



## Master's Thesis

### Comparative analysis of optical in-situ probes and the MSG satellite for improved detection of aircraft icing conditions

Author: Deniz Menekay  
Study Program: ESPACE - Earth Oriented Space Science and Technology  
Chair: Chair of Astronomical and Physical Geodesy  
Matriculation Number: 03750703  
Examiner: Christoph Kiemle  
Supervisor: Johannes Lucke  
Address: Arcisstraße 21, 80333 Munich  
Submission Date: 04.12.2023

---

## Declaration of Authorship

I hereby declare that the thesis submitted is my own unaided work. All direct or indirect sources used are acknowledged as references.

I am aware that the thesis in digital form can be examined for the use of unauthorized aid and in order to determine whether the thesis as a whole or parts incorporated in it may be deemed as plagiarism. For the comparison of my work with existing sources I agree that it shall be entered in a database where it shall also remain after examination, to enable comparison with future theses submitted. Further rights of reproduction and usage, however, are not granted here.

This paper was not previously presented to another examination board and has not been published.

**Student's name:** Deniz Menekay

**Matrikelnummer:** 03750703

Munich, 02.12.2023

Place, date

Deniz Menekay

Signature

---

## Acknowledgements

The completion of this thesis owes much to the support and guidance of numerous individuals. I express my heartfelt gratitude to each of them. My biggest thanks go to Johannes Lucke for being a great supervisor. I have learned so much from him during this period.

Thank you to every person at the DLR Department of Cloud Physics and the SENS4ICE team for their valuable support. Tina Jurkat-Witschas, Simon Kirschler, Johanna Mayer, and Elena De La Torre Castro, your help during the thesis is priceless to me. I am also grateful to my examiner, Christoph Kiemle, for providing me with the initial guidance and support that set the path for this thesis. Your recommendations and support were valuable in getting this project started.

Thank you to the SAFIRE team in Toulouse for making this flight campaign possible and being hospitable throughout the campaign period. I hope F-HTMO will fly safely and host scientists for many more years.

Lastly, I express my deep appreciation to my family for their continuous support and encouragement throughout this journey.

---

# Abstract

In-flight icing poses a significant threat to aircraft safety, potentially leading to the distortion of airflow over wings, loss of lift force, reduced speed, and even stall. While current aircraft are equipped with protection systems against icing, supercooled large droplets (SLDs) still present a safety hazard as they can impinge behind the protected surfaces of an aircraft. To detect and understand the characteristics of SLD conditions, airborne in-situ measurements provide a comprehensive examination of cloud microphysical properties using sensors mounted on an aircraft. One well-established instrument for measuring cloud particles is the Cloud Imaging Probe (CIP), which has been widely used for cloud measurements. However, it is associated with measurement uncertainties. A newer 2D imaging probe, the High-Speed Imager (HSI), is designed to address some of the limitations of the CIP.

The CIP and HSI probes were integrated into SAFIRE’s research aircraft ATR-42 during the SENS4ICE flight campaign conducted in Southern France in April 2023. These in-situ measurements served as reference data for the validation of new ice detection sensors. The primary objective of this study is to develop a methodology aimed at evaluating CIP measurements, particularly in finding out SLDs and large droplet icing conditions following the criteria outlined in Appendix O of aircraft certification standards. The processed data and images from a selected icing encounter are then compared with the HSI data to discriminate their measurement characteristics. The findings can provide support for future flight campaigns to choose the suitable instrument.

The presented data evaluation procedure is then demonstrated on an observational flight of the SENS4ICE campaign. An incoming warm front system with a high likelihood of containing SLD is sampled throughout the flight. Cloud measurements were conducted at temperatures ranging from 0 to -15 °C and altitudes below 5 km. The proposed methodology effectively detected large droplet icing conditions, which extended for nearly an hour. Additionally, the in-situ cloud data collected was used to characterize atmospheric conditions conducive to SLD formation. The results were subsequently cross-validated with Meteosat Second Generation (MSG) satellite products to enable a comprehensive analysis. The tool utilized predominantly categorized the cloud-top of the sampled clouds as mixed-phase. However, the confidence level in these classifications is relatively low due to the obstruction caused by higher-level clouds, limiting the satellite’s observation of the cloud system.

# Contents

<b>1</b>	<b>Introduction</b>	<b>1</b>
1.1	In-flight aircraft icing and SLD . . . . .	1
1.2	Measurement of cloud particles . . . . .	2
1.3	SENS4ICE airborne test campaign . . . . .	3
1.4	Thesis structure . . . . .	5
<b>2</b>	<b>Cloud microphysics and icing certification</b>	<b>6</b>
2.1	Important terminology . . . . .	6
2.2	Cloud phases and aircraft icing types . . . . .	8
2.2.1	Formation of supercooled clouds . . . . .	9
2.2.2	Small droplet versus large droplet icing . . . . .	10
2.3	Formation of SLD icing environments . . . . .	11
2.4	Aircraft icing standards and certification . . . . .	13
<b>3</b>	<b>Methods and instruments to measure icing environments</b>	<b>15</b>
3.1	Cloud Imaging Probe (CIP) . . . . .	16
3.1.1	Measurement principle of the CIP . . . . .	16
3.1.2	Retrieval of cloud microphysical properties from CIP data . . . . .	18
3.1.3	Depth of field and its influence on the sample volume . . . . .	19
3.1.4	CIP data output . . . . .	21
3.1.5	Measurement uncertainties . . . . .	22
3.2	High-Speed Imaging (HSI) Probe . . . . .	25
3.2.1	Multi-beam illumination principle . . . . .	25
3.2.2	Depth of field and beam intersection angle . . . . .	26
3.2.3	Instrument modes and triggering system . . . . .	28
3.3	Optical satellite technology and Meteosat Second Generation (MSG) . . . . .	29
3.3.1	Spinning Enhanced Visible and InfraRed Imager (SEVIRI) . . . . .	30
3.3.2	Bayesian cloud top phase determination . . . . .	31

<b>4</b>	<b>Data evaluation</b>	<b>33</b>
4.1	Description of the dataset . . . . .	33
4.2	Evaluation procedure of the CIP data and applied corrections . . . . .	34
4.2.1	PAS correction . . . . .	34
4.2.2	Correction of missed particles due to dead time . . . . .	35
4.2.3	Filtering usable data . . . . .	36
4.2.4	Depth of field comparison for the CIP and selection of particle rejection mode . . . . .	37
4.2.5	Filtering SLDs from the CIP data . . . . .	39
4.2.6	Creating the combined size distribution . . . . .	42
4.3	Assessment of Appendix O environments . . . . .	43
4.4	Comparison of water content measurements between Nevzorov and CIP instruments . . . . .	44
4.5	Comparison of measurements between the CIP and the HSI . . . . .	45
<b>5</b>	<b>Airborne in-situ measurements of SLD conditions</b>	<b>50</b>
5.1	Meteorological situation on 24 April 2023 . . . . .	50
5.2	Flight track and measurement results . . . . .	51
5.3	Atmosphere characterization of Appendix O icing environment in the selected flight . . . . .	56
5.4	Cross-validation of assessed conditions by the MSG satellite . . . . .	62
<b>6</b>	<b>Conclusion and outlook</b>	<b>67</b>
<b>7</b>	<b>References</b>	<b>70</b>
<b>8</b>	<b>Appendix</b>	<b>74</b>

## List of Figures

1	Aircraft icing has always been a threat to safety in aviation, both on the ground and in-flight. This issue is depicted by war artist Eric Ravilious in his 1942 watercolour painting titled "De-Icing Aircraft" [1]. Aircraft icing is still a topic that requires a profound understanding of atmospheric conditions. . .	1
2	ATR-42 aircraft operated by SAFIRE before an observational flight for the SENS4ICE-EU project, with instruments onboard. . . . .	3
3	Example of stratocumulus cloud tops, which can hold high droplet concentrations. Picture is taken during a SENS4ICE observational flight on 14 April 2023 . . . . .	6
4	An example of a cumulative mass distribution with MVD and $D_{\max}$ shown. .	7
5	Icing environments in the atmosphere [2]. . . . .	8
6	Sketch of homogeneous nucleation (left) and heterogeneous nucleation (right) of cloud droplets. [12] . . . . .	9
7	Post-flight photos of NASA Glenn Research Center's aircraft wing with small-drop (a) and large-drop icing [14]. The black region on the leading edge is the wing's de-icing system . . . . .	11
8	FZRA classical formation process (left) and FZDZ non-classical formation process (right), depicted by Ben C. Bernstein [15]. . . . .	11
9	Visual representations for the formation of in-flight icing environments by active fronts (left) and orographic lifting (right) [19]. . . . .	12
10	LWC envelopes vs temperature of freezing drizzle (left) and freezing rain (right) defined in Appendix O [20]. . . . .	14
11	Three cloud microphysics probes mounted to the ATR-42. . . . .	15
12	Measurement principle of a two-dimensional Optical Array Probe. Image from Wagner et al. [22] . . . . .	16

13	CIP captured images of supercooled droplets from the object plane. The screenshot was taken during a SENS4ICE observational flight from PADS software to control the probe. The vertical axis represents linear photodiode arrays, while the horizontal axis indicates the flight direction. . . . .	17
14	Diagram of an OAP. The shadow of the cloud particle passes over the diode array as the aircraft moves in the flight direction. [25] . . . . .	18
15	Out-of-focus (upper row) and in-focus (lower row) SLD images recorded by the CIP in the same encounter. . . . .	19
16	Depth of field vs. droplet diameter at different intensity levels of the CIP owned by DLR. . . . .	20
17	CIP images of droplets (upper row) and ice particles (lower row). The colouring shows intensity threshold values of 25%, 50%, and 75%, respectively from bright to dark. . . . .	21
18	Definitions of size bins for the CIP. The probe measures the number of particles per size bin. . . . .	22
19	The formation of discrete images in OAPs. Identical droplets (black dots) may result in different discrete images depending on their position relative to the photodiode detector. Image from Korolev et al. [8]. . . . .	23
20	Sample imagery of a dot running at $100 \text{ ms}^{-1}$ but oversampled at $250 \text{ ms}^{-1}$ . Spherical dots appear elliptical at a 2.5 length-to-width ratio. Image from Lilie et al. [27]. . . . .	23
21	Theoretical diffraction pattern with diameter $D = 2R$ at $Z_d = 1$ . The orange dashed circle represents the 50% intensity threshold. Image from Guéllis et al. [29]. . . . .	24
22	Optical layout of the multi-beam imaging approach. Image from Esposito et al. [31]. . . . .	26
23	Schematic of the multi-beam illumination method with two intersecting laser beams. Image from Esposito et al. [31]. . . . .	27
24	The depth of field of the HSI as a function of droplet size. . . . .	28

25	Photo of the HSI owned by DLR (left), the green mark shows the trigger beam window, whereas the orange marks show the illumination beam windows. The figure on the right is from HSI's user manual [30], showing the illustration of the laser beams and the sample area. . . . .	29
26	Illustration of the SEVIRI instrument's scanning principle. Image from Tranquilli et al. [35]. . . . .	30
27	RGB composite (left) and example application of ProPS method (right) for a SEVIRI scene on 25 April 2022 at 12:00 UTC. Image from Mayer et al. [37].	32
28	Comparison of particle count from 1D and 2D data . . . . .	35
29	Example images that are removed by the above-mentioned filters respectively.	37
30	Droplet size distribution measured by the CIP over time in the selected section of the flight. The colour code represents the particle number concentration. .	38
31	On the left side, water content measurements obtained from Nevzorov's TWC cone and three CIP modes recorded between 13:20 and 13:29 UTC are presented. The right side displays the normalized particle size distribution derived from measurements made by the three CIP modes and the CDP during this time range. . . . .	39
32	Supercooled large droplets detected during the selected flight on 24 April 2023 at 12:49 . . . . .	41
33	Ice particles classified as SLD due to being out-of-focus (a), and SLD particles erroneously categorized as "ice" due to the coincidence of two droplets within the same image frame (b). . . . .	41
34	Measurement range of the CDP and CIP probes with separation threshold of 43 $\mu\text{m}$ shown by the red dashed line. . . . .	42
35	The left plot shows comparison and linear regression of Optical LWC and Nevzorov hot-wire TWC measurements, whereas the right plot shows the comparison with Nevzorov LWC measurements. . . . .	45

## LIST OF FIGURES

---

36	Valid particle images captured by the HSI within the time frame of 16:08:59 to 16:12:02 UTC. The largest droplet diameter is 214.6 $\mu\text{m}$ and the smallest is 24.3 $\mu\text{m}$ . . . . .	46
37	Examples of the filtered particle images captured by the CIP within the time frame of 16:08:59 to 16:12:02 UTC. . . . .	47
38	Particle number concentration measurements of the CIP and the HSI between 16:08:59 - 16:12:02 UTC. . . . .	48
39	Normalized particle number concentration histogram of the CIP and the HSI with size bin widths of 15 $\mu\text{m}$ . . . . .	48
40	Tops of measured clouds photographed during the selected flight on 24 April 2023 at 12:47 UTC. A thin layer of higher-level clouds is visible in the image. . . . .	50
41	A radar reflectivity image at the flight zone on 24 April 2023 at 14:35 UTC. The image is provided by Alexandre Floutard in Meteo France. Areas that are surrounded by blue lines show temporary reserved airspaces during the flight. . . . .	51
42	Flight track of the considered flight on 24 April 2023. Each cloud sampling segment is colourized and numbered. . . . .	52
43	Flight altitude profile in ERA5 model, SAT, LWC, cloud particle concentration (N) and ice crystal (LAS) concentration, MVD, and Appendix O icing flag plots over time respectively from top to bottom during the flight. Every cloud sampling segment is identified with a number. . . . .	53
44	The quick-look plot of OF9 showing the profile of particle size measured with the colour code representing the number concentration. The plot on the right side shows the particle size distribution of all measurements. . . . .	54
45	Particle size distributions for each segment respectively with red dashed lines showing the separation between the CDP and the CIP. . . . .	55
46	Durations of cloud encounter types in the chosen flight OF9. . . . .	56
47	30-s averaged LWC data points placed in the freezing drizzle envelope. . . . .	57

## LIST OF FIGURES

---

48	Cumulative mass distributions of Appendix O encounters observed during the selected flight and their mean. . . . .	57
49	30-s averaged LWC, concentration, MVD, temperature, and occurrence data of Appendix O encounters in the selected flight as a function of altitude. . .	58
50	LWC, MVD, and particle number concentration (N) vs temperature profiles of Appendix O encounters during the flight. . . . .	59
51	Frequency distributions of LWC, number concentration, temperature, and altitude for the Appendix O encounters measured during OF9. Blue blocks represent observations with $MVD > 40 \mu\text{m}$ , while orange blocks represent observations with $MVD < 40 \mu\text{m}$ . . . . .	60
52	Frequency distributions of the water content contribution of SLDs and their concentration. . . . .	60
53	30-s averaged LWC, concentration, MVD, temperature, and occurrence data of Appendix O encounters in SENS4ICE-EU as a function of altitude. . . . .	61
54	RGB cloud coverage image and ProPS output for 13:30 UTC, representing Segment 2 and acquisition time of 13:41 UTC. . . . .	63
55	RGB cloud coverage image and ProPS output for 14:15 UTC, representing Segment 3 and acquisition time of 14:26 UTC. . . . .	63
56	RGB cloud coverage image and ProPS output for 15:00 UTC, representing Segment 5 and acquisition time of 15:11 UTC. . . . .	63
57	RGB cloud coverage image and ProPS output for 15:30 UTC, representing Segment 6 and acquisition time of 15:41 UTC. . . . .	64
58	RGB cloud coverage image and ProPS output for 16:00 UTC, representing Segment 7 and acquisition time of 16:11 UTC. . . . .	64
59	Cloud particle images taken by the CIP during 14:27:08-14:28:16 UTC (left) and 14:28:46-14:28:59 UTC. . . . .	65
60	Cloud particle images taken by the CIP during 15:10:53-15:12:26 UTC. . . . .	66
61	Altitude, temperature, LWC, and MVD profiles between 16:08:59 - 16:12:02 .	74

62	Cumulative mass distribution of particles encountered between 16:08:59 - 16:12:02	74
63	Cloud top height map of the flight zone recorded by MSG on 24 April 2023 at 14:00 UTC. [44] The product indicates the height of the highest cloud in each particular pixel. . . . .	75
64	Day Microphysics RGB map of the flight zone recorded by MSG on 24 April 2023 at 14:00 UTC. [44] Green clouds represent lower-level cold clouds measured during the flight, whereas red clouds represent higher-level cirrus clouds. Blue areas are cloud-free. . . . .	75

## List of Tables

1	In-situ reference instruments of the SENS4ICE-EU flight campaign . . . . .	4
2	SLD classes and their LWC values from observations of Cober & Isaac [5]. . . . .	14

## List of abbreviations

- CCN:** Cloud condensation nuclei  
**CCP:** Cloud Combination Probe  
**CDP:** Cloud Droplet Probe  
**CFR:** Code of Federal Regulations  
**CMOS:** Complementary Metal-Oxide-Semiconductor  
**CIP:** Cloud Imaging Probe  
**DLR:** German Aerospace Center (Deutsches Zentrum für Luft- und Raumfahrt)  
**DMT:** Droplet Measurement Technologies  
**DOF:** Depth of Field  
**EASA:** European Union Aviation Safety Agency  
**FAA:** Federal Aviation Administration  
**FL:** Flight Level  
**FZDZ:** Freezing drizzle  
**FZRA:** Freezing rain  
**HSI:** High-Speed Imaging  
**IATA:** International Air Transport Association  
**INP:** Ice nucleating particle  
**IWC:** Ice water content  
**LWC:** Liquid water content  
**MSG:** Meteosat Second Generation  
**MVD:** Median volume diameter  
**SENS4ICE:** SENSors and certifiable hybrid architectures for safer aviation in ICing Environment  
**SEVIRI:** Spinning Enhanced Visible and InfraRed Imager  
**SLD:** Supercooled Large Droplet  
**TAS:** True Air Speed  
**PAS:** Particle Air Speed  
**PSD:** Particle Size Distribution  
**OAP:** Optical Array Probe  
**OF9:** Observational Flight 9  
**UTC:** Coordinated Universal Time

# 1 Introduction

## 1.1 In-flight aircraft icing and SLD



Figure 1: Aircraft icing has always been a threat to safety in aviation, both on the ground and in-flight. This issue is depicted by war artist Eric Ravilious in his 1942 watercolour painting titled "De-Icing Aircraft" [1]. Aircraft icing is still a topic that requires a profound understanding of atmospheric conditions.

In-flight aircraft icing is the formation of ice on the aircraft's surface during flight due to the impingement of supercooled droplets, which can pose a significant threat to flight safety. It can disturb the wing profile, reduce the lift force, increase drag force, and create control problems. Moreover, ice accretion hampers the function of control surfaces, propellers, windscreens, canopies, radio antennas, pitot tubes, and air intakes [2]. Despite remarkable technological safety improvements, aircraft icing remains a topic that needs ongoing investigation. For instance, IATA reported that icing conditions had an 11% contribution to fatal aircraft accidents between 2017 and 2021 [3].

To ensure the safety of flight in icing conditions, typical icing environments have been defined in the American and European Aviation Regulations. The icing environments were defined in Appendix C of the respective documents and are hence known as Appendix C icing conditions [4]. These icing environment characterizations have been used in the certification of commercial aircraft since the 1950s [5]. However, larger droplet sizes were not taken into account due to limited measurement capabilities. Subsequent reports by pilots documented

the hazards associated with larger droplets.

On October 31, 1994, an ATR-72 departed from Indianapolis for Chicago O’Hare International Airport with flight number 4184. After a holding pattern at 10,000 ft in icing conditions due to traffic at O’Hare, the aircraft started descending after air traffic control cleared to 8,000 ft. Shortly after that, the right-wing stalled and the control column deflected fully right. Despite pilots pulling back the control column to recover from the dive, the right-wing stalled a second time and the aircraft crashed near Roselawn, Indiana, resulting in the death of 67 people. After investigations of the crash, the reason was found to be ”supercooled large droplet (SLD) icing” [6]. Additionally, the National Transportation Safety Board described the cause of the accident as ”FAA’s failure to establish adequate aircraft certification standards for flying in icing conditions” [7].

Supercooled large droplets are defined as liquid droplets in clouds with diameters larger than 100  $\mu\text{m}$  that exist in subfreezing temperatures. Accretion of SLD can reach behind the protected surfaces of the aircraft due to their high inertia and create a ridge of ice, resulting in severe aerodynamic disturbances. Since SLD conditions are not covered in Appendix C icing, a review of existing regulations and further study was proposed by the FAA and EASA upon the ATR-72 crash. Field projects were performed with newer instruments and a large database of SLD icing conditions was built [5]. As a result, new additional icing envelopes were defined under Appendix O standards. Nevertheless, the scientific knowledge on SLD formation remains incomplete. Further investigation is also needed with advanced instruments to improve anti-icing and deicing systems.

## 1.2 Measurement of cloud particles

Airborne instruments are used for the microphysical characterization of clouds. One of the most known and used probe types for cloud parametrization is Optical Array Probes (OAP). They were developed in the 1970s and have been extensively used for cloud particle spectrum measurements. The Cloud Imaging Probe (CIP) by Droplet Measurement Technologies (DMT) is an OAP that can measure particle shape, size, concentration, and hence the liquid water content. However, the evaluation of OAPs is challenging due to uncertainties in the measurement. For instance, particles measured outside of the focal plane are artificially enlarged due to variations in diffraction [8].

To overcome this problem, new 2D imaging probes were developed, such as the High-Speed Imaging (HSI) probe. The probe benefits from CMOS sensors and multi-beam illumination methods to control the depth of field and minimize the number of out-of-focus particles. On the other hand, OAPs still have the advantage of a large sample volume and proven correction methods.

The other method to observe icing conditions is spaceborne measurement via satellites. Passive instruments such as SEVIRI aboard the Meteosat Second Generation (MSG) investigate cloud tops to provide information about their phases. MSG's geostationary orbit and adequate spatial resolution of SEVIRI provide continuous observation of cloud tops unless they are hidden by higher-altitude clouds.

### 1.3 SENS4ICE airborne test campaign



Figure 2: ATR-42 aircraft operated by SAFIRE before an observational flight for the SENS4ICE-EU project, with instruments onboard.

The SENS4ICE (Sensors for Certifiable Hybrid Architectures for Safer Aviation in Icing Environment) project is dedicated to developing and testing new sensors for detecting Supercooled Large Droplets (SLD) conditions in flight. These newly developed sensors underwent testing in two simultaneous flight campaigns: one on the Embraer Phenom 300 in the United States and the other on the ATR-42 in Europe.

The Institute of Atmospheric Physics at DLR is responsible for providing accurate and precise

reference data on cloud and icing conditions encountered during these campaign flights. This data is crucial for validating the performance of the new sensors. Additionally, the collected data is used to characterize atmospheric conditions related to SLD icing. To achieve this, underwing cloud probes with established and tested capabilities are employed to measure cloud microphysical properties.

Table 1 lists relevant instruments onboard the ATR-42 aircraft during the campaign. The CDP, CIP, and HSI were mounted under the wings, whereas Nevzorov was mounted on the right-front side of the fuselage. The focus of the study is on atmospheric SLD conditions and temperatures below 0°C. The challenge of detecting and classifying SLD conditions lies in the measurement of a few large droplets in the presence of many more small droplets. It is the case, particularly for the droplet size range of 50  $\mu\text{m}$  to 500  $\mu\text{m}$  [9].

The goal of the data evaluation from the reference instruments is to provide measurements that extend over the entire size range of Appendix C and Appendix O conditions. The CCP (probe combining the grayscale CIP and CDP) is used as the main measurement instrument because it covers the required measurement range. The HSI is aimed to image particles at high resolution for the determination of particle phase. Additionally, the Nevzorov hot-wire probe is used in the campaign as a reference LWC and TWC measurement instrument. As a result, data with a wide range of particle size distribution (PSD) is reached with other essential cloud parameters like the LWC, TWC, MVD, and cumulative size distribution, which are explained in the following chapter.

Instruments				
Name	Method	Measured parameter	Range	Units
Cloud Droplet Probe (CDP)	Forward scattering	Droplet number and size	2-50	$\mu\text{m}$
Cloud Imaging Probe (CIP)	Grayscale OAP	Droplet number and size	15-960	$\mu\text{m}$
High-Speed Imaging (HSI)	2D CMOS imaging	Droplet and ice size and complexity	20-2000	$\mu\text{m}$
Nevzorov	Hot-wire	LWC and TWC	0.03-3	$\text{g m}^{-3}$

Table 1: In-situ reference instruments of the SENS4ICE-EU flight campaign

## 1.4 Thesis structure

This study, presented as a case study based on one flight of the SENS4ICE campaign, focuses on the measurement of SLD cloud conditions and their characterization. The gathered data in the flight is processed and icing encounters throughout the flight are identified. A comparative analysis of the CIP and HSI probes is performed based on a selected icing encounter to find out the differences in measurement characteristics of the two imaging probes. Combined data of the CIP and CDP are then used to investigate cloud microphysical properties to understand the formation and characterization of SLD icing conditions. Finally, the in-situ measurements are compared to the results of the ProPS tool that provides a cloud top thermodynamic phase by using Meteosat Second Generation's SEVIRI products. This comparison aims to evaluate passive satellites' efficiency in detecting SLD icing conditions.

The opening chapter is designed as an introduction, aiming to clarify the concept of in-flight icing, the potential threat posed by supercooled large droplet (SLD) icing to flight safety, the important role of cloud measurement probes in understanding SLD conditions, the SENS4ICE airborne campaign dedicated to advancing technologies for SLD icing prevention, and the specific objectives of this study.

The following two chapters are literature studies. Chapter 2, is an introduction to the SLD icing from a meteorological perspective. General terms and parameters needed to measure a cloud, cloud phases and types of aircraft icing conditions, the formation mechanism of supercooled large droplets, and aircraft standards to ensure a safe flight against icing are explained. On the other hand, Chapter 3 shows state-of-the-art cloud measurement probes and their working principle, together with their pros and cons. The measurement principles of the SEVIRI instrument and the ProPS tool are also presented and explained.

Chapter 4 presents the data evaluation procedure for the CIP data collected during the SENS4ICE flight campaign. The chapter begins by introducing the dataset and explaining the methods used for data correction and evaluation. It proceeds to describe the filters used for detecting SLD particles and icing encounters. The outcomes of this evaluation are then reviewed and compared with the results obtained from the HSI probe. In the final chapter, the methodology introduced in Chapter 4 is applied as a case study to one of the flights conducted during the SENS4ICE campaign. The chapter aims to characterize the atmospheric conditions during the flight and offers an analysis of the obtained results in comparison with SEVIRI products from the MSG satellite.

## 2 Cloud microphysics and icing certification



Figure 3: Example of stratocumulus cloud tops, which can hold high droplet concentrations. Picture is taken during a SENS4ICE observational flight on 14 April 2023

This thesis aims to characterize a specific type of icing condition and review instruments to measure conditions. To do that, it is necessary to establish an understanding of icing conditions and the factors influencing them. In this chapter, key terminology related to atmospheric conditions, various types of aircraft icing, and the formation mechanisms specifically associated with supercooled large droplet (SLD) icing are explained. Furthermore, the historical context and the criteria governing aircraft certifications for icing conditions is discussed to gain insights into previous studies conducted in this field.

### 2.1 Important terminology

The formation of icing environments and their severity mainly depends on several parameters in the atmosphere and clouds listed below:

- **Static air temperature (SAT):** The temperature of the surrounding air measured at a specific point in the atmosphere. The word "static" refers to the temperature that is unaffected by the aircraft's motion and, therefore considered in airborne atmospheric measurements. The unit is in degrees Celcius ( $^{\circ}\text{C}$ ).
- **Liquid water content (LWC):** The water mass in a cloud per unit volume. LWC value is crucial for how much ice accretion has the potential to occur during a passage

through the cloud. The unit is  $\text{g m}^{-3}$ .

- **Total water content (TWC):** The sum of liquid and ice mass in a cloud per unit volume, with the unit  $\text{g m}^{-3}$ .
- **Concentration (N):** The number of droplets in a unit volume. The concentration of SLD, ice crystals, and their ratio are key factors in the determination of the condition. The unit is  $\text{m}^{-3}$ .
- **Particle size distribution (PSD):** The particle concentration (number of droplets per unit volume) over particle size intervals. LWC content and droplet concentration can be derived from the PSD.
- **Median volume diameter (MVD):** The droplet diameter value, which divides the LWC in the droplet size distribution such that half the water volume is in smaller drops and half is in larger drops. MVD is only representative if the droplet size distribution is unimodal and considered to be equivalent to the mean effective drop diameter. The unit used for the term is  $\mu\text{m}$ . (See Figure 4)
- **Volume diameter of 99 percentile (VD99):** The maximum droplet diameter ( $D_{\text{max}}$ ) in this study, which is defined as the diameter where the 99% of the LWC is contained in droplets smaller than ( $D_{\text{max}}$ ). This definition ensures that the ( $D_{\text{max}}$ ) is a stable property and unaffected by the changes in the sampling time. (See Figure 4)

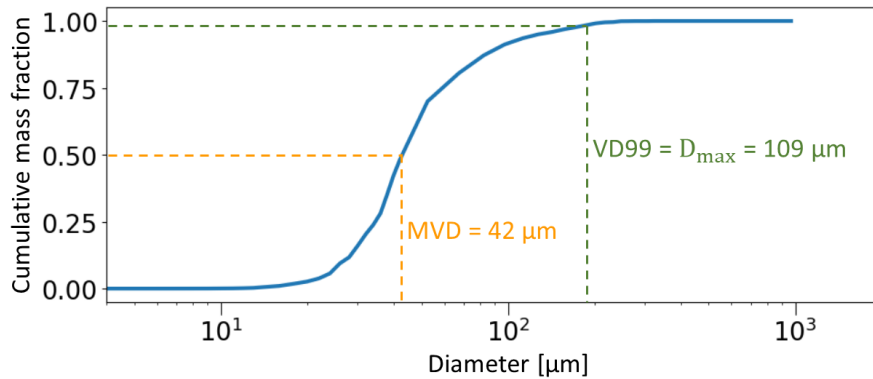


Figure 4: An example of a cumulative mass distribution with MVD and  $D_{\text{max}}$  shown.

## 2.2 Cloud phases and aircraft icing types

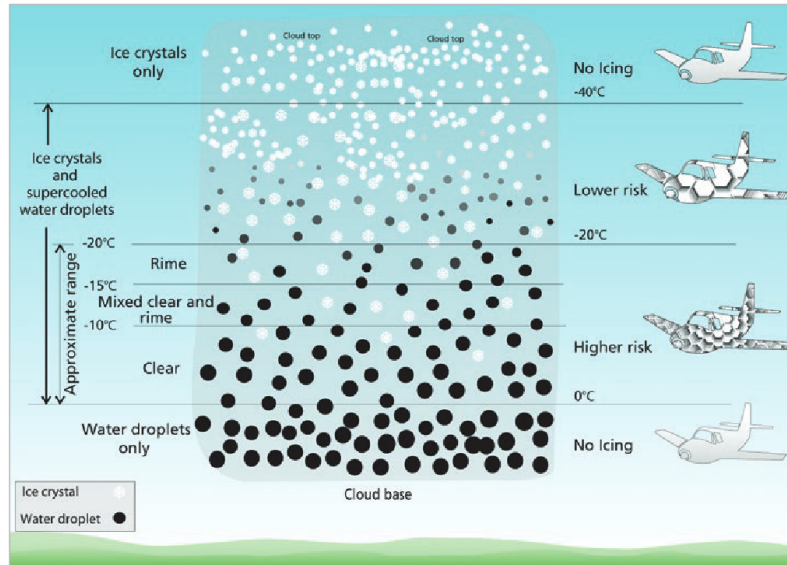


Figure 5: Icing environments in the atmosphere [2].

When a cloud experiences temperatures below the melting point, it can assume one of three states:

- The cloud remains entirely supercooled.
- The cloud becomes a mixed-phase cloud.
- The cloud transitions to a glaciated state.

These states result in corresponding types of aircraft icing: ice-crystal icing, supercooled droplet icing, and mixed-phase icing, as illustrated in Figure 5. Ice crystal icing occurs in glaciated clouds at high altitudes when moist air is lifted into the upper troposphere by deep convective clouds. As the temperature of the moist air decreases below approximately  $-38^{\circ}\text{C}$ , homogeneous nucleation occurs and liquid droplets rapidly freeze into ice crystals. Consequently, clouds transition to an all-ice state below  $-40^{\circ}\text{C}$  [10]. Jet aircraft may encounter issues in glaciated conditions when large amounts of ice crystals are ingested into the engine and sensors, such as pitot tubes. Ice crystals in clouds typically do not contribute to ice accretion on aircraft surfaces because they do not adhere; instead, they are carried away by airflow.

Mixed-phase clouds contain both supercooled droplets and ice crystals and carry the danger of both phases. Recent data sets indicate that a large fraction of icing environments are

mixed-phase and this appears to be the norm rather than the exception [2]. Mixed-phase clouds represent a transition state as ice crystals tend to grow by collision with liquid droplets. Nonetheless, this study primarily centres on supercooled droplet icing, with a specific emphasis on SLDs.

### 2.2.1 Formation of supercooled clouds

*The book 'Atmospheric science: an introductory survey' [11] serves as the primary reference for the following two paragraphs.*

Liquid cloud droplets form when the partial pressure of water vapour in the environment surpasses the saturation vapour pressure. The process is initiated by condensation of water vapour onto aerosol particles, which are small solid or liquid particles suspended in the air. This phenomenon of droplet formation is called "heterogeneous nucleation". Consequently, condensed water dissolves the aerosol and forms a solution water droplet. To nucleate a droplet, the aerosol must be soluble in water e.g. a salt particle, or be sufficiently large in diameter and have a wettable surface. The subset of aerosol particles that can nucleate cloud droplets is called "cloud condensation nuclei (CCN)". Nucleation can also occur in absence of a CCN by merging of several water-vapour molecules in clean air with no aerosols, so-called homogeneous nucleation. However, the resulting droplet is small enough to evaporate quickly and is a less likely case to exist.

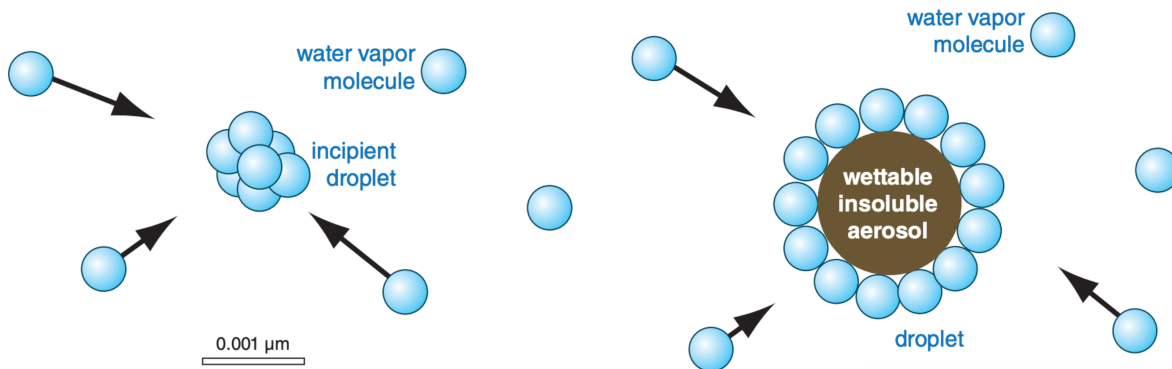


Figure 6: Sketch of homogeneous nucleation (left) and heterogeneous nucleation (right) of cloud droplets. [12]

Once the droplet reaches a certain size, usually between 0.1 and 1  $\mu\text{m}$ , it grows spontaneously due to the decrease in Gibbs free energy of the system caused by condensation. As the droplet grows, the solute concentration decreases, hindering further growth. Additionally, since

volume is proportional to the cube of the droplet diameter, it takes progressively more time for larger droplets to grow under constant conditions. Condensation can typically produce droplets with diameters of up to 50  $\mu\text{m}$  in less than an hour. When growth by condensation slows, cloud droplets can still increase in size through collision with other droplets, known as collision-coalescence (CC).

Cloud droplets do not certainly freeze and transform into ice crystals within the temperature range of  $0^{\circ}\text{C}$  and  $-38^{\circ}\text{C}$ . Instead, droplets persist in the supercooled state, remaining liquid, unless there are ice-nucleating particles (INPs) present in the environment. INPs are organic particles such as amino acids, pollen, algae, and bacteria that initiate the freezing process by heterogeneous nucleation. It's worth noting that the number of INPs is typically much lower than the number of droplets in the cloud environment. Therefore, clouds tend to remain supercooled between  $0^{\circ}\text{C}$  and  $-15^{\circ}\text{C}$ . As the temperature drops below  $-15^{\circ}\text{C}$ , the occurrence of supercooled clouds becomes less frequent because fewer particles can effectively act as INPs at lower temperatures [13].

### 2.2.2 Small droplet versus large droplet icing

Supercooled droplet impingement causes icing on the fuselage and wings, posing a safety risk during flight. Ice accretion on the aircraft differs depending on the droplet size and can be categorized into two types: small droplet icing and large droplet icing, which specifically refers to supercooled large droplets (SLD) with a diameter greater than 100  $\mu\text{m}$ . Small droplets, due to their low inertia, are more easily carried around the wing by airflow and primarily impact the protected leading edge area of the aircraft wing, resulting in rime icing formation. Rime ice, which has an opaque white appearance due to trapped air inside the ice, can be effectively removed by aircraft de-icing systems because of its location and brittleness.

SLDs play a role in the formation of glaze (clear) icing, a significantly more hazardous phenomenon than rime icing. What sets SLDs apart is their substantial mass, which gives them greater inertia and minimizes their susceptibility to airflow. Consequently, SLDs can reach farther behind than small droplets and impact unprotected surfaces on the aircraft. This type of ice accumulation can result in the formation of ridge-shaped ice on the wings, which has the potential to disrupt the aircraft's aerodynamic characteristics by diminishing its lifting force. Furthermore, the rough surface of the ice extending over a substantial area can generate a significant amount of drag.

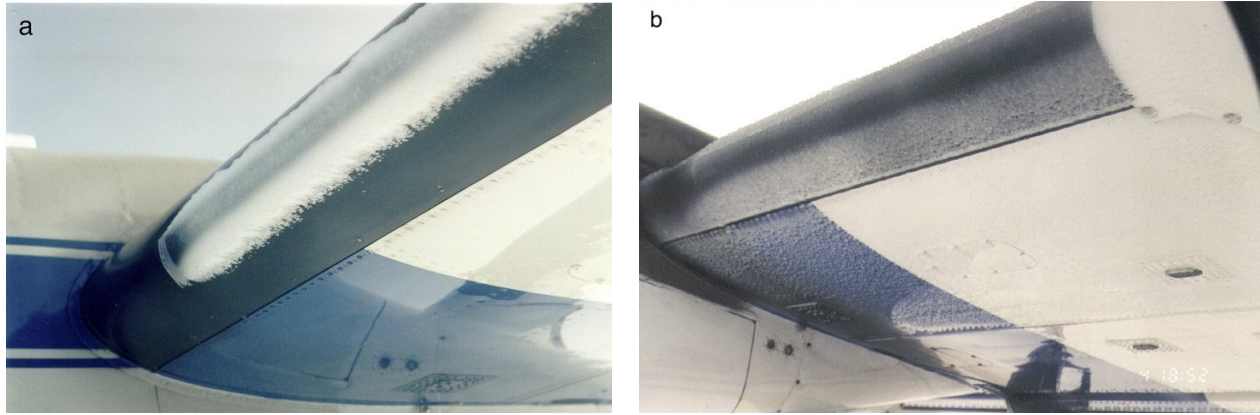


Figure 7: Post-flight photos of NASA Glenn Research Center's aircraft wing with small-drop (a) and large-drop icing [14]. The black region on the leading edge is the wing's de-icing system

### 2.3 Formation of SLD icing environments

Although supercooled clouds are frequently observed in meteorology, the occurrence of SLD conditions is relatively rare. A unique combination of specific circumstances needs to come together. There are mainly two mechanisms causing freezing drizzle and freezing rain, which are two designated subcategories of supercooled large droplets [15]. The factor discriminating them is the maximum volume diameter existing in the icing condition. Icing conditions with  $D_{\max}$  higher than  $500 \mu\text{m}$  are referred to as freezing rain and conditions with lower  $D_{\max}$  are

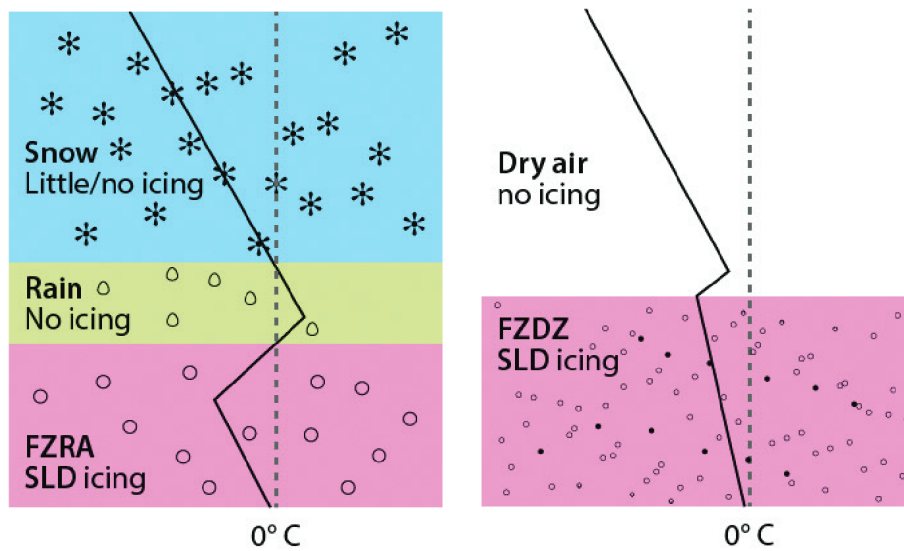


Figure 8: FZRA classical formation process (left) and FZDZ non-classical formation process (right), depicted by Ben C. Bernstein [15].

referred to as freezing drizzle. Formation mechanisms of freezing precipitation are termed "classical" and "non-classical".

The classical formation process occurs when snowflakes fall into a warm air layer with a temperature above the freezing level. Snow melts and forms rain or drizzle then falls into a subfreezing layer. Water droplets then become SLDs in the form of freezing drizzle or rain. The classical process mostly results in freezing rain. Overall, it is responsible for 24% of all freezing precipitation and 62% of freezing rain cases [16].

The non-classical formation process, the so-called "collision-coalescence" or "warm rain" process, occurs in clouds that are primarily composed of liquid water droplets. Cloud top temperatures are expected to be above  $-10^{\circ}\text{C}$ , where there is a low chance of snow production. Colliding and coalescing play a role in the process, resulting in the fall of SLD toward the surface. Their relatively small size range makes them hard to detect by radar systems. Studies [17] also showed that low concentrations of cloud condensation nuclei with high LWC ( $>0.25\text{ g m}^{-3}$ ) are significant for the growth of cloud drops to drizzle sizes.

Icing cloud-producing systems are as follows [18]:

- **Active fronts:** Warm air ascends over cold air and results in the temperature layers explained in the classical formation process. Areas near fronts carry the potential for icing due to the presence of enhanced lifting and ample moisture.
- **Cyclonic circulations:** These circulations generate convergence of air near the centres of low-pressure systems. The result is a large scale of rising motion and cloud formation. The vertical and horizontal extension of the environment can cause long exposures of aircraft icing conditions.

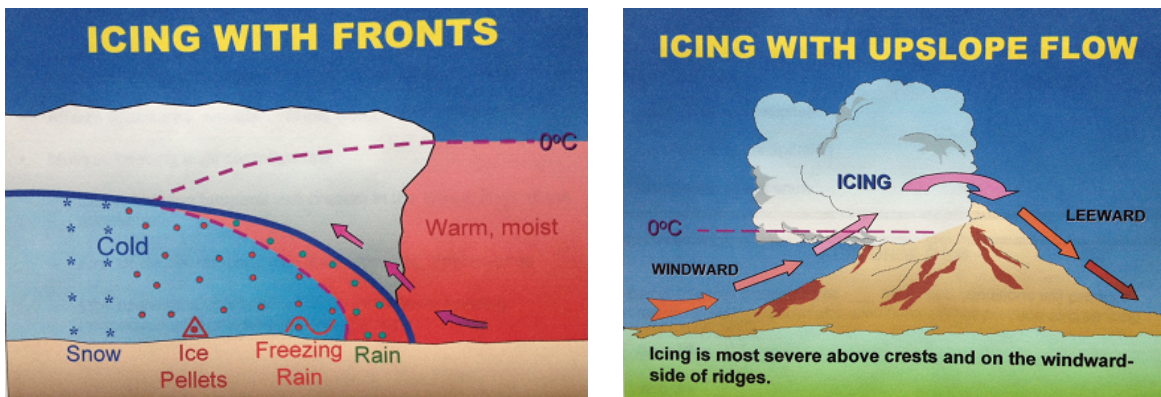


Figure 9: Visual representations for the formation of in-flight icing environments by active fronts (left) and orographic lifting (right) [19].

- **Orographic lifting:** Air masses are forced from low to high elevation over hills and mountains. As the air masses gain altitude, they quickly cool down adiabatically and form clouds. The process also increases the depth of the cloud layer and the liquid concentration of the cloud. Therefore, icing conditions may occur rapidly in elevated areas and severity will be increased over a short time.
- **Warm air advection:** Occurs by warm air moving into a cooler region. The resultant large-scale upward motion lifts clouds to cold temperatures. Icing in this condition has a high potential to be severe due to its widespread nature and upward motion provides a liquid water supply.

## 2.4 Aircraft icing standards and certification

Aircraft manufacturers are required to demonstrate the ability of their aircraft and systems to operate safely in icing conditions. This certification process is governed by the Code of Federal Regulations (CFR), specifically under Title 14 of Part 23 and 25 [4].

Since 1964, Appendix C of 14 CFR Part 25 has been used to certify "Transport category airplanes" for in-flight ice protection systems. This appendix outlines how to characterize aircraft icing environments in both stratiform (continuous maximum) and convective (intermittent maximum) clouds. These environments are characterized by parameters of temperature, liquid water content (LWC), median volume diameter (MVD), and horizontal extent of the environment. However, only MVDs up to 40  $\mu\text{m}$  were considered in the 1940s due to instrument limitations that could not accurately measure larger particles. This limitation meant that larger drop sizes were not incorporated into the certification, even though several reports documented the hazards associated with supercooled large droplets [5]. It was stated in the reports that the current icing regulations do not cover all icing environments with high risk.

The crash of an ATR 72 aircraft near Roselawn in 1994 highlighted the role of supercooled large droplets in forming ridge ice behind protected surfaces on the leading edge. In response, the Federal Aviation Administration (FAA) announced an "In-flight Aircraft Icing Plan". One of the main suggestions of the plan was to redefine current aircraft icing certification envelopes when sufficient information becomes available on SLD and other icing conditions. The plan also suggested establishing a committee to define the icing environment involving SLD and ice crystals. In this respect, a large and comprehensive database of in-situ observations was collected and analyzed from six field programs in three different regions of

North America [5]. It covered a total of 134 flights with 2444 SLD icing environments encountered at 3 km resolution. This work concluded with the characterization of SLD icing environments and opened the way for a new certification standard.

In 2014, this standard was added to part 25 of the Federal Aviation Regulations (14 CFR) as "Supercooled Large Drop Icing Conditions", commonly referred to as "Appendix O" [20]. While Appendix C icing standards cover droplets with MVD smaller than 40  $\mu\text{m}$ , Appendix O is dedicated to addressing SLD conditions for aircraft icing certification. The new standard segregates SLD icing into four subsets: Freezing drizzle environment with (1)  $\text{MVD} < 40$ , (2)  $\text{MVD} > 40$ , and freezing rain environment with (3)  $\text{MVD} < 40$ , (4)  $\text{MVD} > 40$  as shown in the table below. LWC and temperature envelopes of each subset are shown in Figure 10. The first part of the standard describes SLD and parameters for the formation of the SLD environment. The second part describes ice accretions for compliance with the aircraft performance and handling requirements.

Definition	MVD ( $\mu\text{m}$ )	$D_{\text{max}}$ ( $\mu\text{m}$ )	No of 30-s data points	99.0% LWC ( $\text{g m}^{-3}$ )	99.9% LWC ( $\text{g m}^{-3}$ )
FZDZ environment	$< 40$	100-500	1469	0.44	0.58
FZDZ environment	$> 40$	100-500	335	0.27	0.31
FZRA environment	$< 40$	$> 500$	193	0.31	0.37
FZRA environment	$> 40$	$> 500$	447	0.26	0.33

Table 2: SLD classes and their LWC values from observations of Cober & Isaac [5].

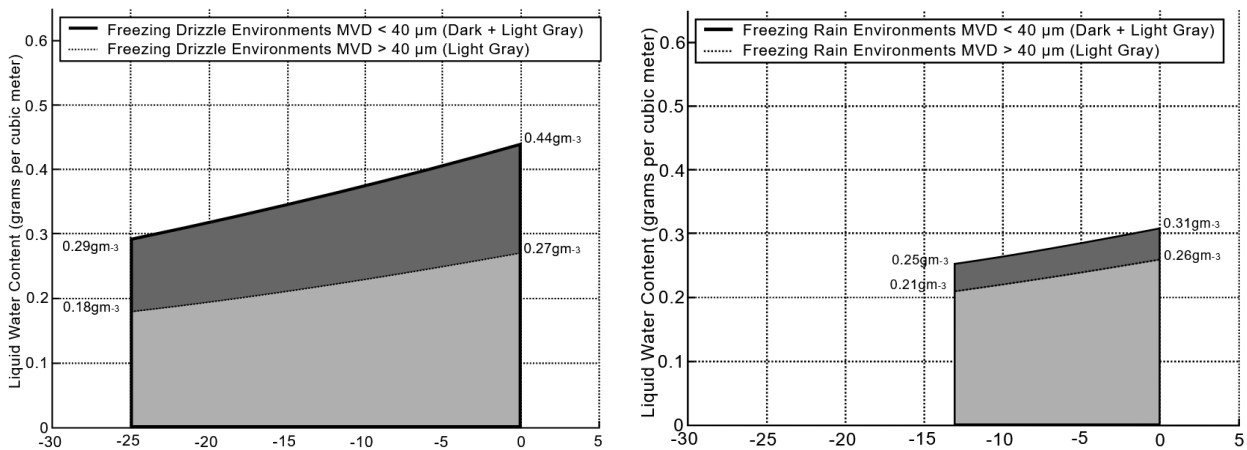


Figure 10: LWC envelopes vs temperature of freezing drizzle (left) and freezing rain (right) defined in Appendix O [20].

### 3 Methods and instruments to measure icing environments



Figure 11: Three cloud microphysics probes mounted to the ATR-42.

The previous chapter covered the concept of in-flight aircraft icing and aircraft standards for ensuring flight safety. On the other hand, a better understanding of the atmospheric conditions causing icing is only possible by capable instruments and accurate data obtained by them. Therefore, this chapter focuses on the instruments used in this study to measure SLD conditions. The measurement principles of these instruments are explained to investigate how cloud microphysical properties are derived and how the uncertainties in measurements occur. Additionally, the MSG satellite and its main instrument, SEVIRI, are introduced with the tool used for validating the cloud environment measured via airborne instruments.

Airborne measurements offer a level of detail and spatial resolution that is unachievable with satellites. Actual knowledge of cloud microphysical properties is mainly from airborne in-situ measurements [21]. This in-situ data acquisition relies on scientific instruments, referred to as probes, which are mounted on research aircraft as photographed in Figure 11. In the image, the lower probe represents the HSI, the upright instrument combines both the CDP and CIP, referred to as the CCP (Cloud Combination Probe), and the instrument at the back is the PIP (Precipitation Imaging Probe). The PIP is excluded from this study due to its measurement range, which surpasses the particle sizes under examination.

### 3.1 Cloud Imaging Probe (CIP)

Optical array probes (OAP) stand out among the various probe types for airborne measurements. Originating in the early 1970s at the National Center for Atmospheric Research, OAPs have been extensively used in airborne campaigns. They are capable of deriving the shape, size, and concentration of cloud and precipitation particles from two-dimensional images by a concentration-depending sampling approach. The primary instrument employed in this thesis, the Cloud Imaging Probe (CIP), falls within the category of OAPs. It was developed in the 1990s by Droplet Measurement Technologies Inc. and underwent multiple upgrades over time.

#### 3.1.1 Measurement principle of the CIP

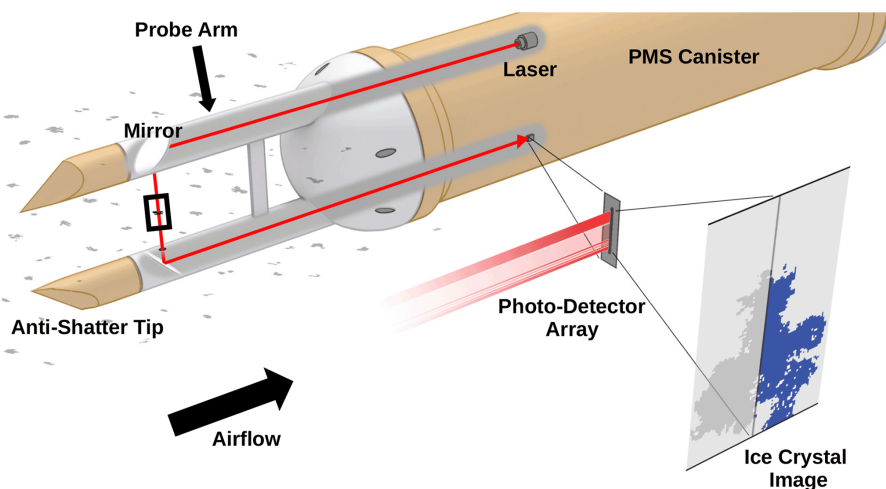


Figure 12: Measurement principle of a two-dimensional Optical Array Probe. Image from Wagner et al. [22]

The Cloud Imaging Probe (CIP) consists of two arms, each equipped with  $90^\circ$  mirrors, a laser emitting at a wavelength of 660 nm, and a linear array of 64 positive-intrinsic-negative photodiodes, each with size of  $15\ \mu\text{m}$ , which are sensitive to light [23]. The photodiode array is aligned perpendicular to the airflow. Inside the probe's canister, a collimated light beam coming out of the laser travels through one arm and reaches the sample area between the two arms. It then goes into the second arm, where a lens focuses it, and the laser light illuminates the photodiode arrays using yet another mirror. For a visual representation of these elements' positions, refer to Figure 12.

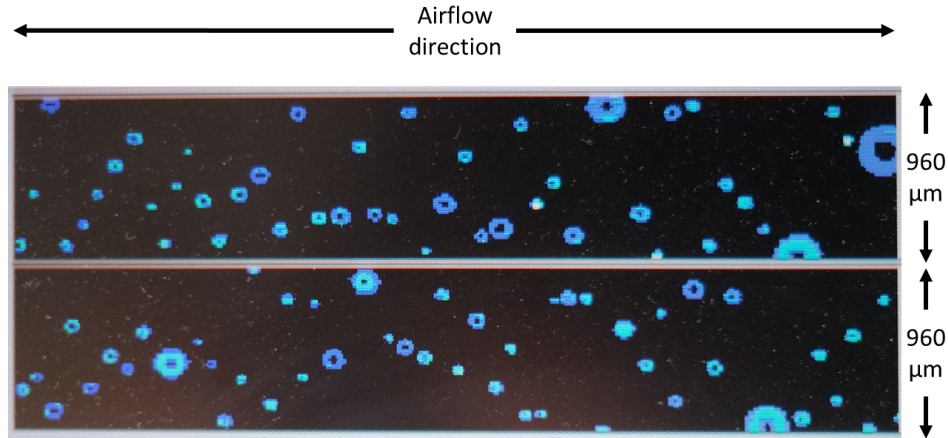


Figure 13: CIP captured images of supercooled droplets from the object plane. The screenshot was taken during a SENS4ICE observational flight from PADS software to control the probe. The vertical axis represents linear photodiode arrays, while the horizontal axis indicates the flight direction.

As the aircraft enters a cloud, cloud particles obstruct the laser beam. If a particle passes close to the object plane, positioned at the midpoint between the two arms, and blocks the light to an extent surpassing a predefined imaging threshold value on at least one photodiode, the probe initiates recording. The probe then captures and reconstructs the image of the particle from a series of consecutive slices aligned with the direction of airflow [24]. The resolution of the probe is determined by the size of a single photodiode. Each slice contains information about the light intensity detected by the photodiodes. An example of images recorded during a flight is shown in Figure 13. The size, shape, and optical properties of particles influence the shadow image recorded by the instrument.

The sampling frequency of the instrument is determined by the following equation [8]:

$$f_s = \frac{\text{TAS}}{d_{\text{photodiode}}} \quad (1)$$

Here, True Airspeed (TAS) represents the speed of the air parcel moving through the probe arms in meters per second ( $\text{m s}^{-1}$ ), while the denominator represents the instrument's resolution in meters (m). For instance, a CIP with a  $15 \mu\text{m}$  resolution and a True Airspeed of  $120 \text{ m s}^{-1}$  provides a sampling frequency of 8 MHz. Perpendicular to the airflow, 64 photodiodes with a  $15 \mu\text{m}$  size provide a measurement range from  $15 \mu\text{m}$  to  $960 \mu\text{m}$ . The size of particles is not limited in the direction of airflow.

### 3.1.2 Retrieval of cloud microphysical properties from CIP data

Several microphysical cloud properties can be derived from images recorded by the CIP. Through image analysis, the size and shape of each particle are determined, and user-defined parameters decide if the particle is counted or not. From this information, cloud properties such as the total number concentration ( $N$ ), the particle size distribution (PSD), median volume diameter (MVD), and maximum drop diameter (VD99) are determined.

The total number concentration tells how many cloud particles in the CIP size range can be found in a unit volume, which is most often specified per cubic centimetre. This parameter is calculated by the amount of all particles detected within a sampling time, which is usually set to one second, divided by the sample volume ( $SV$ ). The sample volume is calculated for each particle separately by the following equation:

$$SV = \omega_{eff} \cdot \text{DOF} \cdot \text{TAS} \cdot t_s \quad (2)$$

Where  $\omega_{eff}$  refers to the effective width of the photodiode array,  $t_s$  is the elapsed time of the measurement, and DOF is the depth of field (explained in the next section). The multiplication of  $\omega_{eff}$  and DOF yields the sample area of the probe, which is the cross-sectional area along the laser beam where particles are detected, being in the middle of two arms and perpendicular to the flow velocity as depicted in Figure 14.

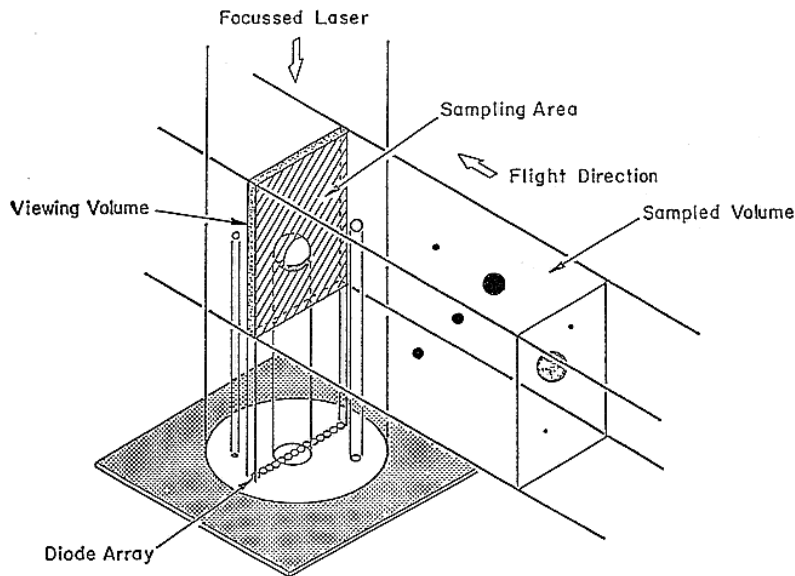


Figure 14: Diagram of an OAP. The shadow of the cloud particle passes over the diode array as the aircraft moves in the flight direction. [25]

In order to describe the particle size profile inside the cloud, the particle size distribution needs to be calculated. The particle size distribution represents the particle counts of each size bin over the sampling time with respect to the sample volume. The CIP provides the distribution of particle sizes in size bins with a width of the probe resolution. To ensure comparability across instruments with varying bin widths, the particle size distribution is normalized to each bin width. Therefore, the unit of the parameter (dN/dD) is given in  $\text{cm}^{-4}$  or in  $\text{cm}^{-3} \mu\text{m}^{-1}$  because the concentration unit is additionally divided by the bin size. The median volume diameter and maximum drop diameter can also be derived from the size distribution as explained in Section 2.1.

The mass of spherical cloud droplets can be derived from the size measured by the CIP. The liquid water content of the cloud can then be calculated as the sum over all 64 size bins.

$$\text{LWC} = \sum_{i=1}^{64} \frac{4}{3} \cdot \pi \cdot \left(\frac{D_i}{2}\right)^3 \cdot \rho_{\text{water}} \cdot \frac{N_{i, \text{droplets}}}{SV} \quad (3)$$

### 3.1.3 Depth of field and its influence on the sample volume

Particles passing near the object plane, which is the plane in the middle of two arms and parallel to the airflow as depicted in Figure 14, are perfectly in-focus. As a particle moves farther from the object plane during measurement, the shadow imaged by the detector becomes increasingly blurred, enlarged, and distorted as shown in Figure 15. The upper row shows SLD images with out-of-focus particles, while the lower row displays in-focus SLDs. Out-of-focus droplets recognizably appear larger and exhibit a larger Poisson's spot.

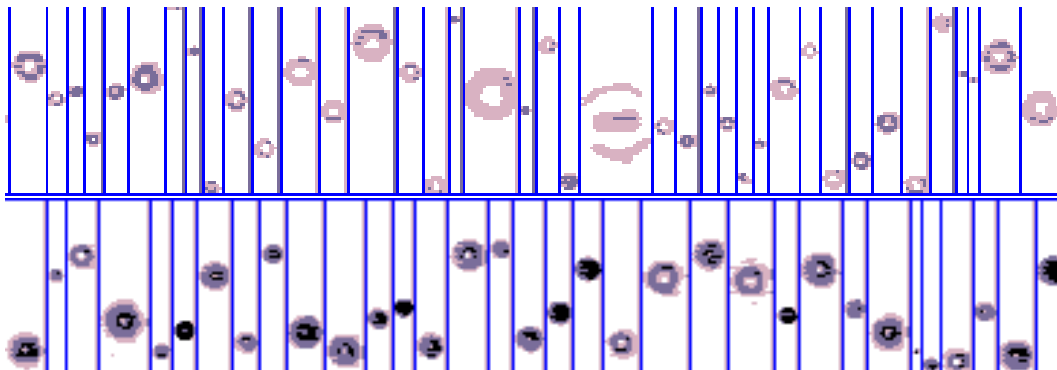


Figure 15: Out-of-focus (upper row) and in-focus (lower row) SLD images recorded by the CIP in the same encounter.

The depth of field (DOF) is defined as the area between the two probe arms where particle passage results in shadowing that exceeds the defined shadowing threshold. The DOF value of an OAP is calculated by the following formula for each particle size:

$$\text{DOF} = \pm c(\chi) \cdot \frac{D^2}{4 \cdot \lambda} \quad (4)$$

In this formula,  $c$  is a dimensionless number that depends on the intensity threshold ( $\chi$ ) that needs to be exceeded and can be configured by the user. As you increase the threshold value, the depth of field narrows, making measurements less sensitive [8]. The plus-minus sign indicates that the depth of field is symmetrical around the object plane. So, the total depth of field is twice the value calculated with the object plane at its centre.  $\lambda$  represents the laser beam's wavelength, and  $D$  is the true diameter of the droplet. The equation shows that the depth of field and hence the degree of blurriness in the shadow image as particles move away from the object plane is largely influenced by their size [8]. The influence of the particle size on DOF is indicated in Figure 16 with particle selection modes introduced in the following chapter. The exposed laser length of 108 mm defines the mechanical limit of the instrument, which is the distance between two arms.

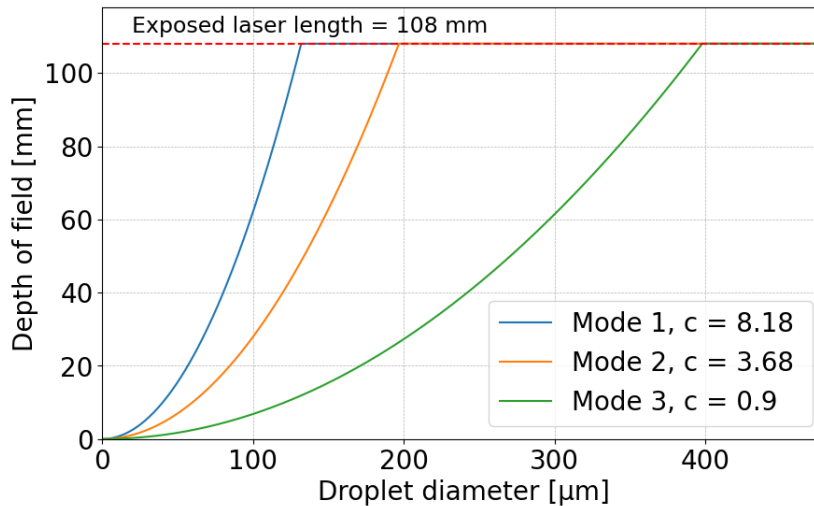


Figure 16: Depth of field vs. droplet diameter at different intensity levels of the CIP owned by DLR.

As mentioned before,  $c$  in Equation 4 is determined by the intensity threshold of the probe. The DOF decreases as the threshold value increases, thus the sensitivity of the probe decreases and only records particles that are closer to the object plane.

In terms of the intensity threshold, OAPs can be categorized into two classes: monoscale and grayscale [26].

- **Monoscale probes** record the light intensity level of the diode using just one bit of information. They classify the intensity level as either a "shadow" if it's less than half of the laser beam intensity (bit value of zero) or as "no shadow" if the intensity level is above this threshold (bit value of one).
- **Grayscale probes** can save two bits of information for the light intensity value, providing more detail. The CIP is a grayscale probe using intensity threshold values of 25%, 50%, and 75% for each pixel to indicate how effectively particles cast shadows on the light.

An example of output images from a grayscale CIP is given in Figure 17. The imaging threshold can be set to one of the three levels. For instance, if the imaging threshold is set to 50%, images of particles that shadow half or more of the light intensity on at least one photodiode will be recorded.

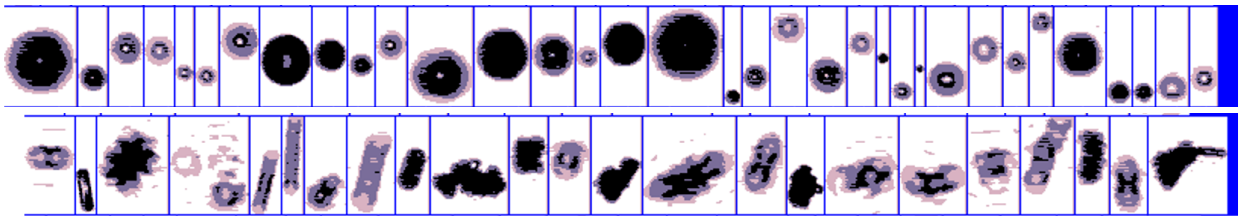


Figure 17: CIP images of droplets (upper row) and ice particles (lower row). The colouring shows intensity threshold values of 25%, 50%, and 75%, respectively from bright to dark.

### 3.1.4 CIP data output

The CIP provides data in two formats: 1D and 2D. The 1D data preserves information about the particle size perpendicular to the flight direction, which is directly generated by the probe and quickly transmitted to the operator's computer during the measurement. In this format, the probe estimates the maximum size of each particle by measuring the furthest distance between any two shadowed photodiodes. Each particle gets sorted into one of the 64 sizing bins with a width of the resolution value ( $15\ \mu\text{m}$ ). A description of size bins for the CIP is shown in Figure 18. For instance, droplets between  $37.5\text{-}52.5\ \mu\text{m}$  shadow three photodiodes, therefore get a size value of  $45\ \mu\text{m}$ . The number of particles falling into each size bin is recorded over 1 second and the count is saved on the operator's computer.

However, 1D data has some limitations. It cannot be corrected for various errors, such as stuck bits, noise, or instances where two small particles are interpreted as one large particle.

This type of data is primarily used for real-time display, immediate access to particle size concentration, and evaluation of missed particles by the probe, rather than for in-depth data analysis [23]. 2D image data (as shown in Figure 17) is used for more comprehensive analysis and research. This data set consists of shadow images captured by the CIP in three grayscale values, providing the shape and size of each particle, along with precise timestamps for each measurement and the total count of particles recorded.

	<b>bin_min</b>	<b>bin_max</b>	<b>bin_mid</b>	<b>bin_width</b>
<b>1</b>	7.5	22.5	15.0	15.0
<b>2</b>	22.5	37.5	30.0	15.0
<b>3</b>	37.5	52.5	45.0	15.0
<b>4</b>	52.5	67.5	60.0	15.0
<b>5</b>	67.5	82.5	75.0	15.0
...	...	...	...	...
<b>60</b>	892.5	907.5	900.0	15.0
<b>61</b>	907.5	922.5	915.0	15.0
<b>62</b>	922.5	937.5	930.0	15.0
<b>63</b>	937.5	952.5	945.0	15.0
<b>64</b>	952.5	967.5	960.0	15.0

Figure 18: Definitions of size bins for the CIP. The probe measures the number of particles per size bin.

### 3.1.5 Measurement uncertainties

CIP measurements are subject to several uncertainties during cloud particle measurements and need to be corrected for accurate information retrieval.

- **Discrete nature of imaging:** As explained in the previous section, particles passing through the laser beam are registered to pixels that are shadowed by that particle and respective size bins. The resulting image of the same particle can vary depending on its position with respect to the photodiode array as shown in Figure 19. This case leads to some uncertainties in the sizing of the droplet especially in small particles. The quality of the image depends on the probe resolution, the magnification of the optical system, and the distance between photodiodes.

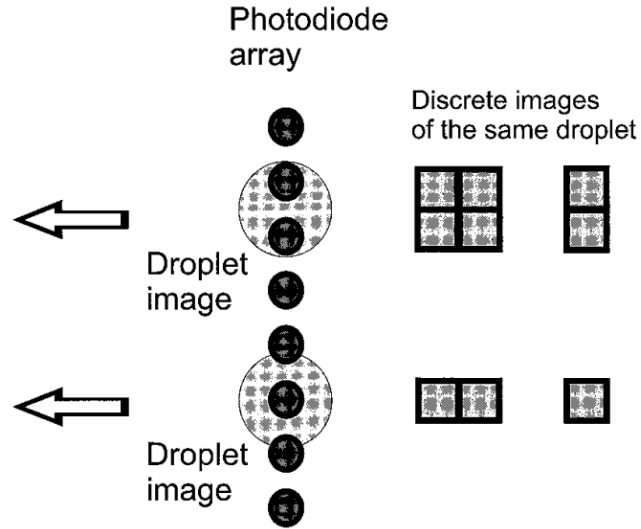


Figure 19: The formation of discrete images in OAPs. Identical droplets (black dots) may result in different discrete images depending on their position relative to the photodiode detector. Image from Korolev et al. [8].

- Definition of the DOF:** Depth of field is one dimension of the sampling area, which is dependent on the particle size as discussed previously. The DOF correction for smaller particles is larger and leads to large errors. This is because any bias in the DOF directly affects the sample volume and, thus the measurements. To derive accurate cloud properties, the exact volume that the instrument measures should be determined [8].
- Air speed:** During the measurement, the probe should continuously be set to the aircraft speed in order to get the correct measurements. Otherwise, the sampling frequency will not match the airflow speed and droplets will not be imaged as a perfect sphere. Consequently, this causes errors in the volume/mass derivation and hence in cloud measurements.

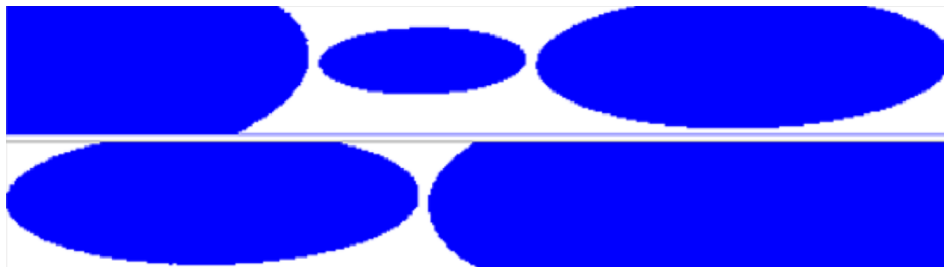


Figure 20: Sample imagery of a dot running at  $100 \text{ ms}^{-1}$  but oversampled at  $250 \text{ ms}^{-1}$ . Spherical dots appear elliptical at a 2.5 length-to-width ratio. Image from Lilie et al. [27].

- Out-of-focus particles:** The individual particle size retrieval is influenced by the actual particle size and its distance from the object plane. Particles measured outside of the focal plane are artificially enlarged due to variations in diffraction [8] and develop a bright spot in the centre. These spots are called "Poisson spots", after the scientist Simeon Denis Poisson, who discovered this phenomenon in 1818 [8]. This is usually the case for spherical water particles such as SLDs and can lead to inaccurate size measurement or misdetection. A possible correction was presented in Korolev et al. [28]. When a Poisson spot is detected, its area is measured and compared to the area of the complete particle. The ratio of these two areas is used to derive a correction factor, which is then applied to adjust the size measurement.

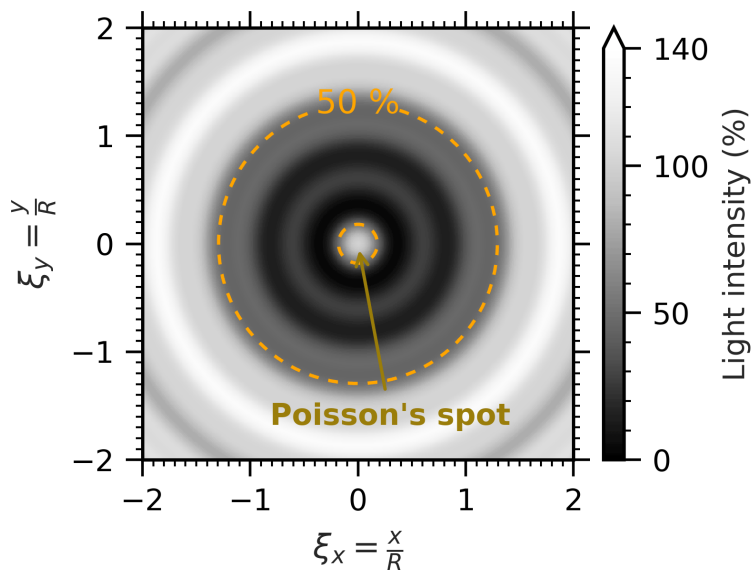


Figure 21: Theoretical diffraction pattern with diameter  $D = 2R$  at  $Z_d = 1$ . The orange dashed circle represents the 50% intensity threshold. Image from Guélis et al. [29].

- Retrieving aspherical particle properties:** Particle size is a 3-dimensional feature and it is derived from a 2-dimensional image. Particles are arbitrarily oriented in space and aspherical particles do not carry the same size characteristics from every angle as shown in Figure 17. This feature makes it very difficult to retrieve ice crystal properties by OAPs and some assumptions have to be made [29]. As this study is focused on detecting SLDs, which are spherical particles, required corrections for aspherical particles are not considered.
- Missed particles due to dead time:** Once particle images are captured by OAPs, they travel through buffers, transmission, and to the data system for recording and displaying. When both the aircraft speed and cloud particle concentration are high,

particles passing through the sample area of the OAP can lead to very high data rates, surpassing the buffer's capacity. Consequently, the probe stops image recording and goes into a mode named "overload". This mode creates a period when data is not recorded called "dead time". Alexei Korolev determined that the CIP goes into overload when the data rate exceeds 100 (4096 bytes) buffers per second [23]. Tests have also shown that the decrease in counting efficiency can be up to 50% between speeds of 38 and 176  $\text{ms}^{-1}$ . The CIP uncertainties in counting and sizing particles smaller than 75  $\mu\text{m}$  are especially problematic according to Gurganus et al. [23].

## 3.2 High-Speed Imaging (HSI) Probe

Alongside the CIP, a new instrument called the "High-Speed Imaging (HSI) probe" was flown during the campaign. The HSI, depicted in Figure 11, is an in-situ probe developed by Artium Technologies Inc. to address some of the measurement challenges associated with OAPs, such as out-of-focus particles and the depth of field's reliance on particle size. The probe captures 2D images of spatial volume and provides a shadow image of the particle to obtain cloud particle size distribution, thermodynamic phase, number density (concentration), and liquid water content of the sampled cloud.

### 3.2.1 Multi-beam illumination principle

The measurement principle of the HSI is based on the multi-beam illumination approach, whereas OAPs use the single-beam illumination method. The HSI utilizes six compact diode lasers with a wavelength of 860 nm. Each laser is equipped with a beam expander and collimator to converge all beams to a common point, creating the probe's sample volume. After passing the sample volume, these lasers are directed to the CMOS imaging sensor via optical elements consisting of receiver lenses and image transfer lenses as depicted in Figure 22. The sensor provides 1624 x 1240 pixels monochromatic images with 256 grayscale values. The digital resolution of the probe is set to 3.03  $\mu\text{m}$  in factory calibration. Therefore, the probe captures high-resolution images of cloud particles, which enhances the accuracy and reliability of determining particle phase [30].

The multi-beam illumination method, as the name suggests, involves using multiple converging laser beams to illuminate particles. Shadows produced at each beam only overlap when particles are at the focal plane of the receiving lens. Otherwise, shadows of particles prop-

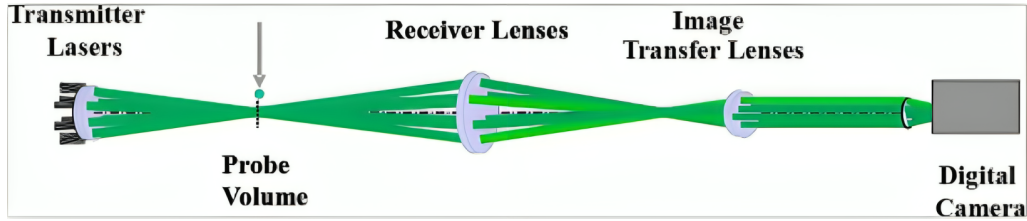


Figure 22: Optical layout of the multi-beam imaging approach. Image from Esposito et al. [31].

agate along the beam into the imaging lens. Therefore, the depth of field can be precisely defined and blurred images are reduced. A schematic of the method with two converging lasers for simplicity is shown in Figure 23. Plane 1 marks the beam intersection point, defining the focal plane of the probe. Planes 2 and 3 represent the positions of particles that would be out-of-focus as pass further away from the focal plane.

### 3.2.2 Depth of field and beam intersection angle

As previously discussed in the CIP section, when particles are located outside the focal plane, they result in blurry images and become unacceptable beyond the depth of field. This parameter is dependent on the actual size of the particle and has a nearly linear relationship with the particle size. However, small errors in DOF determination can result in large errors in cloud measurements. Therefore, the depth of field is a significant source of error, particularly when measuring small particles.

With multi-beam illumination that is used for the HSI, particles at the beam intersection point produce sharp and deep shadow images. Conversely, particles situated away from this intersection point do not create sharp images because the shadows from each beam do not overlap. What sets multi-beam illumination apart from single-beam illumination is that the images become blurred and also separate within each laser beam when the particle is not at the focal plane. This separation of particle shadow images is illustrated in Figure 23. How rapidly shadow images separate particles is determined by the beam intersection angle, which is defined by the angle between two laser beams. A higher beam intersection angle results in greater separation of the particle image illuminated by different laser beams. In image processing, this capability enables the determination of whether a particle is acceptably in-focus or out-of-focus as shadow images of the particle will be more separated as it is further away from the object plane.

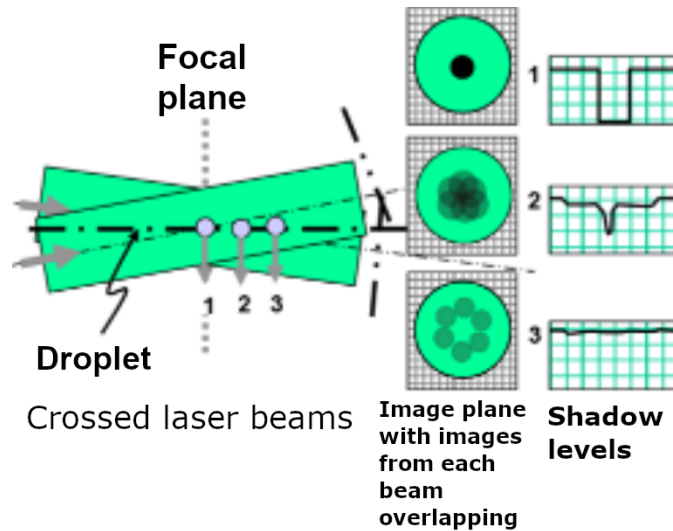


Figure 23: Schematic of the multi-beam illumination method with two intersecting laser beams. Image from Esposito et al. [31].

On the other hand, particles that pass through the beams from outside the intersection point produce out-of-focus shadows on one or two of the beams, but these shadows do not frequently occur in other beams. This configuration helps in reducing the influence of large particles located outside the focal plane. However, the nature of this measurement technique limits the sample volume of the probe, which is smaller compared to the typical sample volumes of OAPs.

*More details about the multi-beam illumination approach can be found in Biagio M. Esposito's paper [31]. It is also used as the primary resource for this section.*

The sample volume of the HSI, used to derive cloud microphysical parameters, relies on the dimensions of the camera frame (length and width) and the depth of field established through calibration relating to droplet size. Figure 24 depicts the depth of field of the probe utilized in this study. It exhibits a parabolic curve for smaller droplet sizes, which transitions to a relatively constant trend for droplets larger than  $100\ \mu\text{m}$ , with an upper limit of  $750\ \mu\text{m}$ . Number density is computed by dividing the total number of droplets by the total volume of the frames.

It is important to note that both imaging modes of the probe contain biases in the measured size distribution. Larger objects can be imaged over a greater depth of field than smaller particles. Therefore, the raw data tends to be biased towards larger droplet sizes. As a solution, Artium introduced Probe Volume Correction (PVC) in order to correct the dataset by the factor of droplet size-dependent probe volume. This should be applied to the particle

size distributions, number density, and LWC measurements via the probe’s software.

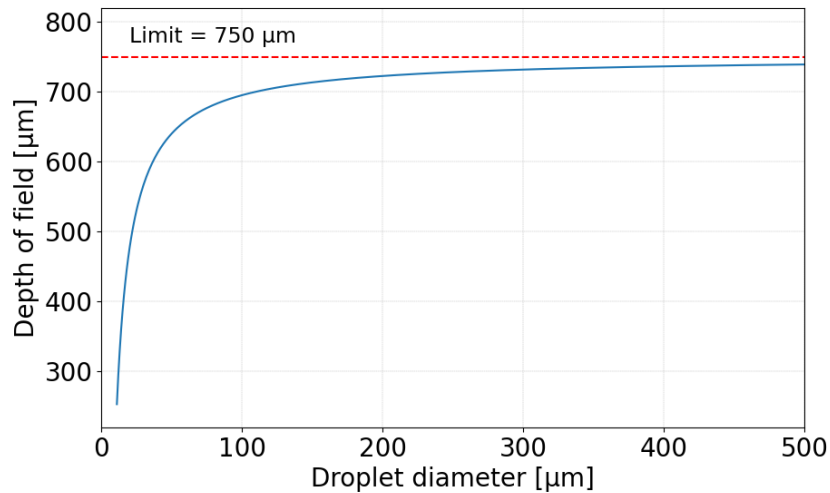


Figure 24: The depth of field of the HSI as a function of droplet size.

### 3.2.3 Instrument modes and triggering system

The High-Speed Imager (HSI) operates in two essential modes: (1) camera mode and (2) trigger mode. In the camera mode, lasers pulse synchronously with the CMOS sensor, enabling particle imaging at an adjustable frame rate of up to 475 Hz. This mode allows the utilization of the entire sample volume unlike the trigger mode. However, the probe’s sampling efficiency in a low-concentration environment is comparatively lower in the camera mode because sample collection depends on particles being within the imaging system’s view volume at the time of laser firing.

The trigger mode involves a modulated laser beam directed coaxially with the illumination beams. A trigger detection system emits and collects scattered light at a frequency of 20 MHz. The trigger laser with a wavelength of 660 nm allows easy separation from the illumination beams. As particles traverse the laser beam, imaging lasers are activated to capture the volume within the sample area. Consequently, sampling relies on the rate of particle arrival or flux through the trigger sample volume, resulting in higher sampling efficiency. For the configuration depicted in Figure 25, the illumination beams have a larger diameter than the viewing area of the imaging system optics, ensuring relatively uniform illumination across the sample volume. However, the sample area’s upper limit is determined by the trigger laser beam’s diameter, indicated by the red area in the figure, significantly reducing the sample area.

The trigger system has an additional drawback in high-concentration scenarios [30]. In situations with more than one particle arriving during one camera shutter opening, the second particle is lost since the trigger system allows only one laser firing per camera shutter opening. Therefore, the trigger system is recommended when the particle rate falls below one per image. Given the anticipation of higher concentrations to be measured in the flights and prioritizing a larger sample volume, the camera mode was selected during the campaign.

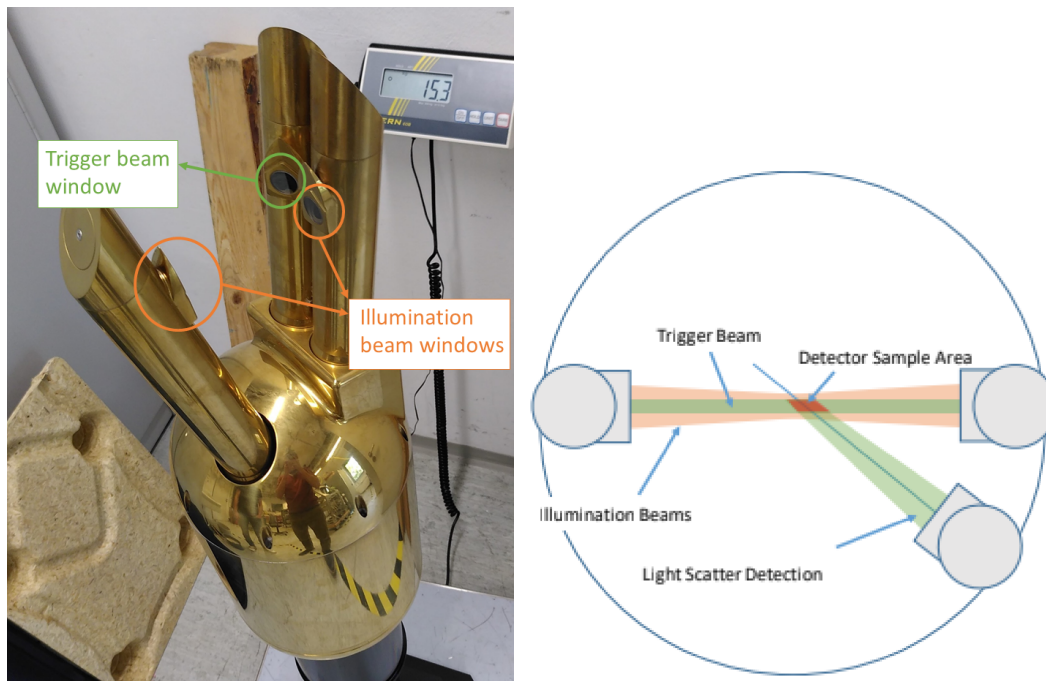


Figure 25: Photo of the HSI owned by DLR (left), the green mark shows the trigger beam window, whereas the orange marks show the illumination beam windows. The figure on the right is from HSI's user manual [30], showing the illustration of the laser beams and the sample area.

### 3.3 Optical satellite technology and Meteosat Second Generation (MSG)

The use of geostationary satellite imagery provides multiple advantages, particularly for cloud studies. These satellites are positioned at an altitude of approximately 36,000 km above the Earth's equator with an orbit inclination angle of  $0^\circ$ . They complete one orbit in about 24 hours to match the Earth's rotation period. Therefore, geostationary satellites allow for a constant view of the same area with relatively high temporal resolution and have the capability to observe conditions with high temporal resolution. Additionally, passive sensors onboard the satellites provide a wide field of view.

Meteosat satellites are a well-known example of a geostationary satellite series that have played a crucial role in providing essential data for weather forecasting, environmental monitoring, and climate research since their first mission in 1977. Meteosat Second Generation (MSG) satellites are an improved follow-on generation of the original METEOSAT satellites and have been actively monitoring the Earth since 2002 [32]. Currently, Meteosat-9, 10, and 11 are MSG satellites operating over  $45.5^{\circ}\text{E}$ ,  $0^{\circ}$ , and  $9.5^{\circ}\text{E}$  respectively after the mission swap between Meteosat-10 and 11 [33]. Meteosat-11 provides an operational European 'rapid scan' mode service every five minutes, whereas Meteosat-9 and 10 provide images of the full Earth scan every 15 minutes.

### 3.3.1 Spinning Enhanced Visible and InfraRed Imager (SEVIRI)

SEVIRI, the primary payload of MSG satellites, is an optical imaging radiometer manufactured by Astrium SAS [34]. The instrument is equipped to capture Earth disc images across 12 spectral channels, including four in the Visible (VIS) and Near-Infrared (VNIR) spectra, and eight in the InfraRed (IR) range. Notably, it provides imaging at a resolution of 1 km when observing from a nadir viewing angle at an altitude of 35,800 km for the High Visible (HRV) channel, whereas it offers a 3 km resolution for the IR and three other visible channels.

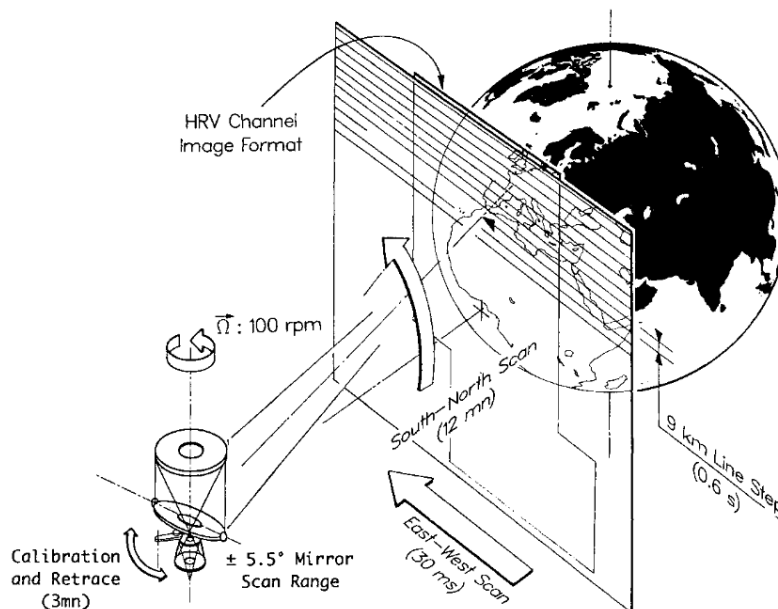


Figure 26: Illustration of the SEVIRI instrument's scanning principle. Image from Tranquilli et al. [35].

The SEVIRI instrument is designed to image the Earth from a satellite spinning at 100 rpm, providing the East-West movement during scanning. The movement of the line-of-sight in the South-North direction is controlled by the scanning mirror as illustrated in Figure 26. Radiance from the target is collected by the telescope and focused onto the detectors. At the focal-plane level of the telescope, channel separation is achieved through folding mirrors. Periodically, a flip-flop mechanism is activated to place the IR calibration reference source in the field of view of the instrument.

As previously mentioned, the SEVIRI instrument can operate in two scanning modes: Full Earth Scanning (FES) and Rapid Scanning Service (RSS). Full Earth Scanning entails rotating the primary mirror within a  $\pm 5.5^\circ$  range, progressing from South to North in steps of 125.8 microradians. This process forms a full-disk SEVIRI acquisition comprised of 3712 lines of image data, completed within 12.5 minutes. Following the South-North (forward) scan, a 2.5-minute retrace phase repositions the mirror to its initial orientation, preparing for the next acquisition beginning at  $-5.5^\circ$ . Consequently, this results in an overall repeat cycle of 15 minutes [34]. Rapid Scanning Service mode operates similarly but focuses on a specific latitude range of approximately  $15^\circ$  to  $70^\circ$  corresponding to 464 scanning lines [36]. Therefore, the rapid mode shortens the repeat cycle to 5 minutes. In this study, the Full Earth Scanning products are used for comparison with the in-situ measurements.

### 3.3.2 Bayesian cloud top phase determination

*The manuscript 'Bayesian Cloud Top Phase Determination for Meteosat Second Generation [37]' by Mayer et al. is used as the primary reference for this section. Refer to that manuscript for further information.*

The development of a method to infer the thermodynamic phase of cloud tops from passive sensor data has become a necessity for extensive monitoring of clouds and their radiative effect. A tool "ProPS (PRObabilistic cloud top Phase retrieval for SEVIRI)" by the DLR Institute of Atmospheric Physics offers the capability to detect clouds and determine their thermodynamic phase for the SEVIRI imager. While existing methods often only distinguish between ice and liquid phases, ProPS enables cloud top phase classification in five categories: optically thin ice (TI), optically thick ice (IC), mixed-phase (MP), supercooled liquid (SC), and warm liquid (LQ) clouds.

The ProPS method utilizes a Bayesian approach, incorporating data from both the cloud mask and phase information retrieved from the DARDAR product, which integrates the

CloudSat radar and the CALIPSO lidar measurements. The primary advantage of the Bayesian approach is its ability to handle complexity and consolidate diverse spectral information from various SEVIRI channels into a single metric. Moreover, this approach offers a quality parameter for the result computed from the output of the ProPS algorithm.

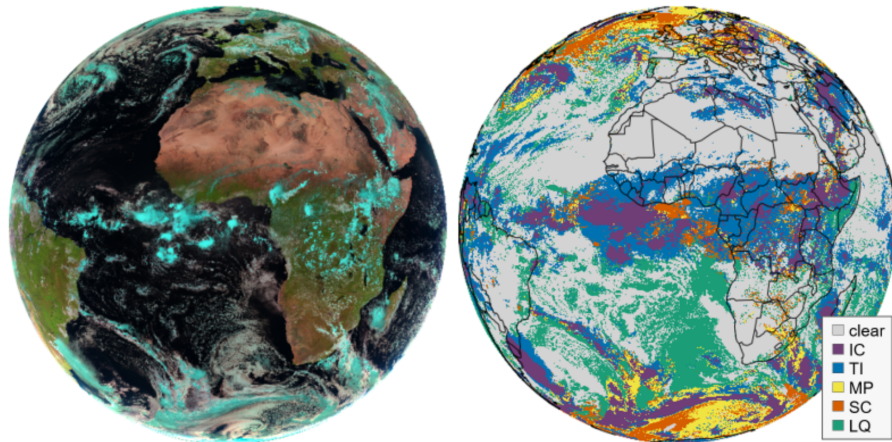


Figure 27: RGB composite (left) and example application of ProPS method (right) for a SEVIRI scene on 25 April 2022 at 12:00 UTC. Image from Mayer et al. [37].

The synergistic lidar-radar technique is a reliable and comprehensive method for defining the cloud phase from satellites due to the combination of different penetration depths and particle size sensitivities. Therefore, DARDAR data serves as the ground truth in order to detect clouds and distinguish their phase. Over five years, data from DARDAR and SEVIRI measurements in specific channels, along with auxiliary data such as surface temperature from the ERA5 model and surface type, are collected to create a co-located dataset with cloud top phase information from DARDAR. SEVIRI channels used in the ProPS method include three infrared channels ( $8.7 \mu\text{m}$ ,  $10.8 \mu\text{m}$ , and  $12 \mu\text{m}$ ), two visible channels ( $0.6 \mu\text{m}$  and  $1.6 \mu\text{m}$ ), and a local texture parameter derived from the  $10.8 \mu\text{m}$  channel.

The cloud top phase retrieval begins with computing a prior probability of cloud and phase occurrence from the DARDAR data. This probability is then iteratively updated using a Bayesian approach with each successive SEVIRI instrument. The outcome is a probability for clear sky and each cloud top phase. The phase with the highest probability is then identified as the result for each SEVIRI pixel. Based on the study conducted by Mayer et al. [37], the daytime results demonstrated success in detecting clouds, accurately identifying 93% of cloud pixels and 86% of clear sky pixels. When it comes to determining the cloud top phase, the algorithm achieved accuracy rates as follows: 91% for IC, 78% for TI, 52% for MP, 58% for SC, and 86% for LQ clouds.

## 4 Data evaluation

The last chapter introduced two cloud measurement instruments: the CIP and the HSI. A transition is made from theory to practical application in this chapter. To obtain accurate measurements of icing conditions in general and specifically of Appendix O conditions, data from these instruments need to be evaluated and a combined size distribution needs to be established. Therefore, filters and corrections applied to the CIP data are presented based on the measurement uncertainties described in the previous chapter. Lastly, requirements set to determine Appendix O icing conditions are explained.

*The data evaluation of the HSI is not covered in this study because it is performed with the data recording and imaging processing software AIMS (The Artium Integrated Management System Software), which eliminates the need for additional data evaluation procedures.*

### 4.1 Description of the dataset

The flight dataset is collected using three main instruments: CIP, CDP, and Nevzorov. A brief description of these instruments can be found in Section 1.3. It is worth noting that the data evaluation for Nevzorov and CDP is outside the scope of this study and is undertaken by a separate researcher.

Particle size, concentration, and LWC measurements are conducted using a combined dataset from the CDP and grayscale CIP. Detailed information on the CIP is available in Section 3.1. During the campaign, the imaging threshold of the CIP is set to 50%. The second instrument, Cloud Droplet Probe (CDP), is a scattering probe that determines particle size by measuring the intensity of forward scattered light using a photodiode [38]. The measurement range of the CDP covers particle sizes from 2 to 50  $\mu\text{m}$ , providing a combined size range of 2-960  $\mu\text{m}$  with the CIP. The CDP does not provide information about particle shape. For analysis purposes, all measured particles by the CDP are assumed to be liquid due to the rapid growth of ice crystals. In the case of the CIP, the shape information is only applicable for larger particles due to the resolution of the instrument.

The reference measurement of water content measurements (LWC and TWC) was conducted using the Nevzorov constant-temperature hotwire instrument. The instrument is equipped with two types of sensors: one for LWC and the other for TWC. The LWC sensor has a cylindrical shape to collect liquid droplets, while the TWC sensor is designed as a concave

cone capable of efficiently collecting all cloud particles. Additionally, the probe carries a reference sensor, which is shielded from the cloud particle impact and measures only convective heat losses, while the LWC and TWC sensors interact with cloud particles and additionally measure the heat loss by evaporation. The operation principle is based on measurements of power needed to compensate for heat losses on the collector sensor. More information on the Nevzorov probe can be found in Korolev et al. [39].

## 4.2 Evaluation procedure of the CIP data and applied corrections

The CIP saves the 1D dataset in a raw file and the 2D dataset in an image file. In order to obtain an extensive data evaluation, 2D data is used for the derivation of cloud microphysical properties. However, the 2D data requires correction to ensure accurate cloud measurements. In this study, the analysis of processed particle images and the data evaluation are conducted using Python scripts.

### 4.2.1 PAS correction

The CIP relies on the aircraft's speed to accurately determine the sample volume and derive cloud microphysical parameters, as detailed in Section 3.1.5. Throughout the campaign, the particle air speed (PAS) was fixed at  $120 \text{ m s}^{-1}$  due to the malfunctioning pitot tube of the probe. This setting ensured that the CIP's recording speed was always higher than the aircraft's velocity. Otherwise, using a low PAS value could result in the inability to record particle images at higher aircraft speeds because the recording speed of the probe depends on the configured airspeed. However, as the aircraft's speed varies during flight, applying a PAS correction is necessary to obtain precise measurements.

To implement the correction, true airspeed data is retrieved from the aircraft data file provided by SAFIRE. The PAS correction factor is then calculated as the ratio of the instantaneous true airspeed when the particle is recorded to the set probe speed ( $120 \text{ m s}^{-1}$ ). This correction factor is subsequently utilized to narrow down the particle shadow image when the true airspeed is lower than the set speed. The equation below shows the calculation of the PAS correction factor. Note that particle images cannot be corrected when the airspeed is higher than the configured airspeed.

$$\text{PAS Correction Factor} = \frac{\text{True Air Speed}}{120 \text{ m s}^{-1}}$$

### 4.2.2 Correction of missed particles due to dead time

The CIP applied a time stamp to the beginning and end of each buffer during measurement as explained in Section 3.1.5. Although the CIP does not record images in the overload, particles are still processed by a 16-bit particle counter. The 1D component of the probe is still incremented when at least one photodiode is occulted by the defined threshold. Therefore, dead time can be estimated based on the number of missed images:

$$\Delta t_{dead} = \Delta t \cdot (1 - N_{image}/N_{all}) \quad (5)$$

In this formula,  $\Delta t_{dead}$  is the estimated dead time in seconds,  $\Delta t$  is the time period when the buffer is recorded,  $N_{image}$  is the number of images recorded by CIP, and  $N_{all}$  is the number of particles counted by the 1D component of the probe. Based on this equation, the following strategy is proposed for the correction of missed particles:

1. Calculate particle count per second by 1D and 2D components.
2. Use the equation above to find the dead time at each second.
3. Adjust the sample volume by  $SV_{new} = SV_{old} \cdot (1 - \Delta t_{dead})$

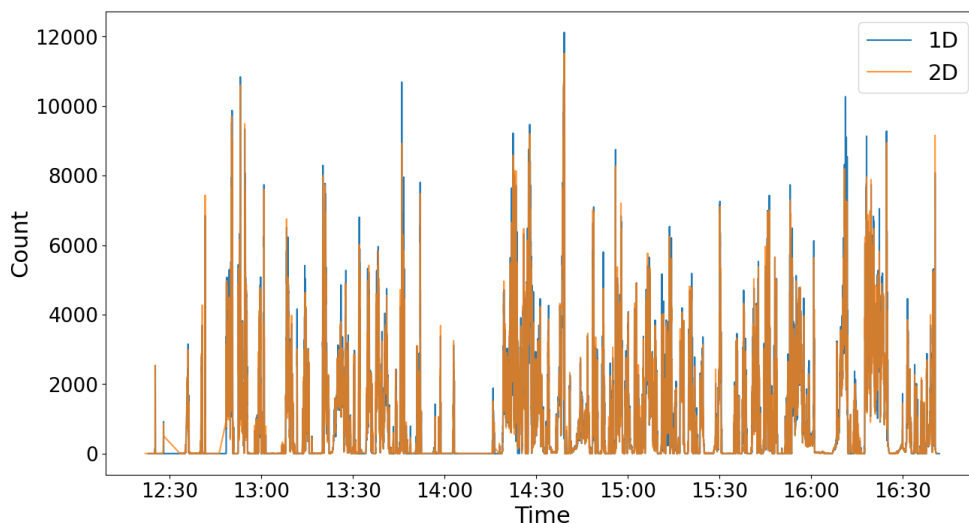


Figure 28: Comparison of particle count from 1D and 2D data

Nevertheless, this correction is not applied in this study since the percentage of missed particles is found as  $\sim 1\%$  as shown in Figure 28. This can be explained by having a newer generation CIP with a faster response rate and relatively lower speed of the aircraft during measurements.

### 4.2.3 Filtering usable data

The CIP provides a particle-by-particle file of the 2D images recorded during the flight. However, these images contain noise by measurement artefacts that can lead to errors in the data evaluation. The initial processing steps remove noise, stuck bits, and nonusable images from the dataset. Various filters have been created to eliminate particle images that are not relevant to the data evaluation, outlined as follows. Figure 29 illustrates examples of images removed by these filters.

*It is important to note that the grayscale threshold encompasses pixels containing all particles above the specified threshold value. For instance, when referring to pixels at a 50% grayscale level, this includes pixels at both 50% and 75% grayscale levels.*

- **1:** Particles that are partially out of the frame by checking whether 50% grayscale level pixel borders are in the frame or not. Size and phase estimation can only be made if the particle is completely imaged. This involves droplets that are imaged out of the frame and large ice crystals.
- **2:** Stuck bits, which are set once to a value but get stuck after that, creating artificial long lines in the image frame. The filter excludes particles if their aspect ratio (ratio of the width to height) at 25% grayscale level is more than 3 and all pixels are at a single grayscale level of 25% or 50%.
- **3:** Particles that have less than 5% pixels at 25% grayscale level and particles that have less than 10% pixels at 50% grayscale level to remove noise and stuck bits.
- **4:** Particles with width and height equal to one or two pixels at 25% grayscale level to remove very small particles since they do not provide reliable information. The small particle range is covered by the CDP.
- **5:** Particles that lack cloud particle characteristics are removed, such as those consisting entirely of pixels at the 50% grayscale level or have an aspect ratio of more than 6.

Once particles have been filtered and non-relevant data removed, the next step involves processing the remaining shadow images using 2D data analysis script. Further particle properties are calculated based on each imaged particle's shape property, such as the arrival time, size, size of the Poisson's spot, aspect ratio in each grayscale level, and aspherical fraction. These properties are later used to identify SLDs and other cloud conditions.

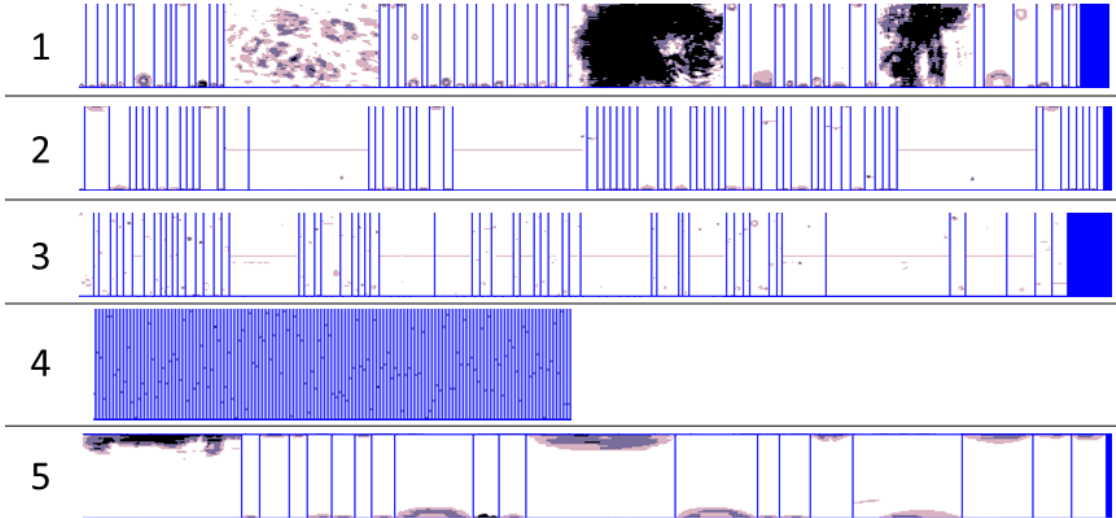


Figure 29: Example images that are removed by the above-mentioned filters respectively.

#### 4.2.4 Depth of field comparison for the CIP and selection of particle rejection mode

As discussed in Section 3.1.3, accurately setting the depth of field (DOF) value is essential for Optical Array Probe measurements, as it directly impacts the determination of the sample volume and, consequently, cloud measurements. The DOF of the probe should be selected, ensuring it is small enough to exclude highly out-of-focus particles for precise phase determination. This consideration arises from the fact that the discrimination of liquid particles relies on their spherical shape. If out-of-focus droplets lack a sharp edge in the image, it introduces potential uncertainty in phase detection. Conversely, the DOF should be sufficiently high to capture the majority of particles passing through the laser beam, facilitating robust statistical assessments. The depth of field is determined by the coefficient  $c$  in equation 4. In this context, the particle rejection modes and their corresponding coefficient values are drawn from the paper by Lyle Lilie [27], who proposed three distinct particle rejection modes outlined below:

- **Mode 1:** Accepting particles that has at least one pixel at 50% shadow level. ( $N_{50} > 0$ ), corresponds to  $c$  value of 8.18.
- **Mode 2:** Accepting particles that has at least one pixel at 75% shadow level. ( $N_{75} > 0$ ), corresponds to  $c$  value of 3.68.
- **Mode 3:** Accepting values when the ratio of pixels at 75% shadow level to pixels at 50% level is 0.5. ( $N_{75}/N_{50} > 0.5$ ) It corresponds to a much lower  $c$  value of 0.9.

In other words, the depth of field is the biggest in Mode 1 and lowest in Mode 3. As the depth of field decreases, particles that are considered in the analysis decrease as fewer particles pass through the narrower sample area. On the other hand, measurement accuracy improves because out-of-focus particles are ignored. The dependency of the DOF on the droplet diameter for each mode is shown in Figure 16, together with the theoretical plots of each corresponding coefficient value.

In order to decide on the DOF mode selection, a section of the CIP data that contains small droplet concentrations in the first section and large droplet concentrations in the latter section is used. LWC measurement provides insights into both concentration and droplet size within their specified sample volumes. Therefore, the behaviour of particle rejection Modes for LWC measurements is investigated. The section starts at 13:20 UTC and ends at 13:29 UTC. As depicted in Figure 30, there is a high concentration of small droplets between 13:20 and 13:22, whereas a high concentration of large droplets is observed between 13:24 and 13:27.

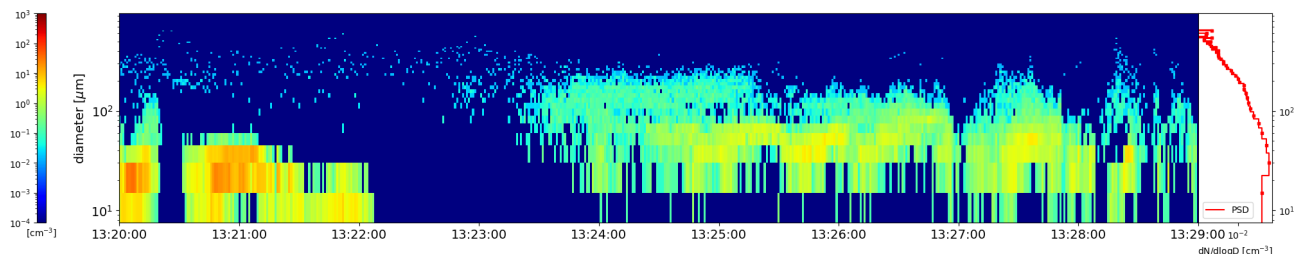


Figure 30: Droplet size distribution measured by the CIP over time in the selected section of the flight. The colour code represents the particle number concentration.

In Figure 31, the water content measurements from CIP modes and of the Nevzorov probe can be observed. This observation is supported by the plot of the normalized size distribution of the three CIP modes and the CDP on the right side of the figure. Plots of the CIP modes closely match after the droplet diameter reaches approximately  $100\ \mu\text{m}$ . However, the overlap between Mode 1 and the CDP is better than other modes at smaller size range. Consequently, it has been decided to use Mode 1 for particles smaller than  $90\ \mu\text{m}$  and Mode 3 for particles larger than  $90\ \mu\text{m}$ . The choice of  $90\ \mu\text{m}$  is based on it being a multiple of the instrument's resolution, which is  $15\ \mu\text{m}$ .

This decision strategy is based on several considerations. Given that ice particles tend to grow rapidly, it is unlikely that they will remain small. Additionally, the CIP's  $15\ \mu\text{m}$  resolution makes it challenging to discriminate water and ice particles at a small size range.

Therefore, phase discrimination is not needed for particles smaller than 90  $\mu\text{m}$  and they are assumed to be liquid. Mode 1 is selected for these particles to ensure a higher particle count and better statistical data. The size distribution plot on Figure 31 also shows the CDP measurements match well with Mode 1 measurements. On the other hand, for particles larger than 90  $\mu\text{m}$ , a more precise assessment of their phase is essential. By examining the section with a higher concentration of large particles in Figure 30, it becomes evident that there is no difference in the measured concentrations of all three modes. Hence, Mode 3 is chosen to make sure that particles are in-focus and can therefore be easily classified as SLD or ice crystals.

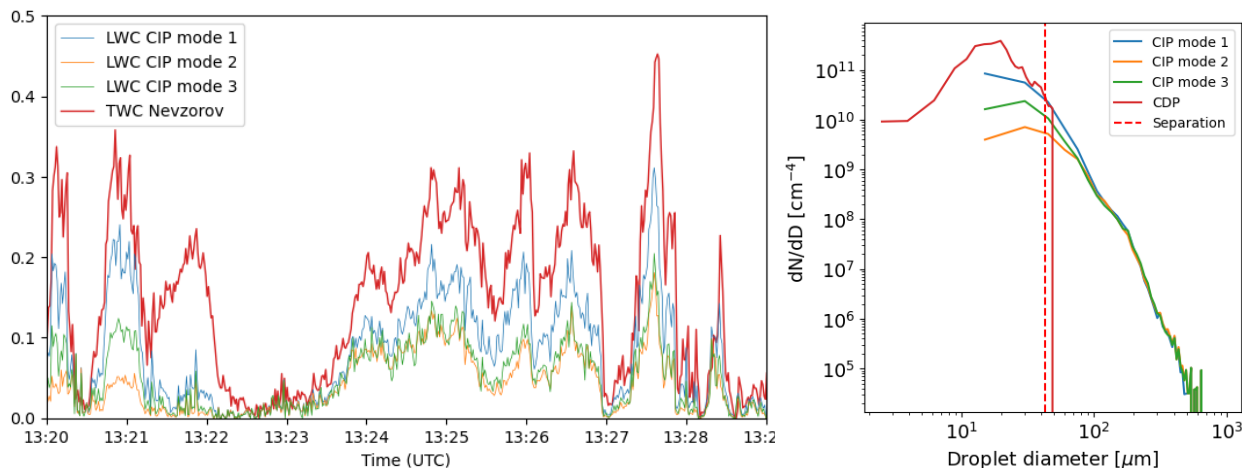


Figure 31: On the left side, water content measurements obtained from Nevzorov’s TWC cone and three CIP modes recorded between 13:20 and 13:29 UTC are presented. The right side displays the normalized particle size distribution derived from measurements made by the three CIP modes and the CDP during this time range.

Moreover, Figure 31 highlights the requirement for an instrument capable of measuring particle sizes below 15  $\mu\text{m}$  to provide a comprehensive particle size distribution. At 13:22, a high number concentration of small droplets is detected by the Nevzorov hot-wire probe, which the CIP is not able to detect. This discrepancy is due to the fact that small droplets fell outside the measurement range of the CIP. To cover the small droplet range, the CDP measurements are used as explained in the following sections in detail.

#### 4.2.5 Filtering SLDs from the CIP data

Several filters are established to detect SLD from the dataset, the particles that meet all conditions listed below are classified as SLD. Parametrization of particle properties is taken from Korolev et al. [40].

- The number of pixels occupied by a particle should be equal to or greater than 30. To illustrate, a particle with a three-pixel radius corresponds to a diameter of 90  $\mu\text{m}$ . This calculation, based on  $\pi \cdot 3^2$ , indicates that a minimum of 30 pixels are required to represent a 90  $\mu\text{m}$  droplet.
- The ratio of the shaded surface within the smallest enclosing circle (minus the Poisson spot if detected) should be equal to or greater than half of the total circular surface area to filter out non-spherical and out-of-focus particles.
- Droplet diameter in pixels after Korolev correction (SODA diameter) should be equal to or more than 6, corresponding to 90  $\mu\text{m}$  diameter.
- The width of the particle above 50% grayscale threshold should be less than 64 to ensure that the particle image is smaller than the probe's maximum size measurement capability.
- The ratio of shaded surface within the area of 90% of the enclosing circle radius should be more than 20% to eliminate non-spherical particles.
- Dimensionless Fresnel diffraction parameter, denoted as  $Z_d$ , should have a value greater than 0.5. This parameter defines the distribution of intensity in the diffraction image of the particle and helps filter out particles that are not sufficiently in-focus. The definition of the parameter is  $Z_d = 4\lambda Z/D_0^2$  in [40], where  $Z$  is the distance from the object plane,  $D_0$  is the actual diameter of the droplet, and  $\lambda$  is the wavelength of the light.
- The ratio of shaded surface within the area between 0.75-radius and full radius should be more than 40% to eliminate out-of-focus particles.
- The aspect ratio of the image created by pixels at 50% grayscale threshold should be more than 0.8 to ensure that filtered particles are spherical.
- The static air temperature recorded at the time of particle detection should be more than  $-32^\circ\text{C}$ , as particles cannot remain in a supercooled phase below this temperature.

While the filters demonstrated effective performance, as illustrated in Figure 32, the detection of SLDs is somewhat compromised by certain factors that influenced the accuracy. As previously discussed, SLD particles that are out-of-focus may not be recognized as SLDs or classified as ice crystals despite the narrowed depth of field, while ice crystals might be misclassified as SLDs. Another contributing factor is the missed detection of SLD due to

the coincidence of two particles. When particles overlap within the same image frame, they introduce non-spherical characteristics during the filtering process. Example images of both false detection cases are shown in Figure 33.

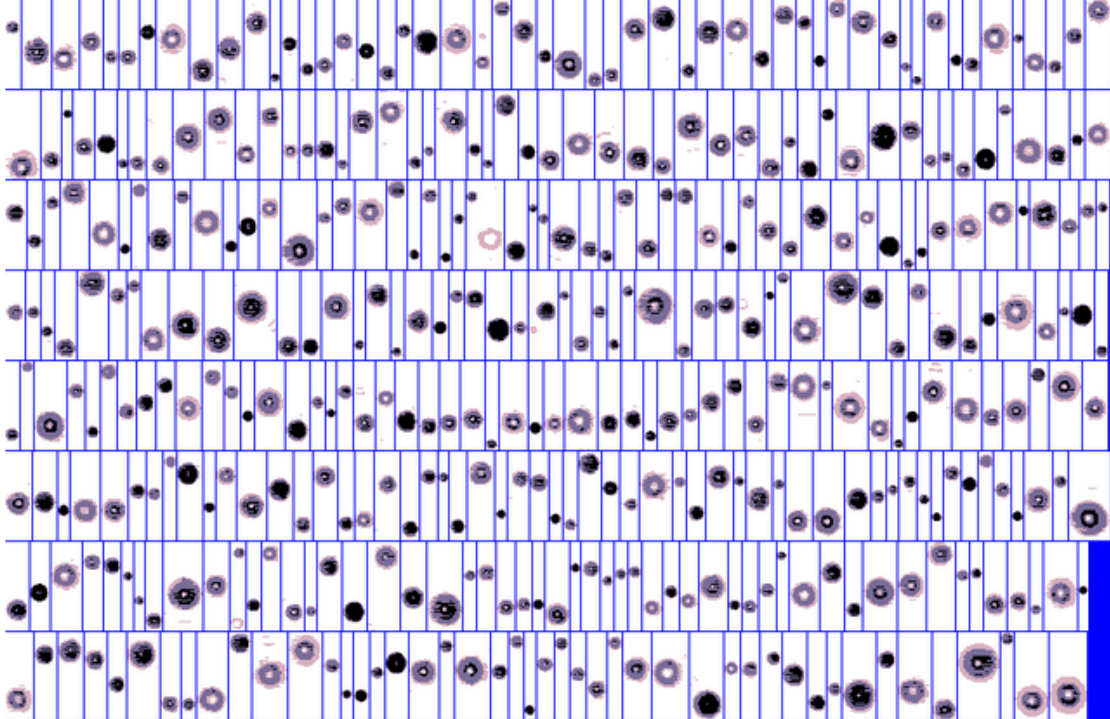


Figure 32: Supercooled large droplets detected during the selected flight on 24 April 2023 at 12:49

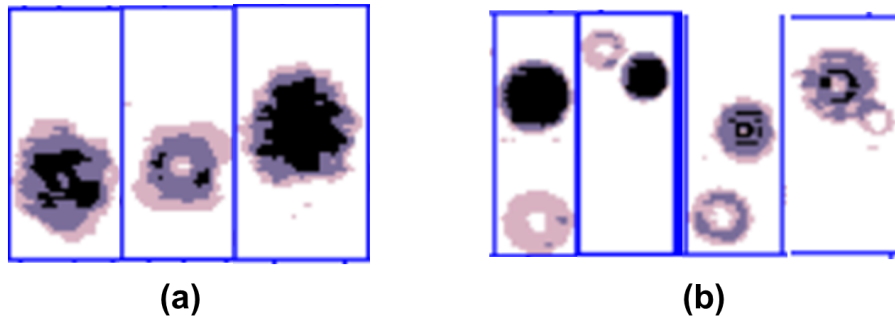


Figure 33: Ice particles classified as SLD due to being out-of-focus (a), and SLD particles erroneously categorized as "ice" due to the coincidence of two droplets within the same image frame (b).

### 4.2.6 Creating the combined size distribution

A combined size distribution from both the CDP and CIP is required for a comprehensive evaluation of particle size distribution. Given the overlapping measurement ranges of the two probes between 15 and 50  $\mu\text{m}$ , it's necessary to define a threshold for separating the data. In this study, CDP data is used up to a particle diameter of 43  $\mu\text{m}$ , while the CIP data is used for larger particles. Considering the CIP's 15  $\mu\text{m}$  resolution, only particles with a minimum size of three pixels, corresponding to 45  $\mu\text{m}$ , are used in the evaluation. After applying data corrections, the combined size distribution of the CDP and CIP is divided into 1  $\mu\text{m}$  bins for normalization. From these higher-resolution size distributions, a cumulative mass distribution is derived, enabling the calculation of the median volume diameter and the maximum drop diameter, as explained in Section 2.1.

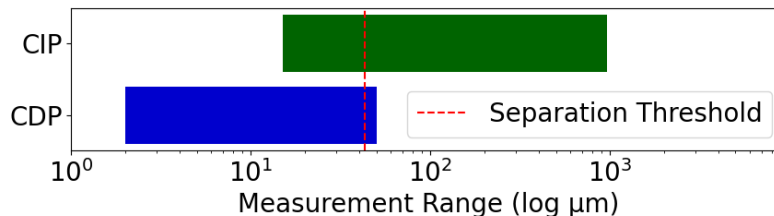


Figure 34: Measurement range of the CDP and CIP probes with separation threshold of 43  $\mu\text{m}$  shown by the red dashed line.

The data combining measurements from the CDP, CIP, and Nevzorov is averaged in sequential 30-second intervals, corresponding to a horizontal length scale of  $3.6 \pm 0.3$  km with the assumption of an average aircraft speed of  $120 \text{ m s}^{-1}$ . Time averaging has to be made for deriving LWC and MVD to ensure good statistical data. This is due to the fact that SLDs are relatively rare in clouds. 30 seconds of averaging time is chosen because it represents a short averaging scale and provides sufficient measurement data for statistical significance as explained in Cober et al. [41]. Although the data points are available for each second, computed values represent the averaged value in the -15/+15-second intervals around the data point to provide stable values of the microphysical properties. Additionally, the volume diameter of 99 percentile (VD99) is taken as the maximum drop diameter as it removes high outliers from the data and provides good statistics.

### 4.3 Assessment of Appendix O environments

The following conditions are applied to the resulting flight data to determine Appendix O encounters that contain SLD:

- **SAT < 0°C:** The ambient temperature needs to be lower than the melting point. This condition is necessary to take only supercooled cloud measurements into account.
- **Hotwire LWC 30s > 0.025 g m<sup>-3</sup>:** The LWC must be more than 0.025 g m<sup>-3</sup>, which is the lowest LWC value that can be measured by the Nevzorov probe. The purpose of defining this filter is to avoid false cloud detections.
- **LAS N 30s < 1 L<sup>-1</sup>:** It was found in Cober et al. [42] that the droplet spectrum is dominated by ice crystals for sizes greater than 35 μm when their concentration exceeds to 1 L<sup>-1</sup>. This is why the ice crystal concentration has to be less than 1 L<sup>-1</sup>. The accurate measurement of droplet concentration and size, as well as obtaining particle size spectra, is only feasible under such low ice particle concentrations with the current instrumentation.
- **LWC SLD 30s > 1% · LWC 30s:** The LWC within the SLD should be larger than 1% of the total LWC. This condition is established in Cober & Isaac [5] to ensure that the maximum droplet diameter (VD99) is larger than 100 μm and only conditions with a significant portion of liquid water contained in SLD are considered.
- **SLD N 30s > 10 · LAS N 30s:** The concentration of SLD must be at least 10 times more than the ice crystal concentration to prevent spherical ice from being defined as SLD.
- **SLD N 30s > 100 m<sup>-3</sup>:** There must be more than 100 SLD in 1 m<sup>3</sup> to avoid occasional occurrences of large droplets, which could occur outside of clouds in a weak drizzle.
- **Hotwire LWC 30s > 0.4 · Hotwire TWC 30s:** The liquid water content should be larger than 40% of the total water content to avoid conditions with a significant amount of ice crystals.
- Duration of the encounter should be at least 5 seconds long to avoid rapidly changing cloud parameters in patchy cloud systems.

By limiting the number of ice crystals that can be present in comparison to the number of SLD, the interpretation of glaciated or mixed-phase conditions as SLD is avoided. However,

this also means that conditions, where large ice crystals and SLD coexist, cannot be detected with this approach. This data evaluation represents encounters with only pure liquid clouds.

Encounters that do not satisfy the previously outlined requirements but exhibit a liquid water content exceeding  $0.025 \text{ g m}^{-3}$  at temperatures below 0 degrees Celsius are categorized as Appendix C conditions.

#### 4.4 Comparison of water content measurements between Nevzorov and CIP instruments

As Appendix O icing encounters are detected by the filters explained in the previous section, a comparison of the LWC measurement from CCP (CDP and CIP) with the LWC and TWC measurements obtained from the reference Nevzorov hot-wire probe is conducted. The data utilized was obtained from the observational flight on April 24, which will be extensively discussed in the following chapter.

The research conducted by A. Isaac [40] has shown that large droplets tend to splash upon impact with the LWC sensor, potentially leading to mass loss as the splashed droplets may re-impinge on the surface or be carried away from the surface by airflow. Therefore, it is known that the LWC of larger droplets, including SLD, is underestimated by the LWC sensor of the Nevzorov probe due to the splashing effect. The TWC sensor is not susceptible to splashing effects due to its conical shape that captures all impinging particles [43]. Hence for the comparison, the TWC measurements from the Nevzorov probe are also considered with an assumption that all particles are in a supercooled liquid phase. Therefore, no ice crystals are assumed to be present in the identified Appendix O icing encounters. The results of this comparison are depicted in Figure 35.

On the right side of the figure, a good agreement is observed between Optical LWC (Measurements by the CDP and CIP) and Nevzorov LWC measurements, as indicated by the regression line with a slope of  $a = 1.02$ . Conversely, the left-side plot illustrates that the CCP underestimates the LWC compared to the TWC component of the Nevzorov probe, with a regression line slope of  $a = 0.58$ . This discrepancy between the LWC and TWC components of the Nevzorov probe can be attributed to the splashing effect and low collection efficiency of the Nevzorov probe's LWC sensor, emphasizing the importance of comparing with TWC measurements for improved accuracy. It is also important to note that the Appendix O filter is not flawless and measures a small portion of ice crystals in addition to

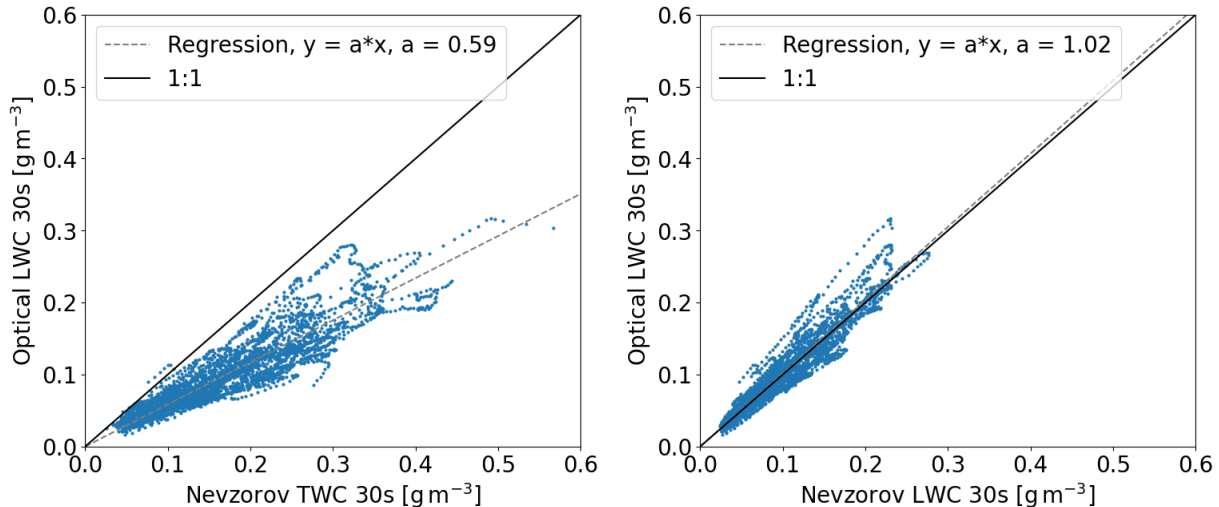


Figure 35: The left plot shows comparison and linear regression of Optical LWC and Nevzorov hot-wire TWC measurements, whereas the right plot shows the comparison with Nevzorov LWC measurements.

supercooled liquid droplets as explained before. Nevertheless, a clear observation emerges that optical LWC measurements by the optical measurements exhibit underestimation. This is because of the good agreement of optical measurements with the Nevzorov LWC measurements despite splashing. Since the optical measurements are lower by a bias factor than the Nevzorov TWC measurements, this case can be defined as a systematic error.

#### 4.5 Comparison of measurements between the CIP and the HSI

For a visual comparison of particle images by the CIP and the HSI, an Appendix O encounter between 16:08:59 - 16:12:02 UTC from the flight on 24 April 2023 is selected. Flight profile and cumulative mass distribution of the encounter together with the LWC, MVD, altitude, and temperature plots are given in Appendix A of this study. The rationale for selecting this encounter is its long duration and substantial existence of large droplets, evident in their cumulative mass distribution and particle images taken during the encounter.

The HSI probes are supplied with a filter formula that is defined after the factory calibration. In order to filter out particles that are in-focus, the recommended filter formula by the probe manufacturer is used on the flight data:

$$\text{IntensityMean} \leq 130 \text{ and GradientMean} \geq 150 \text{ and MeanDiameter} \geq 3 \mu\text{m}$$

The 'IntensityMean' in this formula refers to the average intensity within the outlined parti-

cle area, ranging from 0 to 255. Lower intensity values indicate particle regions that obstruct more light. 'GradientMean' represents the average gradient value along the particle border, serving as an indicator of particle focus, where higher values signify better focus. 'MeanDiameter' denotes the average particle diameter in  $\mu\text{m}$ . The software AIMS (provided by the probe manufacturer) identifies the area inside the outlined particle border as the region of interest (blobs).

During the encounter, the CIP recorded 633,326 cloud particles, and after applying filters, 294,389 particle images remained in the CIP data. On the other side, the HSI captured 15,241 particles within the same time frame and 754 images remained from the data. This discrepancy is primarily due to the HSI's smaller sample volume and the low frame rate set to 100 Hz to prevent memory buffer overflow. While increasing this frame rate is an option to improve counting statistics and SLD detection by the HSI, it should be noted that the results would only exhibit a linear increase with the higher frame rate. Therefore, this approach alone may not be adequate to effectively address the issue.

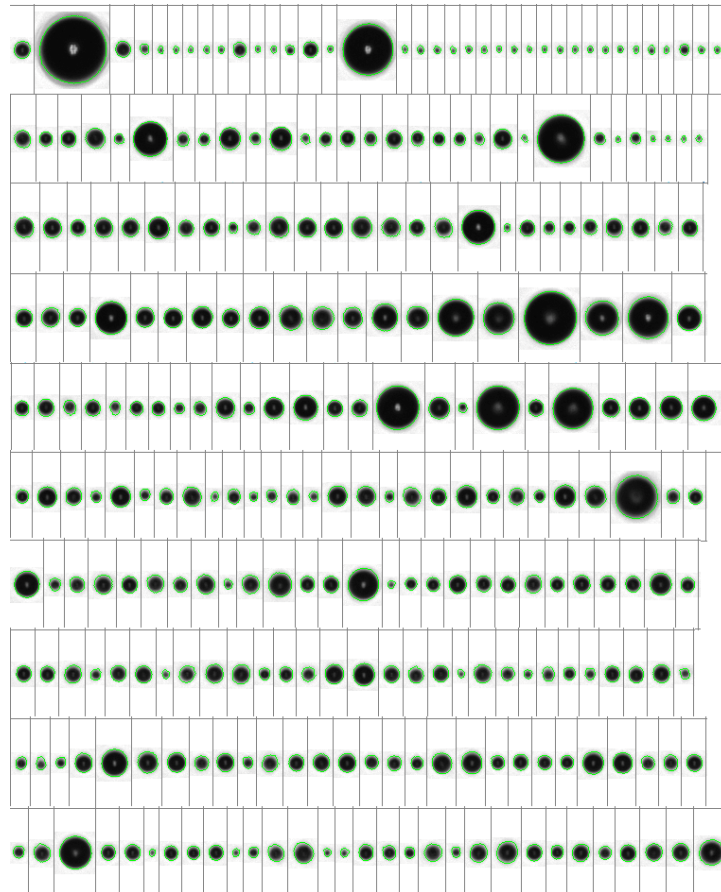


Figure 36: Valid particle images captured by the HSI within the time frame of 16:08:59 to 16:12:02 UTC. The largest droplet diameter is 214.6  $\mu\text{m}$  and the smallest is 24.3  $\mu\text{m}$ .

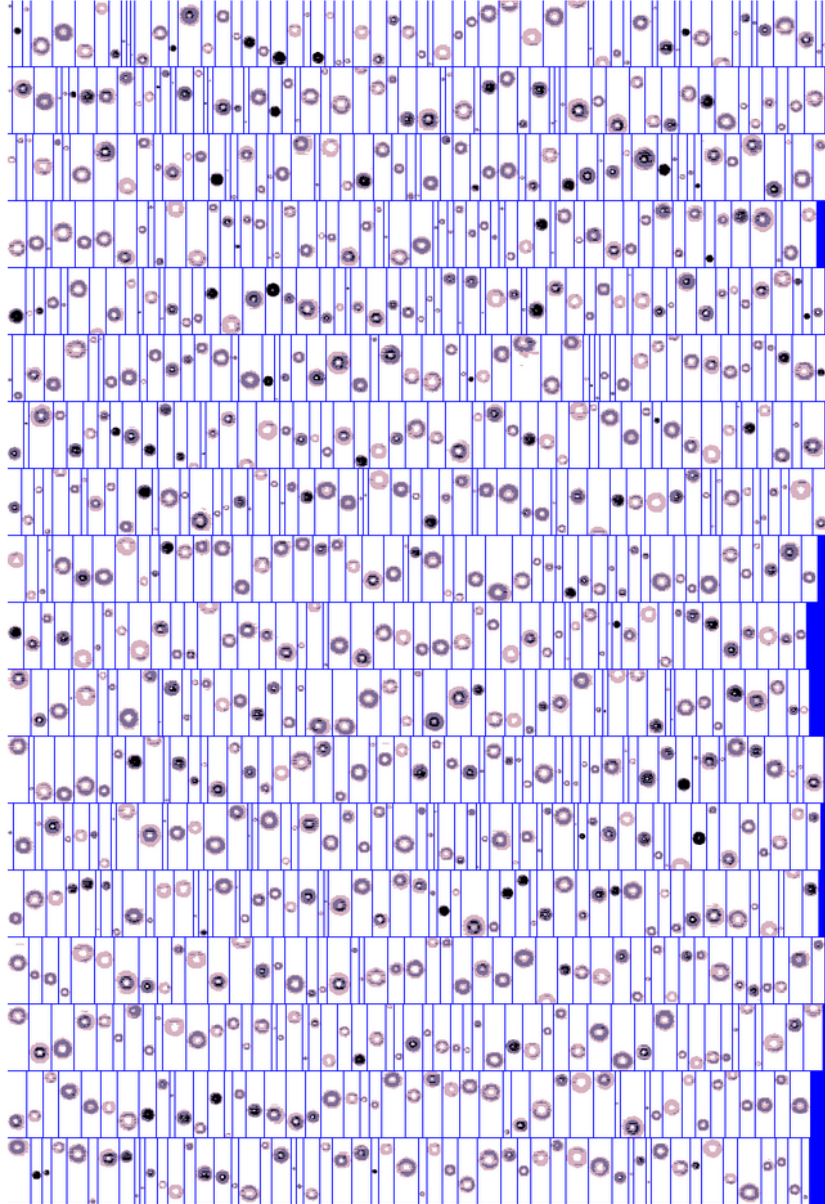


Figure 37: Examples of the filtered particle images captured by the CIP within the time frame of 16:08:59 to 16:12:02 UTC.

Figure 36 displays valid images captured by the HSI during the encounter, whereas Figure 37 shows 1000 randomly selected particle images by the CIP within the same time frame. Images by the HSI exhibit high-resolution particles compared to the CIP, providing a clear discrimination between ice and liquid cloud particles. This serves as validation for the process used to identify Appendix O encounters with the combined data of the CDP and CIP. It can also be seen that Poisson's spot is small enough to be neglected.

To assess the differences in measurement characteristics between the CIP and HSI, a comparison of particle number concentration measurements during the selected encounter is depicted in Figure 38. The plot illustrates that the HSI measurements show larger values of concentration and exhibit abrupt fluctuations. In contrast, the CIP yields more consistent measurements over time. Larger fluctuations of the HSI measurements are because of its small sample volume, reducing the likelihood of encountering particles. Additionally, Figure 39 presents a comparison of the normalized particle number density distributions obtained from both instruments. The HSI data offers a number density histogram with a user-defined size bin width set at  $15\ \mu\text{m}$  to ensure comparability with the CIP data.

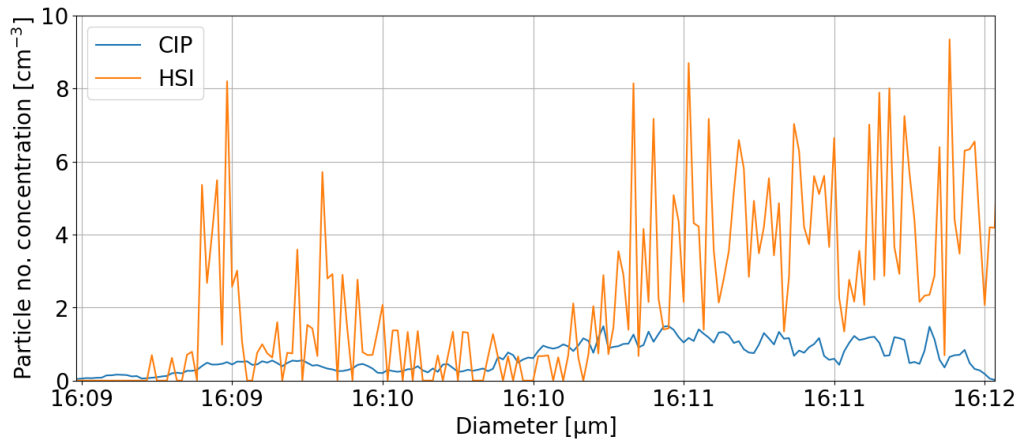


Figure 38: Particle number concentration measurements of the CIP and the HSI between 16:08:59 - 16:12:02 UTC.

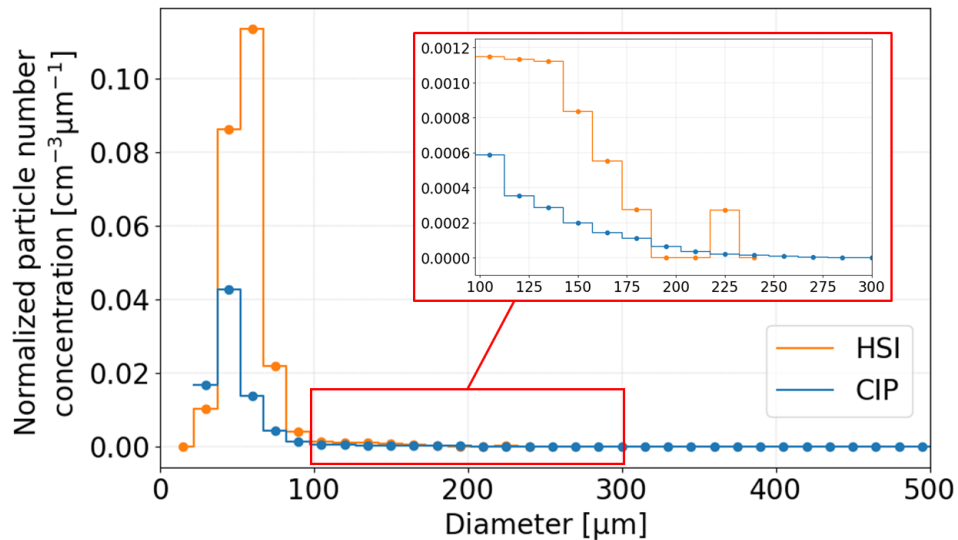


Figure 39: Normalized particle number concentration histogram of the CIP and the HSI with size bin widths of  $15\ \mu\text{m}$ .

The visualization reveals that the CIP presents a more uniform size distribution owing to its recording of a higher number of particles. On the other hand, the HSI only imaged one particle in the 225  $\mu\text{m}$  size bin and no other particles are recorded in size bins higher than 180  $\mu\text{m}$ . With a smaller measured volume, the influence of a single particle on the measurement values becomes more pronounced, reducing the smoothness of the data. Moreover, reduced sample volumes decrease the likelihood of particles being detected by the instrument. These factors contribute to the fluctuations observed in the concentration measurements and result in vacant size bins within the data. In order to obtain more robust statistical data in the HSI measurements, longer data acquisition durations or environments with a higher number concentration are necessary.

Another factor to highlight is the notable differences in concentration measurements between the two probes. During the encounter, the HSI frequently exhibits values approximately 2 to 3 times higher than those recorded by the CIP. The consequence can explain the underestimation of LWC measurements of the CIP compared to the Nevzorov probe. The underestimation of particle number concentration has a direct effect on the LWC measurements, as explained in Section 3.1.2.

## 5 Airborne in-situ measurements of SLD conditions

The objective is to gain an understanding of SLD in-flight icing conditions through the evaluation of data obtained from various instruments. Therefore, the data evaluation procedure presented in the previous chapter is applied to one selected flight of the SENS4ICE campaign, which is the ninth observational flight (OF9 according to the DLR Institute of Atmospheric Physics) performed on 24 April 2023. Firstly, meteorological conditions and flight profiles are introduced to give an overview of the flight. Measurement results and their statistical analysis are demonstrated. The data is used to investigate the cloud microphysical properties during Appendix O encounters together with the SLD contribution. Lastly, the obtained results are compared with MSG products for cross-validation.

### 5.1 Meteorological situation on 24 April 2023

Figures in Appendix B of this thesis present cloud data products recorded by the geostationary Meteosat satellite (MSG) at 14:00 UTC on 24 April 2023, depicting cloud top height, cloud coverage, and associated properties. Notably, the image reveals higher cirrus clouds partially obscuring lower-level clouds. Higher-level clouds can also be seen in Figure 40 taken during the flight.



Figure 40: Tops of measured clouds photographed during the selected flight on 24 April 2023 at 12:47 UTC. A thin layer of higher-level clouds is visible in the image.

Figure 41 illustrates the presence of an active front advancing from the ocean toward the

Southern region of France. As explained in Section 2.3, such active fronts possess the potential for icing events due to increased atmospheric lifting and abundant moisture, thus high LWC. Furthermore, the influx of clean marine air from the ocean further increases the likelihood of SLD formation. The warm air layer below the clouds provided an opportunity to deceive the aircraft, a prerequisite for executing the flight due to safety considerations.

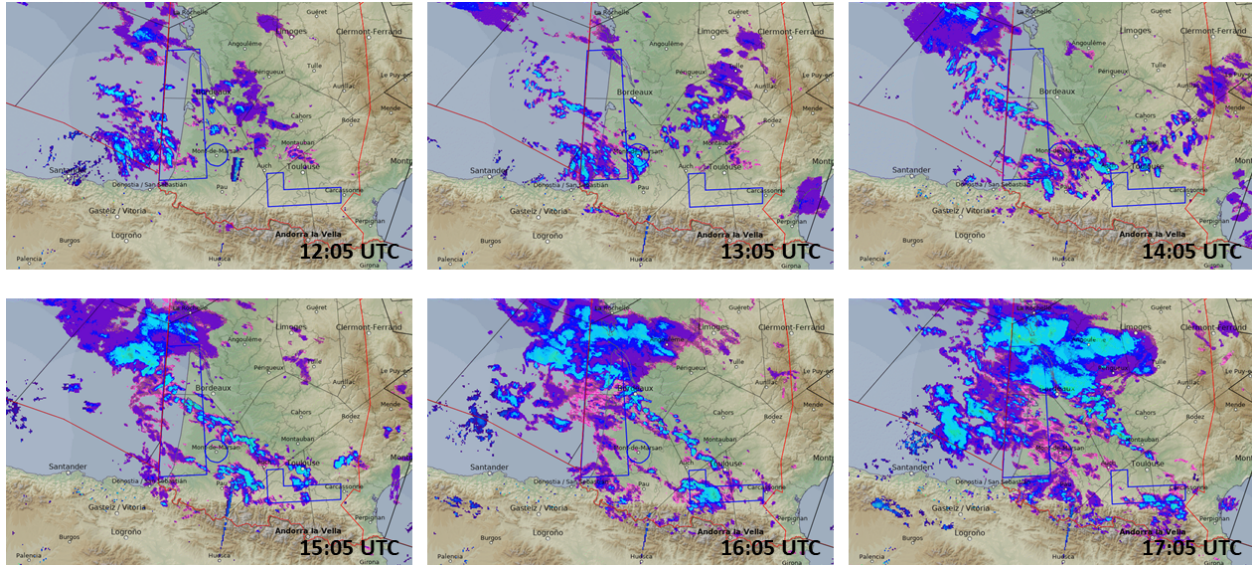


Figure 41: A radar reflectivity image at the flight zone on 24 April 2023 at 14:35 UTC. The image is provided by Alexandre Floutard in Météo France. Areas that are surrounded by blue lines show temporary reserved airspaces during the flight.

Radar images illustrate the magnitude of backscatter from the clouds, with strong returns indicating the presence of precipitation or large ice crystals within the cloud. In situations involving SLDs, radar echoes tend to be weaker, given that SLDs are smaller than raindrops but larger than cloud drops. Consequently, regions characterized by a purple or pink colouration on radar imagery are presumed to contain SLDs, leading to flight planning considerations.

## 5.2 Flight track and measurement results

The flight started from Toulouse Franczal Airport (LFBF) at 12:22 UTC to intercept the incoming warm front situated over the Atlantic Ocean in proximity to the French coastline. Subsequently, the aircraft pursued a Lagrangian flight pattern, following the cloud system as it progressed inland for several hours. The aircraft then proceeded to the temporary reserved area (TRA) located in the southeastern region of Toulouse near the Pyrenees to measure the orographic lifting effect on the system. Within this airspace, multiple loops were executed

and then returned to Francazal Airport at 16:52 UTC. Therefore, the probes were able to measure the same cloud system over the ocean, over the land, and lastly after the orographic lift by the mountains. The flight track is illustrated in Figure 42. Large and small droplet icing was detected by aircraft sensors and pilots several times according to the flight report released by the aircraft operator.

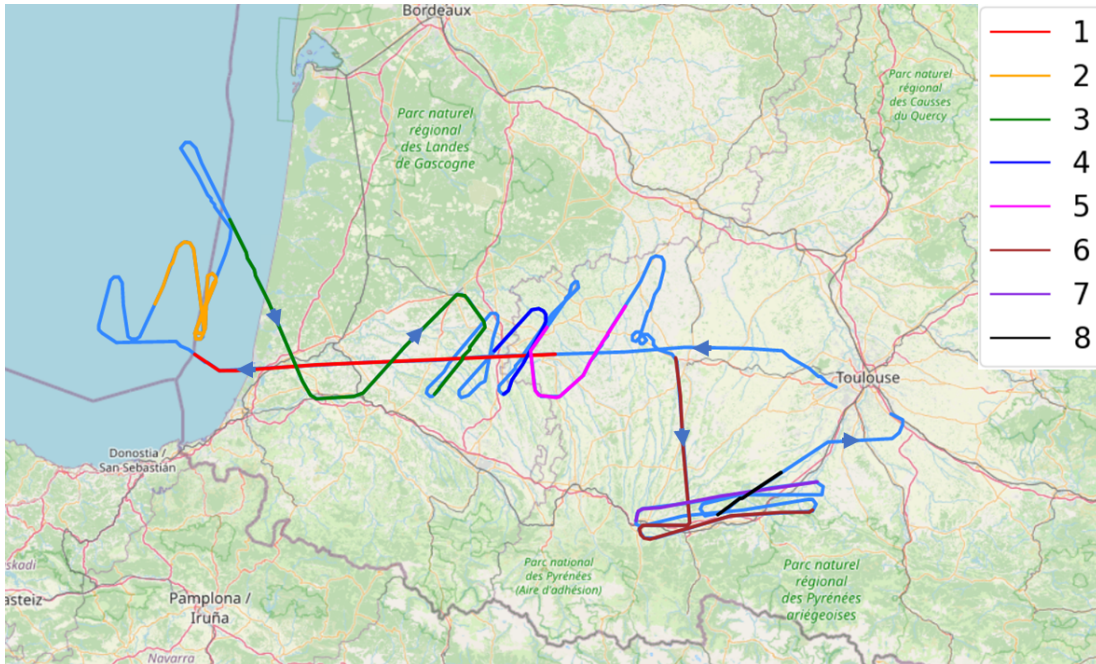


Figure 42: Flight track of the considered flight on 24 April 2023. Each cloud sampling segment is colorized and numbered.

Throughout the flight, cloud sampling primarily occurred at altitudes ranging from 3700 to 4700 meters, corresponding to temperatures fluctuating between  $-5^{\circ}\text{C}$  and  $-15^{\circ}\text{C}$ , as depicted in Figure 43, which provides the flight altitude profile and plots of measured cloud parameters. Sudden decreases and increases in altitude in the figure represent deicing cycles undertaken to avoid ice accumulation on the aircraft, ensuring safety and preventing sensor ice contamination.

Eight primary cloud measurements were carried out during the flight, with each measurement segment separated by deicing cycles. The first five measurements were performed within the period of the Lagrangian pattern towards inland, while the remaining three were taken in the TRA near the Pyrenees. Over the course of these measurements, a slight increase in LWC and MVD was noted, giving insights into the cloud system's evolution and the collision-coalescence process. The majority of the measured particles within the clouds were liquid droplets, although some mixed-phase conditions were observed particularly in proximity to

the Pyrenees in the TRA. This is mainly due to the orographic lifting system at the mountains, transporting ice nuclei upwards. An increase in ice crystal number concentration over time can also be observed due to the Wegener–Bergeron–Findeisen process, in which supercooled water droplets freeze upon contact with ice nuclei. These conditions can be seen in the sections of high ice concentration in Figure 43. However, these ice crystal observations were excluded from the data assessment.

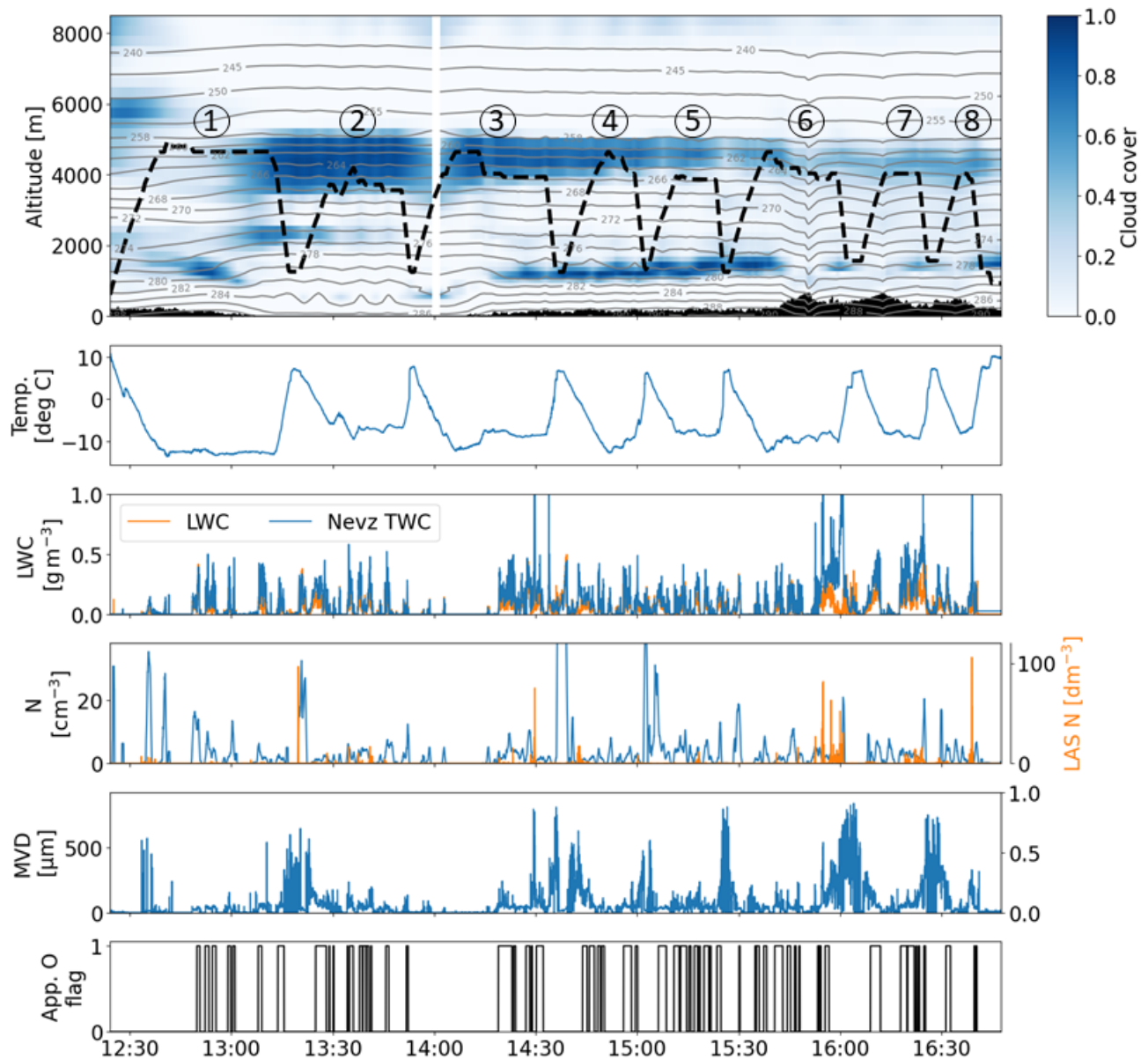


Figure 43: Flight altitude profile in ERA5 model, SAT, LWC, cloud particle concentration (N) and ice crystal (LAS) concentration, MVD, and Appendix O icing flag plots over time respectively from top to bottom during the flight. Every cloud sampling segment is identified with a number.

Figure 44 presents an overview of particle size measurements and their concentrations throughout the flight. Light-coloured areas above 40  $\mu\text{m}$  indicate the existence of large droplets and below indicate small droplets, whereas upper sections with lower concentrations indicate ice crystals with very high particle size. A noticeable step in the colour map occurs at 43  $\mu\text{m}$ , corresponding to the separation threshold between the measurement ranges of the CDP and CIP. Although the concentration measurements by the CDP exhibit higher values, the data appears more sparse due to its smaller sample volume, resulting in intermittent instances of zero values. In contrast, the CIP measurements demonstrate greater uniformity despite displaying lower values on the colour scale. Considering the measurement differences between the two probes, this step is not large in the particle size distribution graph (right side of the figure), which is an indication of the compatibility of the two datasets.

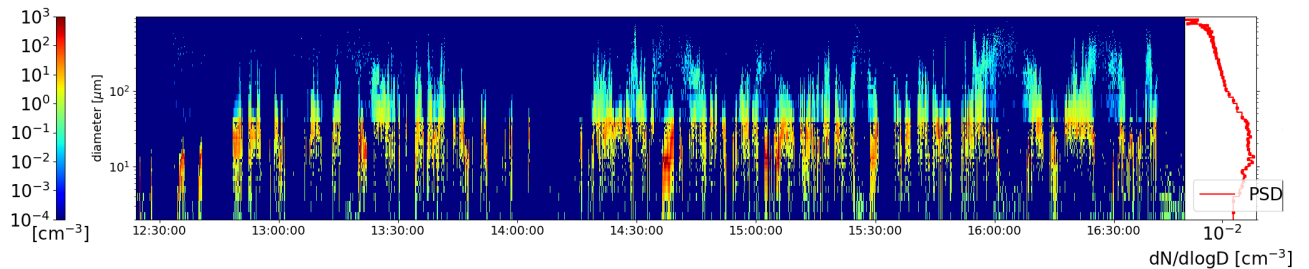


Figure 44: The quick-look plot of OF9 showing the profile of particle size measured with the colour code representing the number concentration. The plot on the right side shows the particle size distribution of all measurements.

The figure also illustrates the distinctive measurement characteristics of the two probes. The CIP exhibits lower particle number concentration and offers lower resolution, but is capable of measuring larger particle size range. Regions with high concentrations of small particles correspond to Appendix C icing conditions, while areas with elevated concentrations of larger particles represent Appendix O icing conditions. Regions with very high particle sizes are associated with ice crystals and are excluded from the analysis.

The characteristics of cloud encounters for each of the eight segments are as follows:

- **Segment 1:** The initial icing encounter occurred shortly after the aircraft entered the front system. It was observed at an altitude of approximately 4600 m, with a temperature of  $-12^{\circ}\text{C}$ , and MVD ranging from 28  $\mu\text{m}$  to 56  $\mu\text{m}$ . LWC ranged between 0.06 and 0.17  $\text{g m}^{-3}$ .
- **Segment 2:** This segment was measured at lower altitudes, between 3700 and 4000 m. The temperature ranged from  $-8$  to  $-5^{\circ}\text{C}$ , and MVD varied from 28 to 150  $\mu\text{m}$ . LWC ranged between 0.03 and 0.11  $\text{g m}^{-3}$ .

- **Segment 3:** No icing encounters were observed at altitudes of 4600 m. The aircraft then descended to altitudes around 3900 m with a temperature of around  $-8^{\circ}\text{C}$ . SLDs were detected, with MVD ranging between 41 and 183  $\mu\text{m}$ , and LWC between 0.04 and  $0.20\text{ g m}^{-3}$ .
- **Segment 4:** Measured at altitudes ranging from 3700 to 4400 m, with a temperature range of  $-6$  to  $-11^{\circ}\text{C}$ . MVD ranged from 40 to 120  $\mu\text{m}$ , and LWC ranged from 0.05 to  $0.12\text{ g m}^{-3}$ .
- **Segment 5:** Measured at altitudes around 3900 m with a temperature of around  $-8^{\circ}\text{C}$ . MVD ranged from 40 to 130  $\mu\text{m}$ , and LWC from 0.01 to  $0.12\text{ g m}^{-3}$ .
- **Segment 6:** The first measurement segment in the orographic system at TRA. Icing encounters were measured at altitudes ranging between 3800 and 4500 m, with a temperature range from  $-7$  to  $-12^{\circ}\text{C}$ . MVD ranged from 25 to 90  $\mu\text{m}$ , and LWC from 0.02

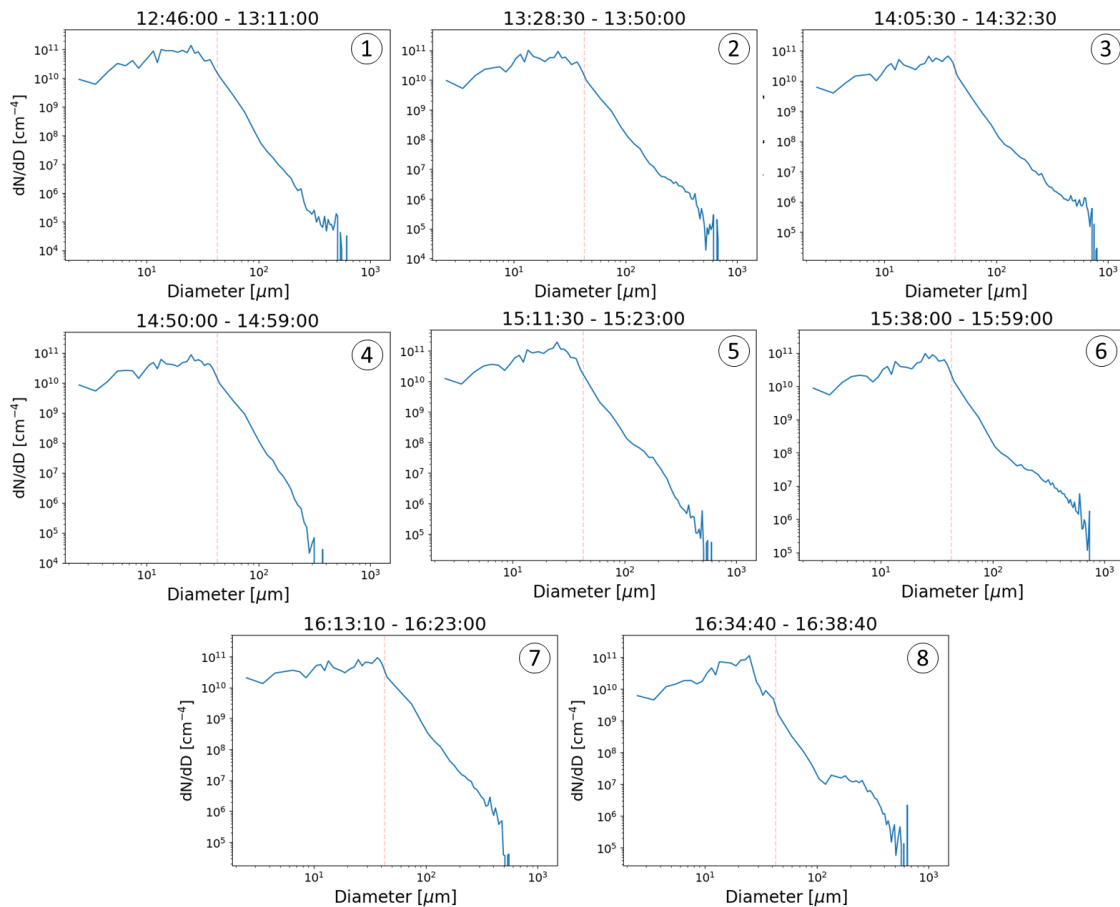


Figure 45: Particle size distributions for each segment respectively with red dashed lines showing the separation between the CDP and the CIP.

to  $0.25 \text{ g m}^{-3}$ .

- **Segment 7:** Measured at altitudes around 4000 m with a temperature of around  $-9^\circ\text{C}$ . MVD ranged from 50 to  $253 \mu\text{m}$ . The highest SLD concentration and LWC were observed in this segment, with LWC ranging between 0.10 and  $0.25 \text{ g m}^{-3}$ .
- **Segment 8:** Icing encounters were observed at higher temperatures, ranging between  $-0.5$  and  $-3^\circ\text{C}$ , at altitudes between 2600 and 3100 m. MVD ranged from 30 to  $94 \mu\text{m}$ , and LWC from 0.03 to  $0.12 \text{ g m}^{-3}$ .

*It should be noted that the CIP underestimates LWC and particle number concentration measurements as mentioned in the previous chapter, where CIP measurements were compared with the Nevzorov and HSI measurements.*

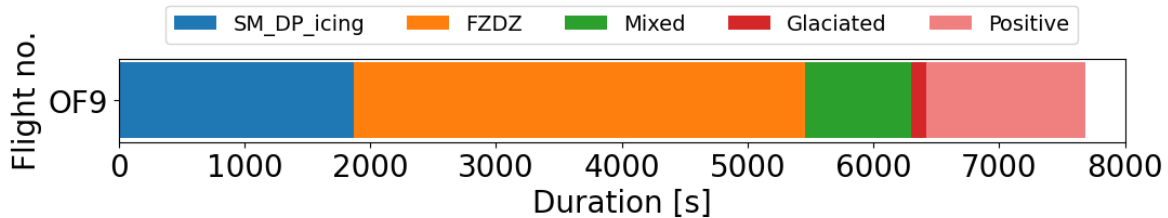


Figure 46: Durations of cloud encounter types in the chosen flight OF9.

Figure 46 provides a visual representation of the duration of different icing conditions observed during the selected flight. Freezing drizzle icing conditions dominated the observation, lasting for 59 minutes and 40 seconds. Small droplet icing followed, accounting for 32 minutes and 46 seconds of the total flight time. Encounters at positive temperatures were noted for 21 minutes and 3 seconds, while mixed icing conditions were observed for 14 minutes and 5 seconds. Glaciated conditions were the least observed, with a total duration of just 1 minute and 56 seconds.

### 5.3 Atmosphere characterization of Appendix O icing environment in the selected flight

In order to characterize large droplet icing parameters for the selected flight (OF9), 1 Hz data points with an Appendix O flag value of '1' are considered. As previously mentioned, each data point is averaged over a 30-second interval, and their 99<sup>th</sup> percentile value is calculated. All data points represent freezing drizzle conditions with  $D_{\max} \leq 500 \mu\text{m}$  and are categorized

into two classes: (1) Freezing drizzle with an MVD  $< 40 \mu\text{m}$ , and (2) freezing drizzle with an MVD  $> 40 \mu\text{m}$ .

In the analysis, it is found that 45 minutes and 43 seconds of the data had an MVD higher than  $40 \mu\text{m}$ , with the maximum observed MVD being  $172 \mu\text{m}$ , and the highest recorded LWC was  $0.32 \text{ g m}^{-3}$ . On the other hand, 14 minutes and 5 seconds of the data had an MVD smaller than  $40 \mu\text{m}$ , with the highest LWC recorded as  $0.28 \text{ g m}^{-3}$ .

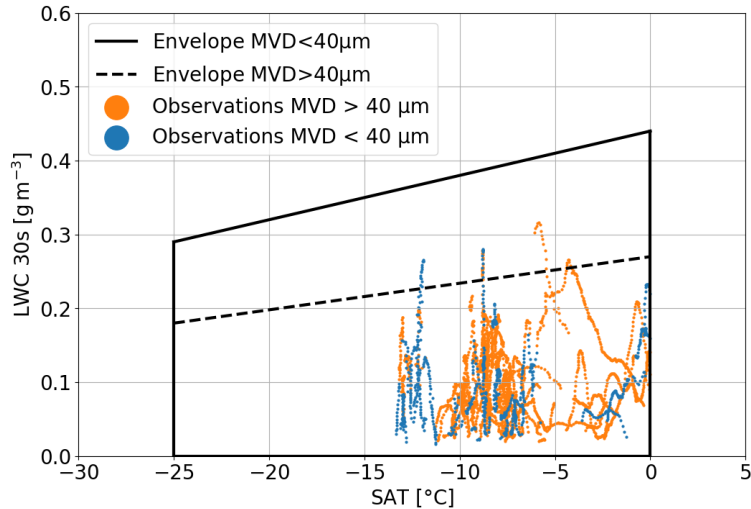


Figure 47: 30-s averaged LWC data points placed in the freezing drizzle envelope.

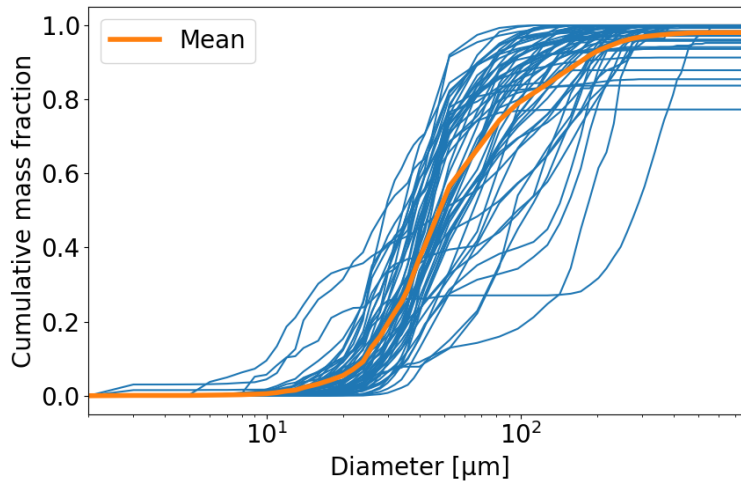


Figure 48: Cumulative mass distributions of Appendix O encounters observed during the selected flight and their mean.

Figure 48 presents that all large droplet icing cases presented in the flight appear to have formed through a nonclassical process, meaning through a condensation and collision-coalescence mechanism. With hardly any SLD over  $500 \mu\text{m}$  diameter, there is no evidence of the classical

freezing rain formation process. The mean MVD value is found as  $48 \mu\text{m}$ . Consequently, severe icing was not expected on the flight. On the other hand, two curves with very high MVDs are contaminated by ice crystals.

The cloud parameter profiles as a function of altitude in Figure 49 illustrates the median and 99<sup>th</sup> percentile measurements of LWC, number concentration, and MVD observed throughout the selected flight, considering only Appendix O measurements. The most frequent icing encounters occurred within the altitude range of 3600 to 4200 meters, corresponding to a temperature range between  $-5^\circ\text{C}$  and  $-10^\circ\text{C}$ . Median LWC measurements ranged up to  $0.18 \text{ g m}^{-3}$ , while the 99th percentile values reached up to  $0.32 \text{ g m}^{-3}$ . The particle number concentration reached up to  $20 \text{ cm}^{-3}$ .

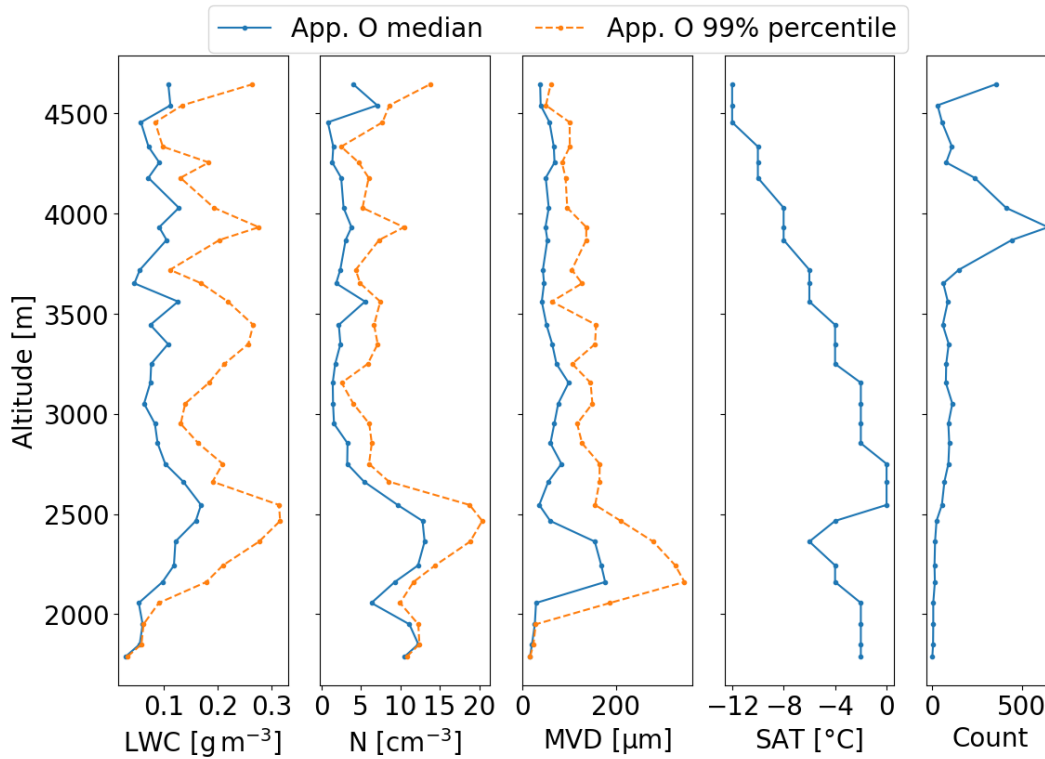


Figure 49: 30-s averaged LWC, concentration, MVD, temperature, and occurrence data of Appendix O encounters in the selected flight as a function of altitude.

The figure illustrates that there is an increase in MVD with decreasing altitude, indicating the presence of larger particles at lower altitudes within the clouds. This phenomenon can be attributed to sedimentation, where droplets are affected by gravity and undergo collision and growth. However, the results also indicate a significant increase in both number concentration and LWC at an altitude of 2500 m. This increase is influenced by a lower supercooled cloud encountered in the first segment, which is also associated with temperature inversion.

In Figure 50, the profiles of MVD, LWC, and particle number concentration (N) over temperature, along with their respective standard deviations, are depicted. LWC values present a stable profile over temperature around  $0.1 \text{ g m}^{-3}$ . It is also observed that MVD tends to increase as temperature rises, which can be attributed to sedimentation as explained in the previous paragraph. Notably, the standard deviation of MVD is relatively larger around  $-4 \text{ }^\circ\text{C}$  and the particle concentration does not show a direct relation with the LWC profile.

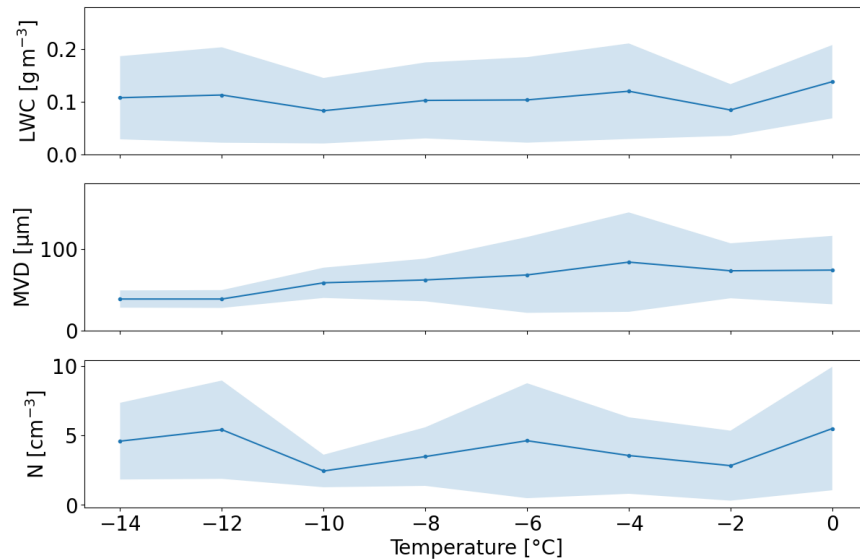


Figure 50: LWC, MVD, and particle number concentration (N) vs temperature profiles of Appendix O encounters during the flight.

Figure 51 shows histograms of LWC, number concentration, temperature, and altitude for large droplet icing encounters measured during OF9. While the data is insufficient for an in-depth comparison, it is evident that Appendix O encounters with  $\text{MVD} < 40 \text{ } \mu\text{m}$  exhibit a higher number concentration profile and a lower LWC profile. On the other hand, Figure 52 illustrates the contribution of SLDs to the LWC and their concentration. It can also be seen that SLDs are relatively rare compared to small droplets, but they do contribute to the LWC due to their larger size. It is important to note that every count represents one second of collected data that is averaged over 30 seconds.

The histogram plots reveal that both Appendix O icing conditions, whether with MVD larger or smaller than  $40 \text{ } \mu\text{m}$ , are observed in similar environments characterized by LWC values below  $0.3 \text{ g m}^{-3}$  and concentrations below  $20 \text{ cm}^{-3}$ . The temperature range for both types of conditions falls between  $0$  and  $-14 \text{ }^\circ\text{C}$ , while the altitude range spans from  $2000$  to  $4700 \text{ m}$ . Notably, icing conditions with  $\text{MVD} < 40 \text{ } \mu\text{m}$  tend to occur at higher concentrations and higher altitudes, although their LWC values remain similar. The contribution of SLDs to the

LWC is lower than smaller droplets due to their infrequent occurrence, which is supported by the concentration histogram of SLDs in Figure 52. Low LWC contribution of SLD is also a sign that large droplet concentration and severity of the icing condition were low.

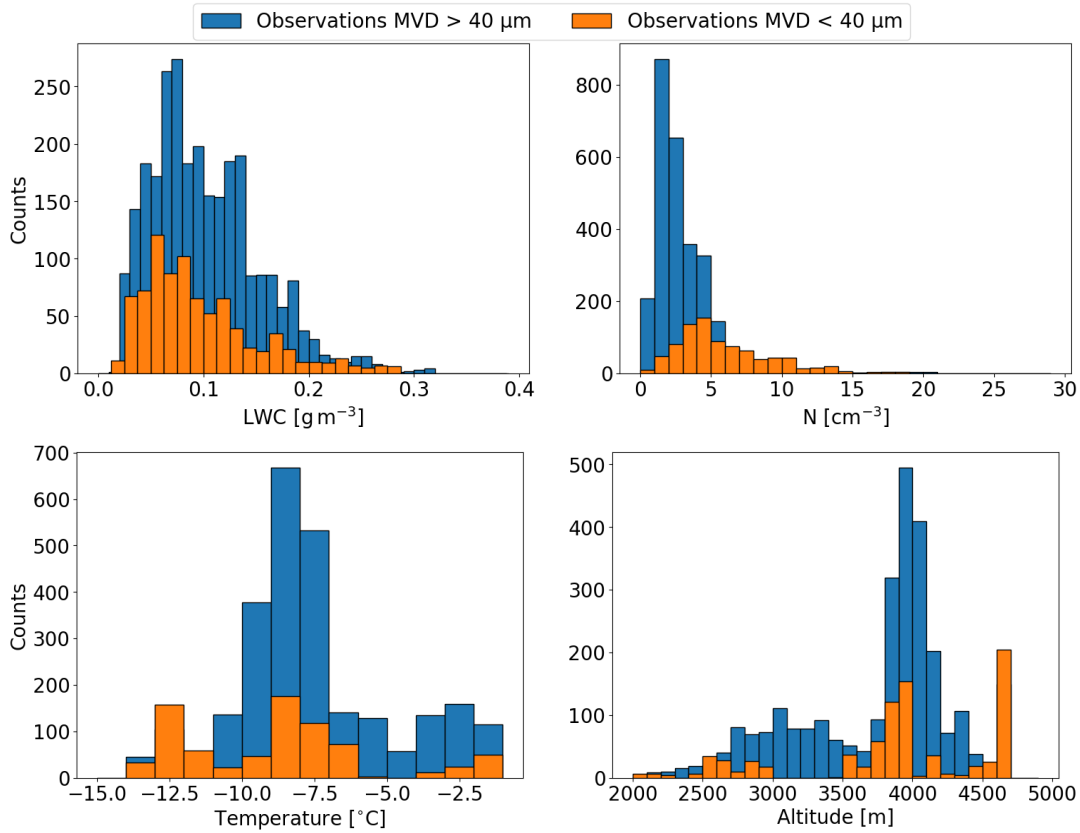


Figure 51: Frequency distributions of LWC, number concentration, temperature, and altitude for the Appendix O encounters measured during OF9. Blue blocks represent observations with MVD > 40 μm, while orange blocks represent observations with MVD < 40 μm .

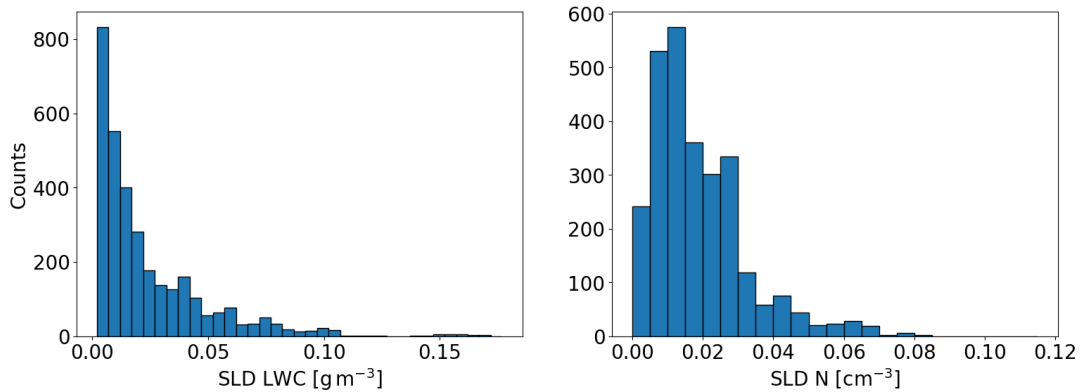


Figure 52: Frequency distributions of the water content contribution of SLDs and their concentration.

It is worth noting that data from a single flight should not be considered sufficient for making definitive conclusions about icing condition characteristics. Rather, it serves the purpose of characterizing the cloud system specific to this particular flight. To set the case study into perspective, the altitude profiles of cloud microphysical parameters from all processed flights are provided in Figure 53.

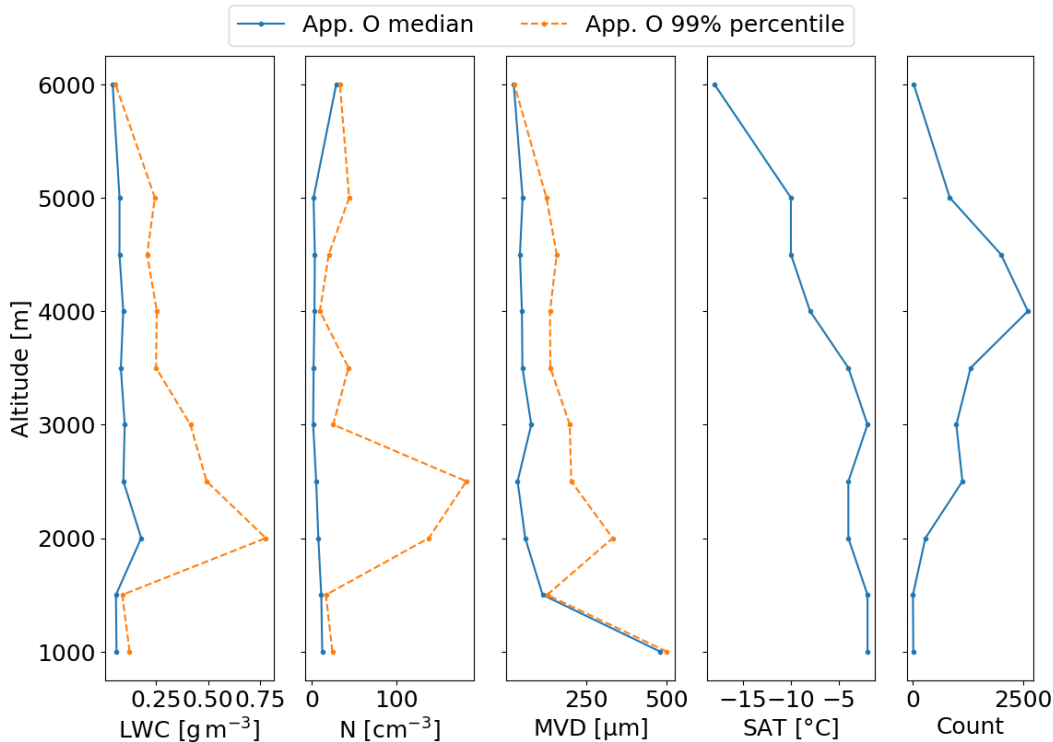


Figure 53: 30-s averaged LWC, concentration, MVD, temperature, and occurrence data of Appendix O encounters in SENS4ICE-EU as a function of altitude.

The figure is generated using data from flights characterized by substantial durations of Appendix O icing, namely flights OF1, OF2.2, OF5, OF9, OF10, OF12, OF13, and OF14, based on the DLR Institute of Atmospheric Physics' naming convention. The count plot illustrates that the majority of cloud sampling during Appendix O icing conditions occurred at an altitude of around 4000 m, with the highest LWC measurements of 0.8 g m<sup>-3</sup> and MVD of 300 μm. The comprehensive trend depicted in the plot indicates an increase in 99<sup>th</sup> percentile measurements of MVD and LWC as the altitude decreases. The rise in MVD can be attributed to sedimentation effects, similar to the data assessment conducted in the OF9 case study. A slight increase in the median LWC values is also noticeable as the altitude decreases.

In the figure, another important observation to note is the presence of a temperature inver-

sion below an altitude of 3000m. This region exhibits an increase in LWC, particle number concentration, and MVD as explained in Section 2.3. On the other hand, the substantial increase in MVD below 1500 m is associated with rain measurements occurring at temperatures nearly below 0°C, which are identified as Appendix O icing. Measurements in this altitude range should be ignored.

## 5.4 Cross-validation of assessed conditions by the MSG satellite

To validate the cloud top phase observed throughout the flight and obtain a comprehensive view of the system, the ProPS tool explained in Section 3.3.2 is utilized.

Given the instrument’s capability to capture Earth images within a 12.5-minute scanning interval from South to North (details in Section 3.3.1), the measurements over the flight area occurred roughly 11 minutes after the scan began. Hence, aircraft locations 11 minutes post each measurement’s start time were considered during the selection of MSG images. Accordingly, SEVIRI measurements starting at 13:30, 14:45, 15:00, 15:30, and 16:00 UTC on the flight date, along with auxiliary data provided to the tool. The choice of these times aligns with measurement segments 2, 3, 5, 6, and 7, respectively.

The altitude and longitude values at the acquisition times are then overlaid onto the ProPS outcome images and RGB images captured simultaneously by the MSG satellite. These collocated images are presented below. On the left side, a false colour RGB image from the MSG satellite displays the surface and clouds in white and light blue colours, with colder/higher clouds having a stronger blue tone. The red dot marks the aircraft’s location during the measurement time, depicted on both images. On the right side, the ProPS tool’s outcomes are illustrated, with each colour representing a distinct cloud top phase or occurrence as follows:

- **Grey:** clear sky
- **Purple:** ice cloud
- **Yellow:** mixed-phase cloud
- **Green:** warm liquid cloud
- **Red:** supercooled cloud
- **Blue:** thin ice cloud (cirrus)

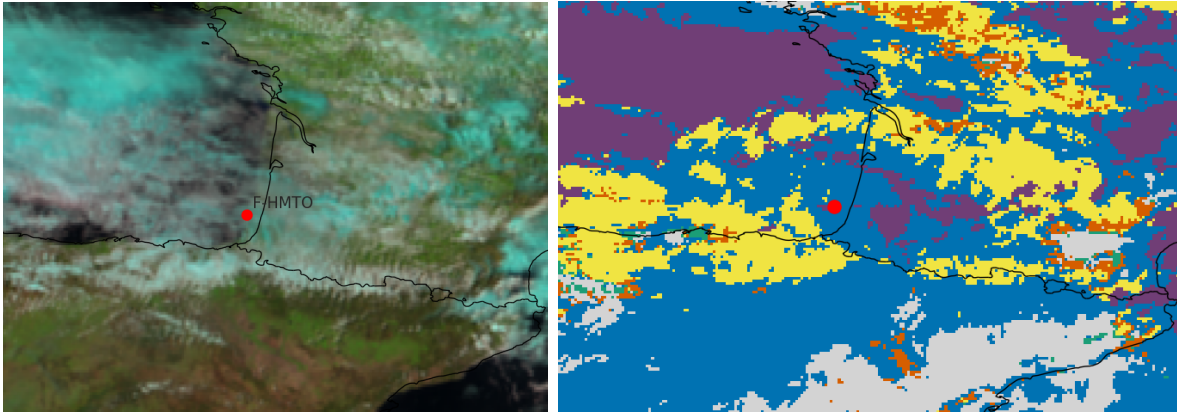


Figure 54: RGB cloud coverage image and ProPS output for 13:30 UTC, representing Segment 2 and acquisition time of 13:41 UTC.

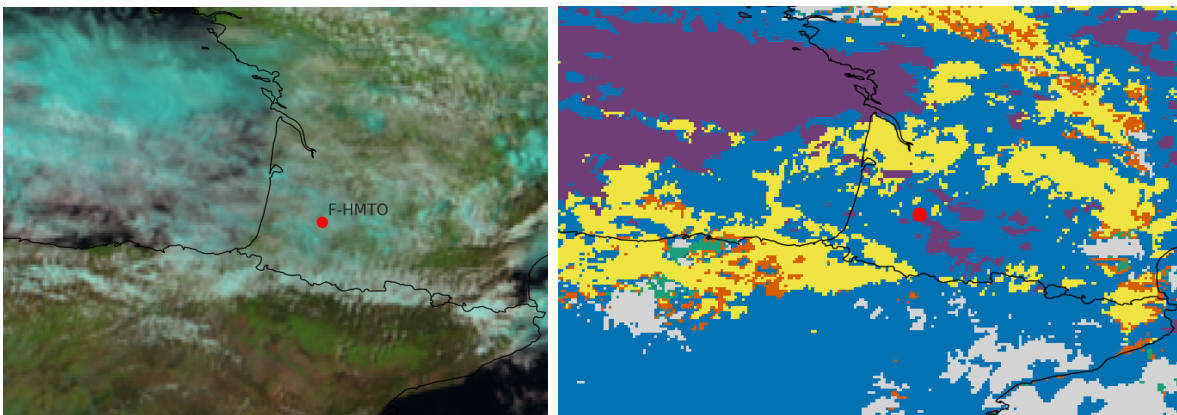


Figure 55: RGB cloud coverage image and ProPS output for 14:15 UTC, representing Segment 3 and acquisition time of 14:26 UTC.

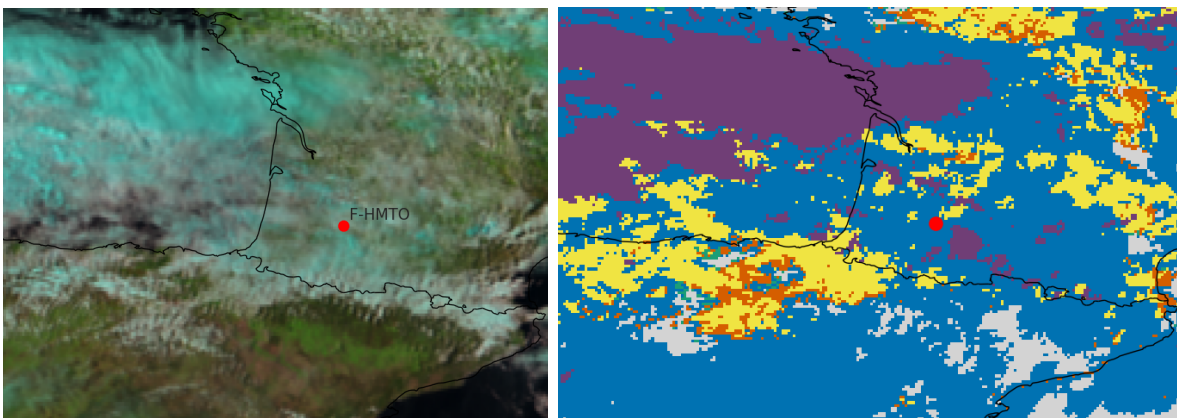


Figure 56: RGB cloud coverage image and ProPS output for 15:00 UTC, representing Segment 5 and acquisition time of 15:11 UTC.

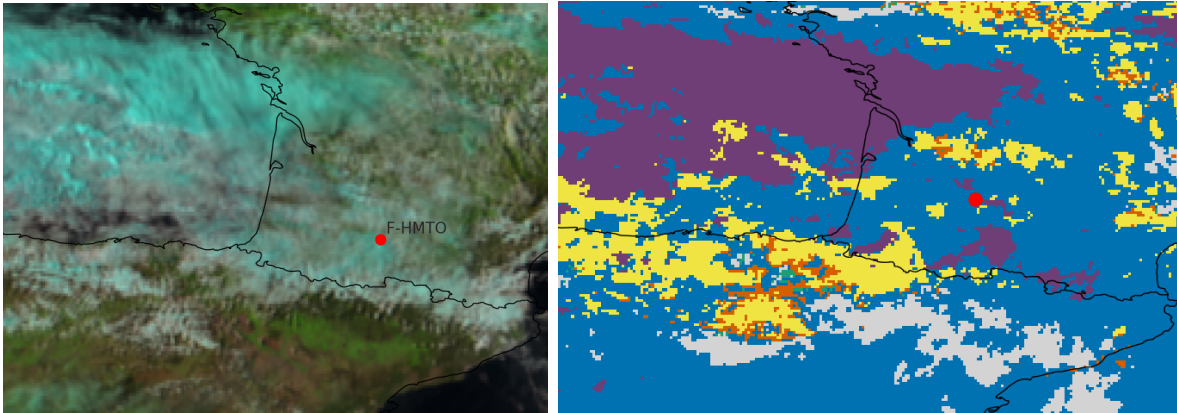


Figure 57: RGB cloud coverage image and ProPS output for 15:30 UTC, representing Segment 6 and acquisition time of 15:41 UTC.

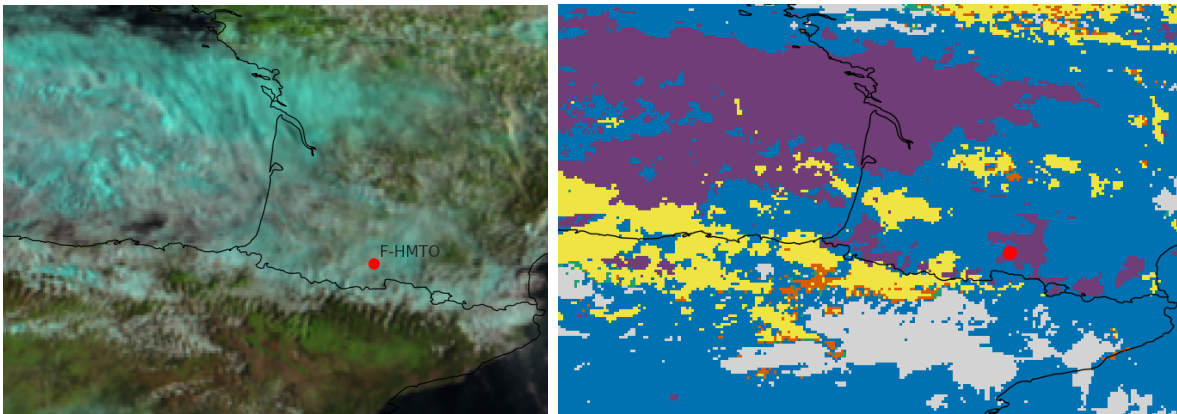


Figure 58: RGB cloud coverage image and ProPS output for 16:00 UTC, representing Segment 7 and acquisition time of 16:11 UTC.

The primary challenge evident in the figures arises from the presence of high-level clouds obscuring the clouds being measured during the flight. As a result, a substantial portion of the clouds detected by the satellite are categorized as "thin ice," corresponding to cirrus clouds, and some as ice clouds at higher altitudes. Although the satellite is capable of capturing segments of the cloud system being observed through the gaps between cirrus clouds, such as in Figure 55 and 56, the cloud tops are often classified as "mixed-phase."

To compare the outcome images from the ProPS tool with the CIP measurements, Figures 55 and 56 are taken into consideration. These figures are selected because the satellite captured the top of the cloud measured by the aircraft during these times, in which cloud top phases are classified as 'mixed phase'. Additionally, Appendix O icing conditions are detected by the data evaluation tool developed in this study around the time of satellite acquisition, which are at 14:26 and 15:11 UTC. Below are the cloud particle images captured by the CIP during these times.

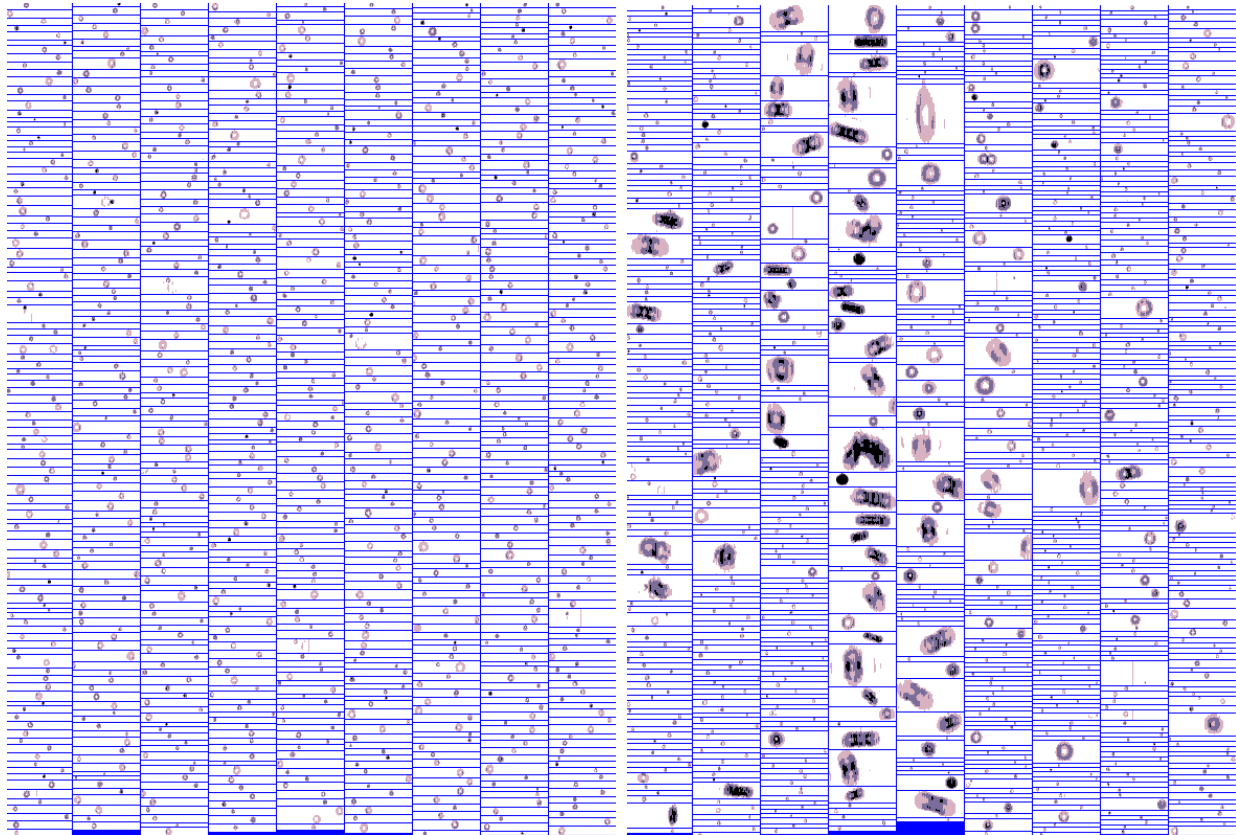


Figure 59: Cloud particle images taken by the CIP during 14:27:08-14:28:16 UTC (left) and 14:28:46-14:28:59 UTC.

In the initial detected encounter starting at 14:27:08 UTC (Figure 59), it is evident that the prevailing condition is small droplet icing with an MVD of  $40 \mu\text{m}$ , an LWC of  $0.20 \text{ g m}^{-3}$ , SAT of  $-8.8^\circ\text{C}$ , and an Altitude of 3930 m. The SLD contribution to LWC is measured at  $0.0073 \text{ g m}^{-3}$  with no detected ice crystals. However, approximately 30 seconds later, an encounter was identified featuring mixed-phase conditions, and its cloud particle images are displayed on the right side of the figure. In this subsequent encounter, the conditions recorded hold an MVD of  $254 \mu\text{m}$ , an LWC of  $0.04 \text{ g m}^{-3}$ , SAT of  $-8.5^\circ\text{C}$ , and an altitude of 3932 m, with a noticeable concentration of ice crystals. Two encounters existing in the same temperature and altitude range show that the thermodynamic phase of the cloud is variable over the cloud extent. Mixed-phase cloud conditions exist within the cloud system, although relatively sparse compared to the supercooled phase. This can conclude that the ProPS tool is correct for this encounter case.

The second presented cloud particle images in Figure 60 represent an insight into the cloud system during the acquisition time of the MSG satellite at 15:12 UTC in Figure 56. The encounter detected starts at 15:10:53 UTC and lasts at 15:12:26 carries small droplet icing

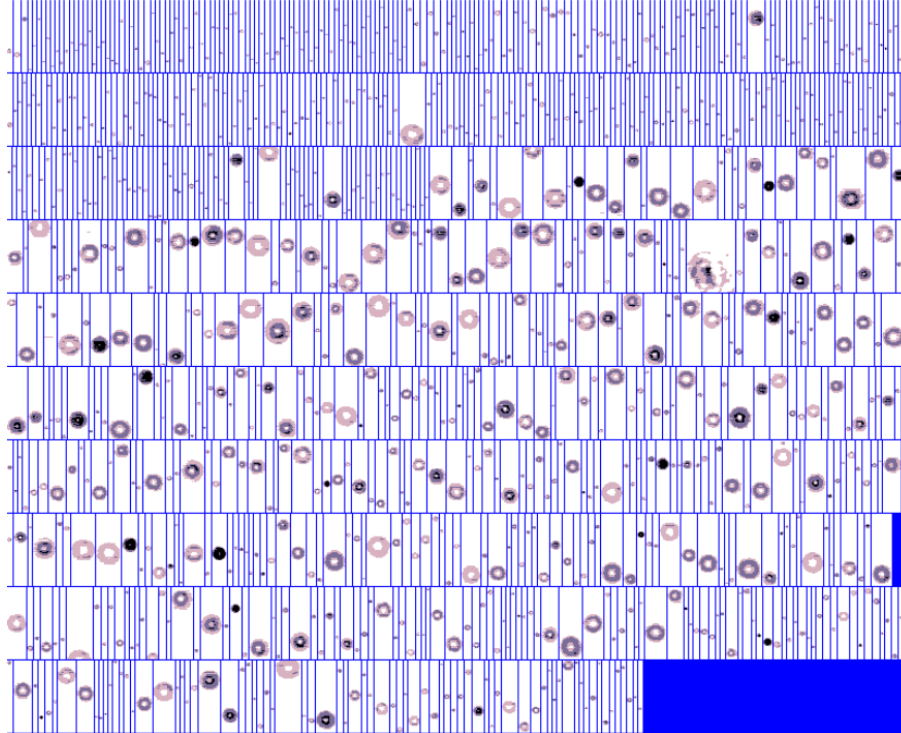


Figure 60: Cloud particle images taken by the CIP during 15:10:53-15:12:26 UTC.

condition characteristics at first but then detects large concentrations of SLD. The cloud microphysical conditions are as follows: MVD of  $39 \mu\text{m}$ , an LWC of  $0.05 \text{ g m}^{-3}$ , and SAT of  $-7.4^\circ\text{C}$  at an altitude of 3891 m. SLD contribution to the LWC is measured as  $0.0089 \text{ g m}^{-3}$  and scarcely any ice crystals were present in the encounter. The condition of the cloud system can be thus defined as supercooled.

Overall, ProPS classifies the measured cloud system predominantly as mixed-phase. This is confirmed by the in-situ data, which has observed both liquid droplets and ice crystals in the cloud system as seen in Figure 43. However, in the second case analysed here, the ProPS results (mixed-phase) do not match the in-situ observations (supercooled). A reason might be the partial obstruction of pixels by higher-level clouds, visible in the RGB cloud coverage images. This leads to a mixture of radiation signals from the lower and overlying clouds and decreases the confidence level in cloud top phase classifications. Another reason could be the presence of SLDs (see Figure 60), which increase the effective radius of the cloud, resulting in a radiative signal in the satellite channels more similar to that of ice crystals. Therefore, further investigation is needed to assess the tool's reliability, particularly by applying the same procedure to flights with less obstruction from higher-level clouds.

## 6 Conclusion and outlook

Airborne in-situ measurements of clouds with a high potential for the presence of supercooled large droplets (SLDs) were conducted as part of the SENS4ICE measurement campaign in Southern France in April 2023. The measurements were carried out using cloud microphysical measurement instruments, including the CIP, CDP, Nevzorov hot-wire, and HSI, aboard an ATR-42 research aircraft. They served as a reference for the evaluation of newly developed SLD detection sensors during the campaign and provided cloud measurement data for atmospheric research. This work presented an evaluation strategy of the CIP data to identify conditions associated with large droplet icing and the presence of SLDs. The evaluated data was then combined with the CDP to cover a comprehensive particle size range from 2  $\mu\text{m}$  to 960  $\mu\text{m}$ . The SLD images and measurements obtained from the CIP and the HSI were subsequently compared with each other to find out the impact of differences in measurement characteristics.

The particle selection criteria were configured to ensure that the CIP provides good statistical data by maintaining depth of field while minimizing the inclusion of large out-of-focus particles, which can lead to uncertainties in phase detection. The selection criteria for data evaluation specifically involves particles smaller than 90  $\mu\text{m}$  with a minimum of one pixel at a 50% shadow level, and particles larger than 90  $\mu\text{m}$  with over half of their pixels at a 75% shadow level. This method and the data processing procedure can be deemed successful as it effectively identified the majority of large droplet icing conditions and supercooled large droplets (SLDs). However, it is important to acknowledge that some SLDs were undetected because they were not sufficiently in-focus and some were classified as ice crystals due to the coincidence of two droplets within the same image frame. Therefore, there is room for further refinement of the procedure. The primary concern that warrants investigation is the consistent underestimation of liquid water content (LWC) by the Cloud Imaging Probe (CIP) compared to the TWC sensor of the Nevzorov hot-wire probe, with a discrepancy of roughly 40%. This underestimation was considered as a systematic error by a bias factor.

In the comparison of particle images obtained from the HSI and the CIP, one long icing encounter from the flight campaign was considered with a high concentration of large droplets. Despite the HSI's high image resolution achieved through its new imaging method, the instrument detected significantly fewer SLDs due to its smaller sample volume and could not provide good statistical data compared to the CIP. On the other hand, a comparison of the two probes showed that the CIP measurements were underestimated due to low particle num-

ber concentration measurements. This also explains the discrepancy between the CIP and Nevzorov hot-wire probe's LWC measurements. Consequently, it can be inferred that the HSI operates efficiently primarily during sustained encounters with high particle concentrations.

The second part of the study involves the demonstration of the presented data evaluation procedure with a selected flight from the SENS4ICE flight campaign. The ninth observational flight of the campaign was selected for the case study, which took place on April 24. The flight involved following an incoming warm front in a Lagrangian flight pattern as it progressed inland in Southern France. Therefore, icing conditions in the same cloud system were sampled over the ocean and later on the land. In order to evaluate the flight, cloud measurements by the presented instruments and indications of large droplet icing conditions were initially presented. The flight was divided into eight segments, with each segment separated by deicing cycles required for sensor calibration and safety precautions. The particle size distribution for each segment was shown to demonstrate the evolution of the cloud system over time. Subsequently, the identified Appendix O icing encounters were investigated separately to for characterization. Lastly, the flight results were validated using the ProPS tool, which is specifically designed for identifying cloud occurrence and determining the thermophysical phase of cloud tops, by using SEVIRI measurements of MSG satellites.

Throughout the case study flight, a total of 59 minutes and 48 seconds of data met the criteria for Appendix O icing standards, with 45 minutes and 43 seconds of it having an MVD value greater than  $40\ \mu\text{m}$ . The highest recorded LWC value reached  $0.32\ \text{g m}^{-3}$ . The presence of clean marine air originating from the ocean provided favourable conditions for supercooled large droplets (SLD) to form and grow. Over time, there was an observed increase in both LWC and MVD as the frontal system developed. As the flight progressed and the altitude decreased, there was a noticeable increase in MVD, attributed to the sedimentation of cloud droplets as they descended and collided. Additionally, the number concentration of ice crystals increased as the system moved towards the mountains. This phenomenon was driven by the orographic uplift of ice-nucleating particles by the Pyrenees, resulting in the formation of ice crystals in the last three segments. Supercooled water droplets also froze upon contact with these ice nuclei, increasing the ice crystal concentration. In addition to the case study, the cloud measurements conducted during the identified Appendix O icing conditions in the entire flight campaign were presented to offer a comprehensive perspective.

The cloud measurements conducted during the selected flight were lastly compared with satellite measurements to analyze the broader cloud system that was sampled and explore the potential for detecting SLD icing conditions using spaceborne measurements. Throughout

the selected flight, higher-level cirrus clouds above the measured cloud system were observed. These cirrus clouds hindered the consistent determination of the cloud top thermodynamic phase using the ProPS tool, which relies on SEVIRI images from MSG satellites. The limitations of using passive satellite products became evident. However, the tool still managed to retrieve cloud top phase information from the gaps between cirrus clouds, mostly categorizing the measured cloud system as "mixed-phase." This result was attributed to the presence of ice crystals and the predominance of the pure supercooled phase in the middle or lower sections of the clouds. The methodology employed in this thesis is suggested for implementation in other observational flights conducted during the campaign, particularly those with reduced interference from higher-level clouds. Therefore, the accuracy of the tool can be further evaluated.

## 7 References

- [1] URL: <https://artsandculture.google.com/asset/de-icing-aircraft-ravilious-eric/sgHpKOYQpwwKlQ>.
- [2] June 2015. URL: <http://www.bom.gov.au/aviation/data/education/icing.pdf>.
- [3] *2021 Safety Report*. Tech. rep. International Air Transport Association (IATA), 2022.
- [4] Richard K Jeck. “Icing Design Envelopes (14 CFR Parts 25 and 29, Appendix C) Converted to a Distance-Based”. In: *Federal Aviation Administration, US Department of Transportation: Washington, DC, USA* (2002).
- [5] Stewart G Cober and George A Isaac. “Characterization of aircraft icing environments with supercooled large drops for application to commercial aircraft certification”. In: *Journal of Applied Meteorology and Climatology* 51.2 (2012), pp. 265–284.
- [6] *Loss of Control Simmons Airlines, dba American Eagle Flight 4184 Avions de Transport Regional (ATR) Model 72-212, N401AM Roselawn, Indiana October 31, 1994*. Tech. rep. National Transportation Safety Board.
- [7] Eric Malnic. *Report blames FAA for 1997 plane crash*. Aug. 1998. URL: <https://www.latimes.com/archives/la-xpm-1998-aug-28-mn-17490-story.html>.
- [8] AV Korolev, JW Strapp, and GA Isaac. “Evaluation of the accuracy of PMS optical array probes”. In: *Journal of Atmospheric and Oceanic Technology* 15.3 (1998), pp. 708–720.
- [9] Tina Jurkat-Witschas et al. *Overview of Cloud Microphysical Measurements during the SENS4ICE Airborne Test Campaigns: Contrasting Icing Frequencies from Climatological Data to First Results from Airborne Observations*. Tech. rep. SAE Technical Paper, 2023.
- [10] URL: <https://skybrary.aero/articles/high-level-ice-crystal-icing-effects-engines>.
- [11] John M Wallace and Peter V Hobbs. *Atmospheric science: an introductory survey*. Vol. 92. Elsevier, 2006.
- [12] Roland Stull. *7.2: Nucleation of liquid droplets*. Dec. 2022. URL: [https://geolibretexts.org/Bookshelves/Meteorology\\_and\\_Climate\\_Science/Practical\\_Meteorology\\_\(Stull\)/07%3A\\_Precipitation\\_Processes/7.02%3A\\_Nucleation\\_of\\_Liquid\\_Droplets](https://geolibretexts.org/Bookshelves/Meteorology_and_Climate_Science/Practical_Meteorology_(Stull)/07%3A_Precipitation_Processes/7.02%3A_Nucleation_of_Liquid_Droplets).
- [13] MK Politovich. “Aircraft icing”. In: *Encyclopedia of atmospheric sciences* 358.1776 (2003), pp. 68–75.

- [14] Ben C Bernstein et al. “Keys to differentiating between small-and large-drop icing conditions in continental clouds”. In: *Journal of Applied Meteorology and Climatology* 58.9 (2019), pp. 1931–1953.
- [15] Richard J. Ranaudo. “Hazardous Ice”. In: *Focus on commercial aviation safety* 109 (Winter 2017), pp. 17–22.
- [16] Ben C Bernstein. “Regional and local influences on freezing drizzle, freezing rain, and ice pellet events”. In: *Weather and forecasting* 15.5 (2000), pp. 485–508.
- [17] Roy M Rasmussen et al. “The 1990 Valentine’s Day arctic outbreak. Part I: Mesoscale and microscale structure and evolution of a Colorado Front Range shallow upslope cloud”. In: *Journal of Applied Meteorology and Climatology* 34.7 (1995), pp. 1481–1511.
- [18] JR Holton, JA Curry, and JA Pyle. *Encyclopedia of Atmospheric Sciences, Volumes 1-6–Wildfire Weather*.
- [19] URL: [https://www.weather.gov/source/zhu/ZHU\\_Training\\_Page/icing\\_stuff/icing/icing.htm](https://www.weather.gov/source/zhu/ZHU_Training_Page/icing_stuff/icing/icing.htm).
- [20] URL: [https://www.law.cornell.edu/cfr/text/14/appendix-0\\_to\\_part\\_25](https://www.law.cornell.edu/cfr/text/14/appendix-0_to_part_25).
- [21] Olivier Boucher et al. “Clouds and aerosols”. In: *Climate change 2013: The physical science basis. Contribution of working group I to the fifth assessment report of the intergovernmental panel on climate change*. Cambridge University Press, 2013, pp. 571–657.
- [22] Shawn Wendell Wagner and David James Delene. “Technique for comparison of backscatter coefficients derived from in situ cloud probe measurements with concurrent airborne lidar”. In: *Atmospheric Measurement Techniques* 15.21 (2022), pp. 6447–6466.
- [23] Colin Gurganus and Paul Lawson. “Laboratory and flight tests of 2D imaging probes: Toward a better understanding of instrument performance and the impact on archived data”. In: *Journal of Atmospheric and Oceanic Technology* 35.7 (2018), pp. 1533–1553.
- [24] Manuel Moser. “Characterization and calibration of an optical array probe and airborne in-situ measurements of mixed-phase clouds”. In: (2018).
- [25] Sarah Woods. *Earth Observing Laboratory*. URL: <https://www.eol.ucar.edu/instruments/two-dimensional-optical-array-cloud-probe>.
- [26] Sebastian J O’Shea et al. “Revisiting particle sizing using greyscale optical array probes: evaluation using laboratory experiments and synthetic data”. In: *Atmospheric Measurement Techniques* 12.6 (2019), pp. 3067–3079.

- [27] Lyle Lilie et al. *A New 1D2D Optical Array Particle Imaging Probe for Airborne and Ground Simulation Cloud Measurements*. Tech. rep. SAE Technical Paper, 2023.
- [28] AV Korolev et al. “In situ measurements of liquid water content profiles in midlatitude stratiform clouds”. In: *Quarterly Journal of the Royal Meteorological Society: A journal of the atmospheric sciences, applied meteorology and physical oceanography* 133.628 (2007), pp. 1693–1699.
- [29] Thibault Vaillant de Guélis et al. “Study of the diffraction pattern of cloud particles and the respective responses of optical array probes”. In: *Atmospheric Measurement Techniques* 12.4 (2019), pp. 2513–2529.
- [30] Artium. *High-Speed Imaging Flight Probe Model HSI-VC-Can-r User Manual*. 2020.
- [31] Biagio M Esposito et al. *Wind Tunnel Measurements of Simulated Glaciated Cloud Conditions to Evaluate Newly Developed 2D Imaging Probes*. Tech. rep. SAE Technical Paper, 2019.
- [32] URL: <https://www.eumetsat.int/meteosat-second-generation>.
- [33] Feb. 2023. URL: <https://www.eumetsat.int/meteosat-10meteosat-11-mission-swap>.
- [34] DMA Aminou. “MSG’s SEVIRI instrument”. In: *ESA Bulletin(0376-4265)* 111 (2002), pp. 15–17.
- [35] Claudia Tranquilli et al. “Meteosat SEVIRI performance characterisation and calibration with dedicated Moon/Sun/deep-space scans”. In: *14th International Conference on Space Operations*. 2016, p. 2536.
- [36] URL: <https://www.eumetsat.int/rapid-scanning-service>.
- [37] Johanna Mayer. “Bayesian Cloud Top Phase Determination for Meteosat Second Generation”. In: (2023).
- [38] Sara Lance et al. “Water droplet calibration of the Cloud Droplet Probe (CDP) and in-flight performance in liquid, ice and mixed-phase clouds during ARCPAC”. In: *Atmospheric Measurement Techniques* 3.6 (2010), pp. 1683–1706.
- [39] AV Korolev et al. “The Nevzorov airborne hot-wire LWC–TWC probe: Principle of operation and performance characteristics”. In: *Journal of Atmospheric and Oceanic Technology* 15.6 (1998), pp. 1495–1510.
- [40] Alexei Korolev. “Reconstruction of the sizes of spherical particles from their shadow images. Part I: Theoretical considerations”. In: *Journal of Atmospheric and Oceanic Technology* 24.3 (2007), pp. 376–389.

- [41] Stewart Cober et al. “Defining Characteristic Cloud Drop Spectra From In-situ Measurements.” In: *41st aerospace sciences meeting and exhibit*. 2003, p. 561.
- [42] Stewart G Cober et al. “Assessing cloud-phase conditions”. In: *Journal of Applied Meteorology and Climatology* 40.11 (2001), pp. 1967–1983.
- [43] Dean Miller and Christopher Lynch. “Overview of high speed close-up imaging in an icing environment”. In: (2004), p. 407.
- [44] URL: <https://view.eumetsat.int/productviewer?v=default>.

## 8 Appendix

### A - Encounter between 16:08:59 - 16:12:02

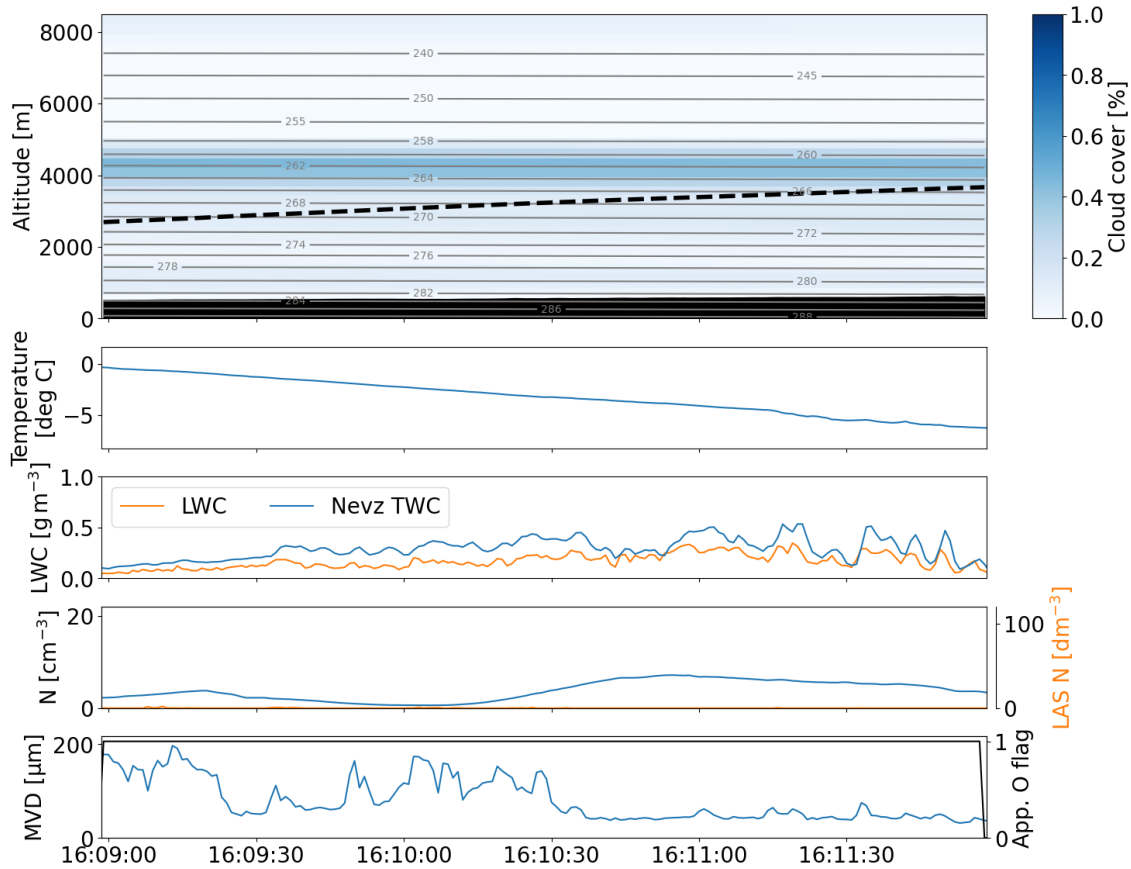


Figure 61: Altitude, temperature, LWC, and MVD profiles between 16:08:59 - 16:12:02

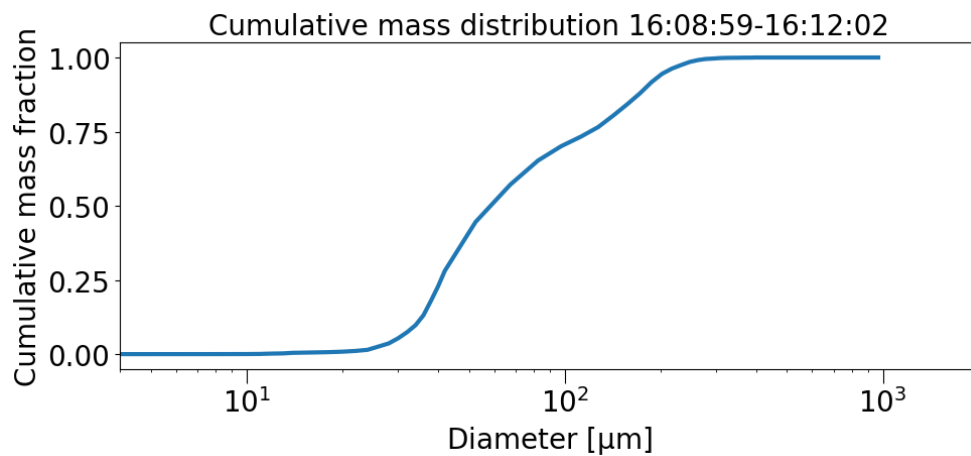


Figure 62: Cumulative mass distribution of particles encountered between 16:08:59 - 16:12:02

## B - Satellite images of the flight area on 24 April 2023

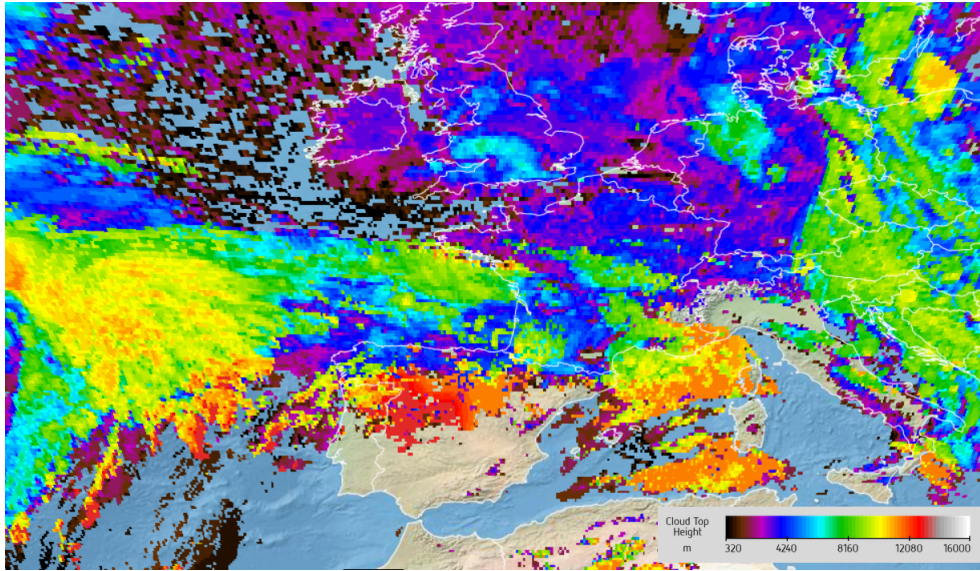


Figure 63: Cloud top height map of the flight zone recorded by MSG on 24 April 2023 at 14:00 UTC. [44] The product indicates the height of the highest cloud in each particular pixel.

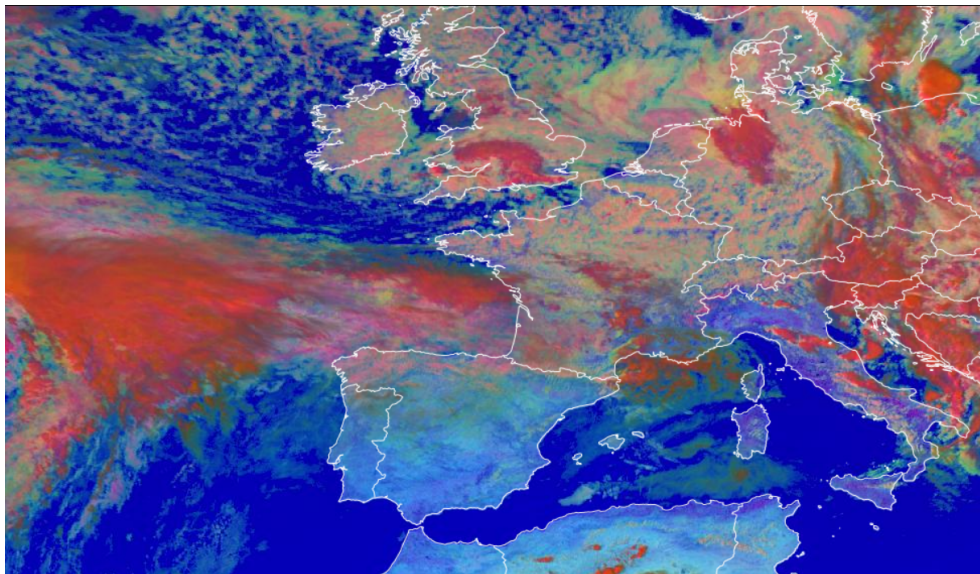


Figure 64: Day Microphysics RGB map of the flight zone recorded by MSG on 24 April 2023 at 14:00 UTC. [44] Green clouds represent lower-level cold clouds measured during the flight, whereas red clouds represent higher-level cirrus clouds. Blue areas are cloud-free.